Contents

List of Figures

List of Tables

Introduction

This thesis reports the research work performed during the three years of my Ph.D. course at the Physics Department "Galileo Galilei" of the Università di Padova.
Most of my research activity has been carried out at the Consorzio RFX [1], located inside the Consiglio Nazionale delle Ricerche (CNR) area of Padova, where operates the Reversed Field eXperiment, namely RFX-mod, the largest fusion experiment currently operating in the *Reversed-Field Pinch* (RFP) configuration.
The RFP, together with the Tokamak and the Stellarator, is one of the main configurations used to confine a *plasma* in a toroidal device by means of a combination of magnetic fields, in order to study controlled thermonuclear fusion as an energy source.

My research activity on the RFX-mod experiment is mainly focused on the study of high frequency magnetic fluctuations occurring in the plasma.
A plasma, indeed, constitutes a strongly nonlinear system, characterized by electromagnetic instabilities, waves and turbulent fluctuations which can cause losses of energy and particles. For this reason the investigation of the mechanisms underlying these processes constitutes a key topic in fusion research. Understanding the origin of instabilities is expected to contribute to improve energy and particle confinement in experimental devices by taming the causes or mitigating the associated losses. Moreover, progresses in this field can also give an important contribution to the understanding of the origin and the features of instabilities in other magnetized plasmas, including astrophysical ones.

In order to help the reader to better understand the context, the first three chapters of my thesis give a brief overview of introductive information about the plasma characteristics, the RFP configuration and the experimental settings where my research activity has developed.

In particular, in *Chapter 1* the concept of plasma and its dynamics are introducted and the thermonuclear fusion, a promising method to generate energy, is presented. In order to achieve a positive energy balance in a future

fusion reactor, the plasma is confined by magnetic fields of toroidal topology and the instabilities that can develop and, in some cases, cause particle losses, must be known and controlled: in this chapter magnetohydrodynamic (MHD) equations and some magnetic instabilities mentioned in the future chapters are presented.

In *Chapter 2* a brief introduction to the Reversed-Field Pinch configuration and to the RFX-mod experiment and its typical plasma is given. The main characteristics of the configuration, such as the reversal of the toroidal field at the edge of the plasma column and the transition to a better-confined regime, with a helical-shaped plasma, are highlighted.
A section in this chapter describes EXTRAP T2R , a RFP machine located in Stockholm, where part of my research has been carried out during an interesting experimental campaign.

Chapter 3 presents the systems of probes (the U-probe, the ISIS system, the Alfvén probe) used in RFX-mod and EXTRAP T2R plasmas to measure electrostatic and magnetic fluctuations described in the thesis. More in detail, the main experimental observations in RFX-mod have been obtained by means of two systems of in-vessel magnetic sensors with high space and time resolution:

- the first one is an insertable edge probe called *U-probe*, measuring the fluctuations of the three components of the magnetic field, and able to investigate high order toroidal harmonics and frequencies up to $5\,MHz$;
- the second one consists of a subset of the *ISIS* (Integrated System of Internal Sensors) diagnostics, a complex system of arrays of sensors covering the whole toroidal and poloidal angles of the torus.

Some information about the other diagnostics mentioned in the thesis in order to to give a physical interpretation to the observations is also reported. Chapter 3 is, moreover, dedicated to the data analysis techniques used for the determination of temporal and spatial periodicities associated to the phenomena observed, which are essential for their characterization.

Several coherent magnetic activities have been observed, analyzed and, in some cases, recognized. The most interesting results obtained during the PhD are presented in the thesis, organized so that each of the following three chapters describes fluctuations of different nature, measured in RFX-mod plasma. In particular, in *Chapter 4*, a strong activity observed to arise at the plasma edge at a frequency of the order of $100\,kHz$ is described.

Various analyses performed in order to trace the dependence relations between the characteristics of the activity and the plasma parameters have been carried out: the modes resonate at the edge of the plasma column, externally respect to the reversal surface of the toroidal magnetic field and the frequency associated with the mode has been found to be mainly due to a Doppler effect, as they rotate with the plasma. An important contribution on the physical interpretation of the modes has been provided by a linear stability analysis performed by means of the code ETAW, solving the resistive MHD equations in cylindrical approximation. The theoretical results have shown a good agreement with the features of the modes experimentally observed; thus, it has been possible to recognize them as belonging to the branch of the **Resistive Interchange Modes**, also known in astrophysics as g**-modes**.
This result has been exposed in a paper published by *Nuclear Fusion* in 2010 [2].

Chapter 5 shows the analysis of a relevant high frequency magnetic activity detected in the poloidal component of the magnetic fluctuation measured by means of the mentioned U-probe, at a frequency in the range $0.1 \div 1.2\,MHz$. Since the beginning, the alfvénic nature of the these modes was clear. In particular, their frequency has been shown to be proportional to the Alfvén velocity. Two main different kind of modes are observed with the features of discrete **Alfvén Eigenmodes**:

- the first kind consists in two distinct modes, both characterized by low poloidal and toroidal periodicities, enduring all the discharge time. The experimental observations suggest an interpretation of these modes in terms of Global Alfvén Eigenmodes. A paper on this topic has been published by *Nuclear Fusion* in 2011 [3].

- the second kind appears only when the plasma undergoes a transition to statees of helical equilibrium, called *Single Helical Axis states*. Further analyses are needed to understand the cause inducing this branch of Alfvén modes.

The study of Alfvén eigenmodes has gained in importance, since it has been observed that they are destabilized by energetic particles; this means that in a fusion reactor, the presence of $\alpha-$particles can make the modes to profusely arise. In this picture, the experimental results presented in this thesis take place as the first observation of Alfvén Eigenmodes in RFX-mod plasma.

Chapter 6 reports some experimental observations concerning a magnetic activity that seems to be associated to the presence of strong temperature

gradients. The preliminary analyses about these modes and the comparison of their characteristics with those predicted by a gyrokinetic code, named GS2, would suggest an interpretation of the activity in terms of **microtearing** instabilities.

During my Ph.D., I was also involved in the collaboration between RFX-mod and the EXTRAP T2R RFP experiments. *Chapter 7* is devoted to the description of this experience: the experimental campaign was mainly dedicated to the revamping of an insertable probe, the Alfvén probe, and the acquisition of electrostatic and magnetic measurements at different radial insertions. A preliminary analysis of the data, included the application of Resonant and Non-Resonant Magnetic Perturbations (RMP and NRMPs), is mentioned.

Introduzione

Questa tesi descrive il lavoro di ricerca che ho svolto durante i tre anni di corso di Dottorato in Fisica presso il Dipartimento di Fisica "Galileo Galilei" dell'Universitá di Padova.
La mia attività di ricerca si è sviluppata principalmente presso il Consorzio RFX [1], che si trova all'interno dell'area del Consiglio Nazionale delle Ricerche (CNR) di Padova, dove opera l'esperimento RFX-mod, il più grande esperimento di fusione attualmente operante in configurazione Reversed-Field Pinch (RFP). L'RFP, insieme al Tokamak e allo Stellarator, è uno delle principali configurazioni usate per confinare in strutture toroidali un *plasma* per mezzo di una combinazione di campi magnetici. Essi si propongono di studiare la *fusione termonucleare controllata* come fonte di energia.

L'attivitá di ricerca svolta presso l'esperimento RFX-mod è stata principalmente focalizzata sullo studio delle fluttuazioni magnetiche ad alta frequenza che si sviluppano nel plasma.
Un plasma, infatti, costituisce un sistema fortemente non-lineare, caratterizzato da instabilità elettromagnetiche, onde e fluttuazioni della turbolenza che possono causare la perdita di energia e particelle. Per questa ragione l'indagine dei meccanismi alla base di questi processi costituisce uno dei temi chiave nella ricerca sulla fusione. Capire l'origine delle instabilitá si pensa possa contribuire a migliorare il confinamento di energia e particelle nei dispositivi sperimentali cercando di domare le cause scatenanti o di attenuare le perdite associate. Inoltre, progressi in questo campo possono dare anche un importante contributo alla comprensione dell'origine e delle caratteristiche di instabilità in altri plasmi magnetizzati, inclusi quelli astrofisici.

Per aiutare il lettore a comprendere meglio il contesto in cui si sviluppa questa tesi, i primi tre capitoli fanno una breve panoramica di informazioni di base per quanto riguarda le caratteristiche del plasma, la configurazione RFP e il *setting* sperimentale presso cui si è sviluppata la mia attivitá di ricerca.

In particolare, nel *Capitolo 1* vengono introdotti il concetto di plasma e la

sua dinamica e la fusione termonucleare, una promettente opportunitá per la produzione di energia. Col fine di raggiungere un bilancio energetico positivo in un futuro reattore a fusione, il plasma è confinato da campi magnetici di geometria toroidale e le instabilitá che possono svilupparsi e, in alcuni casi, causare la perdita di particelle, devono essere conosciute e controllate: in questo capitolo si introducono le equazioni della magnetoidrodinamica (MHD) e alcuni tipi di instabilità magnetiche a cui si farà riferimento nei capitoli successivi.

Nel *Capitolo 2* sono proposte una breve introduzione sulla configurazione Reversed-Field Pinch e sull'esperimento RFX-mod e il suo plasma. Vengono messe in luce le caratteristiche della configurazione, come il rovesciamento del campo toroidale nella regione di bordo del plasma e la transizione ad un regime meglio confinato, con un plasma di forma elicoidale. Una sezione di questo capitolo è dedicata alla presentazione della macchina RFP EXTRAP T2R , che si trova a Stoccolma, presso cui ho partecipato ad un interessante campagna sperimentale.

Il *Capitolo 3* presenta i sistemi di sonde (la U-probe, ISIS, la sonda Alfvén) utilizzati nei plasmi di RFX-mod e EXTRAP T2R per investigare le fluttuazioni elettrostatiche e magnetiche descritte nella tesi. Più in dettaglio, le principali osservazioni sperimentali in RFX-mod sono state ottenute per mezzo di due sistemi di sensori magnetici collocati internamente alla camera da vuoto, altamente risolti in spazio e tempo.

- il primo è una sonda di bordo inseribile, chiamata *U-probe*, che misura le fluttuazioni delle tre componenti di campo magnetico ed è in grado di investigare alti ordini di armoniche toroidali e frequenze fino ai $5\,MHz$;

- il secondo consiste in alcuni sensori della diagnostica *ISIS* (Integrated System of Internal Sensors), un complesso sistema di sonde allineate in modo da coprire interamente gli angoli toroidale e poloidale del toro.

Sono riportate anche alcune informazioni sulle altre diagnostiche usate per dare un'interpretazione fisica alle osservazioni. Il Capitolo 3 è inoltre dedicato alle tecniche di analisi dati usate per la determinazione delle periodicitá temporali e spaziali associate ai fenomeni osservati, che sono essenziali per la loro caratterizzazione.

Diverse attivitá magnetiche coerenti sono state osservate, analizzate e a volte riconusciute. I risultati piú interessanti ottenuti durante il dottorato sono presentati nella tesi, oraganizzati in modo che ognuno dei tre capitoli

seguenti descriva fluttuazioni di diversa natura, misurate nel plasma di RFX-mod.
In particolare, nel *Capitolo 4* è descritta una forte attivitá osservata sorgere a bordo plasma ad una frequenza dell'ordine dei $100\,kHz$.
Sono state effettuate varie analisi con lo scopo di rintracciare relazioni di dipendenza tra le caratteristiche dell'attivitá ed i parametri di plasma: i modi risuonano a bordo plasma, esternamente rispetto alla superficie di rovesciamento del campo magnetico toroidale, e la frequenza associata al modo è stata trovata essere dovuta principalmente all'effetto Doppler, in quanto essi ruotano con il plasma. Un importante contributo all'interpretazione fisica dei modi è stata fornita da un'analisi di stabilitá lineare effettuata per mezzo del codice ETAW, che risolve le equazioni MHD resistive in approssimazione cilindrica. I risultati teorici hanno mostrato un buon accordo con le caratteristiche dei modi osservate sperimentalmente; è stato quindi possibile riconoscerli come appartenenti alla branca dei **Resistive Interchange Modes**, conosciuti anche in ambito astrofisico come g**-modes**.
Questo risultato è stato esposto in un articolo pubblicato da *Nuclear Fusion* nel 2010 [2].

Il *Capitolo 5* mostra l'analisi riguardante un altra attivitá magnetic ad alta frequenza rilevata sulla componente poloidale della fluttuazione magnetica misurata per mezzo della U-probe, ad una frequenza appartenente all'intervallo $0.1 \div 1.2\,MHz$. Sin dall'inizio, è risultata chiara la natura alfvénica di questi modi. In particolare, la loro frequenza è stata mostrata essere proportionale alla velocitá di Alfvén. Sono stati osservati due diversi tipi di modi con le caratteristiche di **modi alfvénici**:

- il primo tipo consiste in due modi distinti, entrambi caratterizzati da baas periodicitá poloidale e toroidale, e sono visibili per tutta la durata della scarica. Le osservazioni sperimentali suggeriscono un'interpretazione di questi modi in termini di Global Alfvén Eigenmodes. Un articolo a questo proposito è stato pubblicato da *Nuclear Fusion* nel 2011 [3].

- il secondo tipo appare solo durante le fasi in cui il plasma assumes un equilibrio elicoidale, detto *stato a Singolo Asse Elicoidale*. Altre analisi sono necessarie per capire la causa che induce questo tipo di modi alfvénici.

Lo studio dei modi alfvénici ha guadagnato importanza nelle ultime decadi, in quanto essi vengono destabilizzati da particelle energetiche; ció significa che in un reattore a fusione, la presenza di particelle α può far nascere modi a profusione. In questo contesto, i risultati sperimentali presentati in questa tesi si

collocano come la prima osservazione di modi alfvénici nel plasma di RFX-mod.

Il *Capitolo 6* riporta alcune osservazioni sperimentali riguardanti un'attivitá magnetica che sembra essere associata alla presenza di forti gradienti di temperatura. Le analisi preliminari inerenti questi modi e il confrontodelle loro caratteristiche con quelle previste da un codice girocinetico, chiamto GS2, suggerirebbero un'interpretazione dell'attivitá in termini di instabilitá **microtearing**.

Durante il mio dottorato ho partecipato ad una collaborazione tra gli esperimenti RFP RFX-mod e EXTRAP T2R. Il *Capitolo 7* è si occupa della descrizione di questa esperienza: la campagna sperimentale è stata dedicata principalmente al ripristino di una sonda inseribile, la sonda Alfvén , e all'acquisizione di misure elettrostatiche e magnetiche a diverse inserzioni radiali. Nel capitolo è esposta un'analisi preliminare dei dati, inclusa l'applicazione di Perturbazioni Magnetiche Risonanti e Non-Risonanti (RMP and NRMPs).

Plasma physics

1.1 Plasma and its dynamics

A *plasma* is a special kind of fluid in which the constituent particles are partially or totally ionized. A fully ionized plasma is a collection of positively charged ions and negatively charged electrons, with approximately equal charge densities, so $n_i \approx n_e \approx n$ (here and in the following the index i and e refer to the ion and the electron particles respectively), obtained by heating a gas to very high temperatures or by passing an electric current through it.
Plasmas constitute more than 99% of the visible universe [4]. As shown in fig. 1.1, plasmas span a huge range in scale length, density and temperature. In plasma physics, density is usually indicated in terms of particles per unity of volume (m^{-3}) and temperature, T, in electronvolt (eV). The choice of using eV is due to the fact that T is considered as average energy ($T[eV] = T[K] \cdot k_B/e$, where k_B is the Boltzmann constant and e the electron charge). In this thesis, temperature is expressed in eV, unless differently indicated.
The term *plasma* was coined in the twenties by Irving Langmuir, a pioneer in the study on ionized gases, but the interest on laboratory plasmas had an important development only from the fifties, when the research on controlled thermonuclear fusion (see section 1.2) took root; then, in the eighties, several plasma tecnologies for industrial applications arose. In particular, in this thesis, we are interested in fusion plasmas, characterized by particle densities of the order of $n \approx 10^{19} \div 10^{20}\ m^{-3}$ and temperatures in the range of $T \approx 0.1 \div 10\ keV$.

Plasma dynamics is dominated by a *collective behaviour*, due to long-range electromagnetic interactions, and by a global charge neutrality.
The last property is assured by the low inertia of electrons that rapidly flow to re-establish neutrality in the case of a charge imbalance, so that any spatial charge inhomogeneity is shielded over a relatively restricted region. Solving the Poisson's equation considering the quasi-neutrality condition, the electrostatic

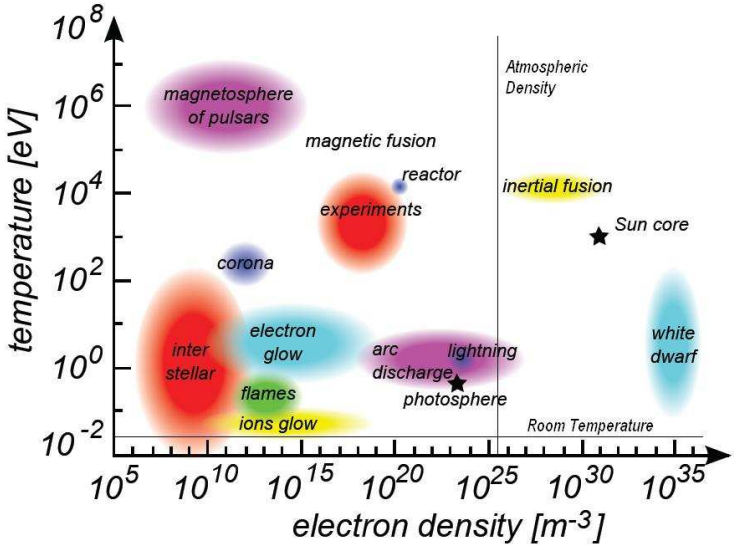

Figure 1.1: Position of several kinds of plasmas in the temperature-density chart. The conditions for a ionized gas to behave like a plasma are fulfilled in a wide range of parameters.

potential ϕ of any charged particle can be derived:

$$\phi(r) \sim exp(-r/\lambda_D) \qquad \text{where} \qquad \lambda_D = \sqrt{\frac{\varepsilon_0 k_B T_e}{n_e e^2}}. \tag{1.1}$$

λ_D is called the *Debye length* and is the maximum typical distance up to which an external electrostatic field can penetrate (ε_0 is the vacuum permittivity). The Debye length is an important plasma parameter, because it gives the order of magnitude of the distance over which the plasma presents a collective behaviour and so can be considered a highly conductive fluid [5].
In the case of laboratory plasmas (whose size is tipically in the range $10^{-2} \div 10\,m$), λ_D measures few microns, so that the dynamics of the particles can be described using the hydrodynamic equations, just adding the laws of electromagnetism: this representation is called *Magneto Hydro Dynamics* (MHD).
The formulation of the equations is here limited to the case of Hydrogen plasma (but it is possible to extend it also to multiple species plasmas) and the displacement current term ($\partial E/\partial t$) in the Ampère's law is neglected.
The system of equations considered is thus:

$$\frac{\partial \rho}{\partial t} + \nabla(\rho \mathbf{v}) = 0 \quad \text{mass continuity} \tag{1.2}$$

$$\rho \frac{d\mathbf{v}}{dt} = \mathbf{j} \times \mathbf{B} - \nabla p \quad \text{momentum continuity} \tag{1.3}$$

$$\mathbf{E} + \mathbf{v} \times \mathbf{B} = \eta \mathbf{j} \quad \text{Ohm's law} \tag{1.4}$$

$$\nabla \times \mathbf{B} = \mu_0 \mathbf{j} \quad \text{Ampère's law} \tag{1.5}$$

$$\nabla \times \mathbf{E} = -\frac{\partial \mathbf{B}}{\partial t} \quad \text{Faraday's law} \tag{1.6}$$

$$\nabla \cdot \mathbf{B} = 0 \quad \mathbf{B} \text{ solenoidality} \tag{1.7}$$

$$\frac{d}{dt}\left(\frac{p}{\rho^\gamma}\right) = 0 \quad \text{state equation} \tag{1.8}$$

(we remember that $\frac{d}{dt} = \frac{\partial}{\partial t} + (\mathbf{v} \cdot \nabla)$).
The MHD model provides a description of a long-wavelength (length scale larger than the Debye one), low-frequency (time scale larger than the inverse of plasma frequency $\omega_p = \lambda_D \backslash v_T$, where v_T is thermal speed of the ions), single-fluid (charge separation is negligible, the Gauss' law can be dropped from the system), homogeneous, isotropic (the pressure $p = n(T_e + T_i)$ is a scalar) plasma; in these conditions it is possible to define the mass density as $\rho = n_e m_e + n_i m_i$, the fluid velocity as $\mathbf{v} = (n_i m_i \mathbf{v_i} + n_e m_e \mathbf{v_e})/\rho$ and the current density as $\mathbf{j} = e(n_i \mathbf{v_i} - n_e \mathbf{v_e})$; μ_0 is the vacuum permeability.
The equation of state 1.8 is added in order to obtain the closure of the system of equations: the exponent γ is chosen depending on the phenomena to describe ($\gamma = 1$ and $\gamma = 5/3$ represents the isothermal and the adiabatic compression respectively).

By combining Ohm's law (eq. 1.4) with the equations 1.5, 1.6 and 1.7 and taking a uniform resistivity η, the *induction equation* is derived:

$$\frac{\partial \mathbf{B}}{\partial t} = \nabla \times (\mathbf{v} \times \mathbf{B}) + \frac{\eta}{\mu_0} \nabla^2 \mathbf{B} \tag{1.9}$$

It is worth noting that the evolution of the magnetic field $\mathbf{B}$ depends on the *convection term* (known also as *dynamo term*, see section 2.1), representing the coupling of the field with the plasma (first term on the right hand side of eq. 1.9), and on the *diffusion term*, describing the penetration of the magnetic field across the plasma (second term).
These two processes work on different time scales: considering a general magnetic structure having a characteristic size L, we can respectively define the *Alfvén transit time*

$$\tau_A = \frac{L}{v_A}, \quad \text{where} \quad v_A = \frac{B}{\sqrt{\mu_0 \rho}} \tag{1.10}$$

is the *Alfvén velocity*, the speed at which magnetic disturbances propagate 1.4.2, and the *resistive diffusion time*

$$\tau_R = \frac{\mu_0}{\eta} L^2. \tag{1.11}$$

The ratio between the characteristic times τ_A and τ_R is called the *Lundquist number*

$$S = \frac{\tau_R}{\tau_A} \propto \frac{B}{\eta \rho^{1/2}} \tag{1.12}$$

and gives an indication of the dominant dynamics.
Typically $\tau_R \gg \tau_A$ (in the laboratory plasmas $S \sim 10^6 \div 10^8$ [6], while in the astrophysical ones (solar corona) $S \sim 10^{12}$ [7]), so the *ideal MHD approximation*, where η is considered negligible, is usually reasonable.
In this case, the *Alfvén's theorem of flux-freezing* [8] implies that the flux of the magnetic field is conserved over any surface and its lines move with the plasma flow. Nevertheless, some narrow plasma regions (*resistive layers*), where the magnetic field lines can be broken and reconnected and resistive instabilities can grow (see Sec. 1.4), can be present.

1.2 Thermonuclear fusion

Thermonuclear fusion plays an essential role in the Universe, as it is the process which powers the stars. A fusion reaction consists in two atomic nuclei fusing to form a single heavier nucleus.

When the particles involved in the reaction have a mass lower than that of

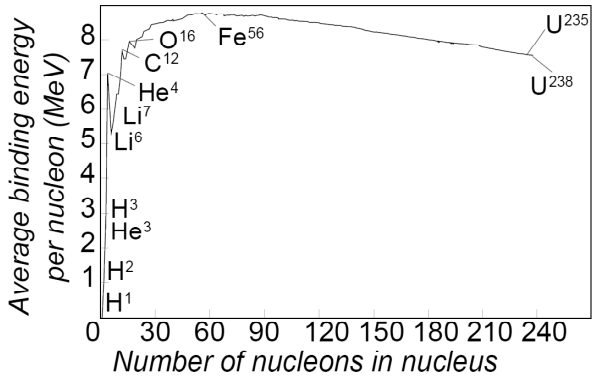

Figure 1.2: Binding energy per nucleon versus atomic mass A.

Iron-57 (this isotope has the highest binding energy per nucleon as shown in figure 1.2), the sum of the masses of the starting nuclei is higher than the mass of the final one, so the fusion process releases energy according to Einstein's formula $\Delta E = mc^2$.
The research on *controlled thermonuclear fusion* relies on the idea of reproducing in the laboratory the conditions suitable to obtain a new convenient energy

source, alternative to fossil fuels and fission reactors. As can be seen from the mentioned figure, the fusion reaction requires high energies to happen as the coulombian repulsion between the nuclei must be overcome; nevertheless, the energies here reported are for monochromatic beams of particles, while in the case of a maxwellian distribution, that is in the plasma state, the required mean energy is significantly lower (around $10\,keV \approx 100$ millions Kelvin).
The most convenient fusion reaction in terms of cross-section, σ, for controlled fusion in the laboratory involves two isotopes of hydrogen, namely deuterium D and tritium T [7], characterized by the lowest threshold energy (see fig. 1.3). The $D-T$ fusion reaction balance is

$$ {}^{2}_{1}D + {}^{3}_{1}T \quad \longrightarrow \quad {}^{4}_{2}He\,(3.5\,MeV) + {}^{1}_{0}n\,(14.1\,MeV) \tag{1.13} $$

The process produces a Helium nucleus and a neutron, with $W_{DT} = 17.6\,MeV$

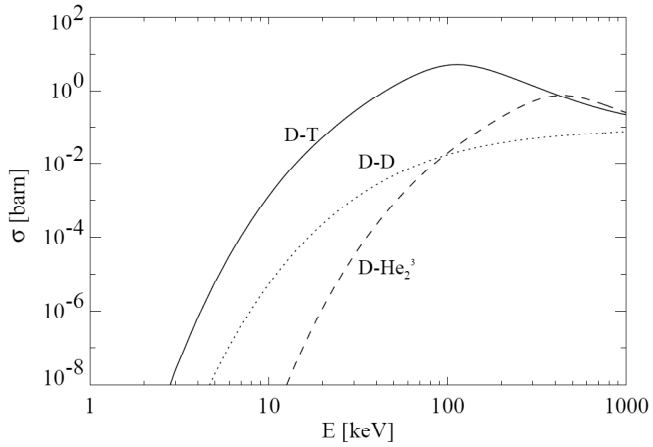

Figure 1.3: Cross section for typical fusion reactions: deuterium-tritium ($D-T$), deuterium-deuterium ($D-D$) and deuterium-helium ($D-{}^{3}He$).

of excess energy in the form of kinetic energy of the products: whereas the $\alpha-$particles are confined by the magnetic fields (see section 1.3) and can contribute to heat the plasma itself, neutrons can be used both to produce thermal (and then electrical) energy and tritium by the reactions with the Lithium blanket [9, 10].
In general, in a fusion reactor there will be a balance between heating and losses. The time evolution of the plasma energy density W depends on the power produced by the α-particles P_α,

$$ P_\alpha = \frac{n^2}{2}\langle\sigma v\rangle\frac{W_{DT}}{5}, \tag{1.14} $$

the power lost P_l because of *brehmsstrahlung* radiation and transport mechanisms

$$P_l = \frac{3nk_BT}{\tau_E} + bn\sqrt{T} \tag{1.15}$$

(τ_E being the energy confinement time and b a function of the effective charge Z_{eff}) and the power of other possible external heatings P_h.
The power belance, thus will be,

$$\frac{\partial W}{\partial t} = P_\alpha + P_h - P_l \tag{1.16}$$

It would be a very desirable goal if, in the regime of steady state ($\frac{\partial W}{\partial t} = 0$), fusion power was produced with no external power required to sustain the plasma ($P_h = 0$): this condition ($P_\alpha = P_l$) is called *ignition*.
More in detail, it is easy to demonstrate that after some simple algebra one obtains a condition on the product $n\tau_E$ as a function of T:

$$n\tau_E = \frac{3k_BT}{\frac{n^2}{20}\langle\sigma v\rangle W_{DT} - b\sqrt{T}} \tag{1.17}$$

As it can be seen in figure 1.4, the curve presents a minimum at about $20\,keV$.
A more compact expression to define the ignition criterion is the so-called *fusion triple product*, taking into account the minimum temperature value:

$$n\tau_E T > 3 \times 10^{21}\, m^{-3} \cdot s \cdot keV \tag{1.18}$$

This means that a promising way to access a positive power balance is to produce a plasma with a density of the order of $10^{20}\, m^{-3}$ and a temperature of $20\,keV$; moreover, the characteristic time for the thermal energy to escape to the surrounding material surfaces must exceed about 3 seconds, in order that the power produced in $\alpha-$particles can sustain the temperature of the plasma.

1.3 Magnetic plasma confinement: toroidal configurations

As mentioned in the previous section, for a significant fraction of fusion reactions to occur, the particles have to achieve high densities and temperatures for a sufficiently long time.
This critical issue is easily overcome by the Sun thanks to its huge mass and hence by *gravitational confinement*.
Clearly other solutions must be found to realize fusion conditions in the laboratory: currently, the most promising methods are the so-called inertial and

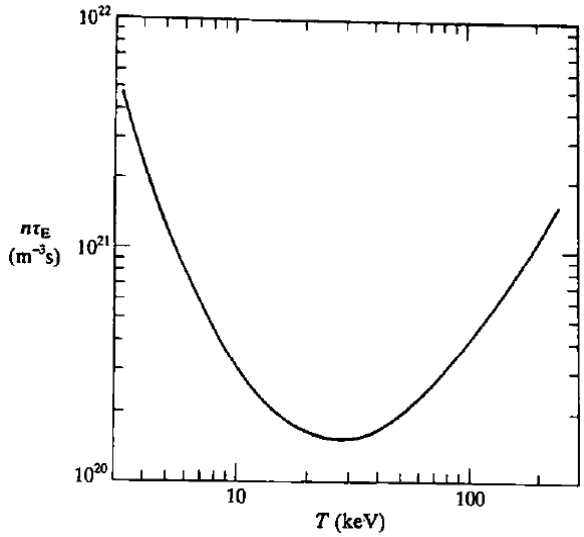

Figure 1.4: Ignition criterion: $n\tau_E$ product as function of T.

magnetic confinement fusion.
In *inertial confinement* fusion experiments [7], small targets of deuterium and tritium are uniformly radiated by high power lasers in order to compress them and to obtain the proper condition of temperature and density. Pulsed reactors, however, are not very desirable because cyclical thermal and mechanical stresses on the structure lead to increased maintenance and more frequent replacement of components due to fatigue failure.
Magnetic confinement fusion [11], on which this thesis is focused, invests strong magnetic fields to confine particles in the plasma state. It is well-known that any particle of mass m and charge q is constrained to spiral around the magnetic field lines by the Lorentz force ($m\ddot{\mathbf{r}} = q\dot{\mathbf{r}} \times \mathbf{B}$). If the magnetic field $\mathbf{B}$ is constant and uniform, the circular frequency, named *cyclotron frequency*, and the radius of the spiral, named *Larmor radius*, are respectively defined:

$$\omega_c = \frac{\mid q \mid B}{m} \qquad \text{and} \qquad r_L = \frac{v_\perp}{\omega_c} = \frac{m v_\perp}{\mid q \mid B}, \tag{1.19}$$

where $v_\perp$ is the component of the particle velocity perpendicular to $\mathbf{B}$.
The r_L is inversely proportional to the strength of the magnetic field, so in a strong field charged particles are confined on a plane perpendicular to the field (in fusion devices, tipically $r_L \sim 1\,cm$ for ions), but not along the direction parallel to $\mathbf{B}$. In order to avoid parallel losses, fusion research has been focused on the configurations in which the field lines are closed: the simplest one is a torus (see fig. 1.5b).

In fig. 1.5a the coordinate system usually adopted to describe such a geometry is shown: θ and φ are the poloidal and toroidal angles, respectively, and r is the minor radial coordinate, which spans from the centre of the plasma to the boundary ($0 \leq r \leq a$).

In a system with purely toroidal magnetic field B_φ, a magnetic field gradient

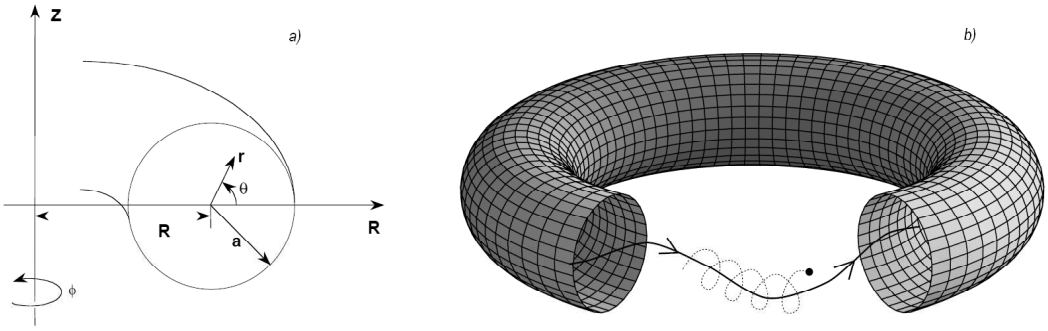

Figure 1.5: a) The system of toroidal (r, θ, φ) and cylindrical coordinates (R, φ, Z). b) A charged particle orbits around a helical magnetic field line and it is thus confined within the toroidal device.

($\mathbf{B}(R) \propto R^{-1}$, where R is the major radius of the torus) and the curvature of the lines result in a vertical drift with opposite directions for ions and electrons; the electric field resulting by charge separation causes an outward $E \times B$ drift of the whole plasma, damaging the confinement. This complication is solved twisting the magnetic field lines by adding a poloidal magnetic field, B_θ: the magnetic field lines are helical, wound around the torus lying over toroidal surfaces called *magnetic surfaces*.

Helical magnetic field lines are usually described in terms of the so-called *safety factor* q, defined as the number of toroidal turns completed by a magnetic line for the whole poloidal turn:

$$q(r) \equiv \frac{rB_\varphi}{RB_\theta}. \tag{1.20}$$

Another useful parameter, strictly linked to safety factor q is the *magnetic shear* s defined as:

$$s(r) \equiv \frac{r}{q(r)} \frac{dq(r)}{dr}. \tag{1.21}$$

The presence of a not null magnetic shear plays an important role in stabilizing MHD instabilities, particularly those driven by the pressure gradient (as will be seen in section 1.4.1).

Finally, to quantify the efficiency of plasma confinement in a magnetic

confinement configuration, it is useful to introduce the parameter *beta*:

$$\beta \equiv \frac{\langle p \rangle}{B^2/2\mu_0} \tag{1.22}$$

It represents the ratio between kinetic ($p \propto nT$) and magnetic pressure and gives an indication of the confinement properties: for stability reasons and technological limitations, in present machines, it can usually not exceed values of some percent. The magnetic configurations having a relatively high β value are thus the most convenient, because in this case the magnetic field confines the plasma more efficiently.

Different magnetic configurations have been investigated in fusion research: in this thesis we will mention the *tokamak*, characterized by a dominant toroidal magnetic field and we will focus on the *reversed-field pinch*, where B_φ and B_θ are of the same order. In both devices, a toroidal current I_p, inductively driven by an external circuit, flows through the plasma and generates a poloidal magnetic field B_θ that confines and compresses the plasma. Moreover, the toroidal magnetic field is in part generated by a system of external coils encircling poloidally the machine.
The **tokamak** [11] is, at present, the most promising fusion device: this is indeed the configuration chosen for the world's largest and most advanced experiment, called International Thermonuclear Experimental Reactor (ITER) [12]. ITER is expected to demonstrate the principle of extracting more energy out of the fusion process than that used to initiate it.
The tokamak is characterized by a relatively high toroidal magnetic field, that can reach values of several $Tesla$ in high field machine, and a much weaker (about one order of magnitude) poloidal one (see figure 1.6b). The condition $B_\varphi \gg B_\theta$ limits the toroidal current and, hence, the Ohmic heating of the plasma. In this configuration, only the B_θ component contributes to the radial confinement of the plasma, so the β parameter value is usually small (≈ 0.01): only a small fraction of the magnetic energy is used to confine and ohmically heat the plasma, while the most is required to stabilize it. For this reason, additional complex heating methods, e.g. neutral beam injection and radio-frequency heating, are needed to reach thermonuclear conditions.
The **reversed-field pinch** (RFP) configuration is extensively described in section 2.1; we will here just mention the main differences with respect to the tokamaks.
In RFP devices, B_θ is generated by the toroidal plasma current, as for tokamaks, while part of B_φ is created by the plasma itself, by means of a *dynamo* process. As seen figure 1.6a, poloidal and toroidal magnetic field components are comparable.

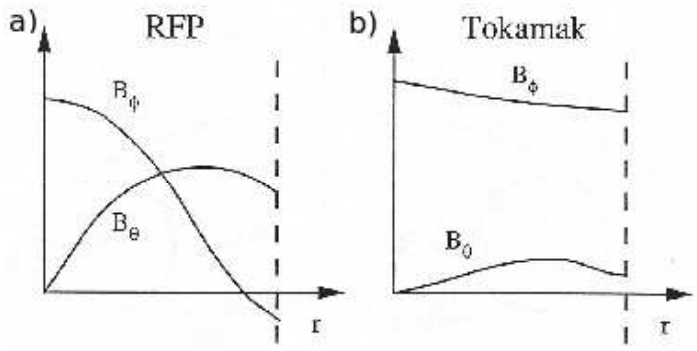

Figure 1.6: RFP (a) and tokamak (b) typical radial profiles.

Moreover, the peculiar q profile of RFP configurations (see fig. 1.6) generates a wide spectrum of MHD modes, which makes the RFP plasmas more turbulent than those confined in tokamak configurations. Nevertheless at equivalent value of externally applied magnetic field, RFP can, in principle, achieve higher plasma current allowing the reaching of ignition condition by means of ohmic heating only. Thus, higher values of β with respect to the tokamaks can be obtained ($\beta \approx 0.1$). All these considerations make the RFP an interesting alternative to tokamaks as magnetic confinement device.

1.4 Instabilities in magnetized plasmas

Various types of instabilities can occur in a plasma system: in the literature several different classification schemes have been introduced to distinguish one to the other.
A common way to classify plasma instabilities is by the driving source. Since $\nabla p = \mathbf{J} \times \mathbf{B}$ in equilibrium (*force balance equation*, eq. 1.3 in steady state conditions), instabilities driven by currents perpendicular to the main magnetic field are often called "pressure-driven" modes, while instabilities driven by the parallel currents are often called "current-driven" modes.
Another important classification discerns between ideal and resistive instabilities: the first ones would develop even if the plasma were perfectly conducting and can be very violent, the second ones depend on the presence of a not null plasma resistivity.
Both ideal and resistive instabilities have an infinite spectrum of possible modes, each one characterized by its mode numbers: a small perturbation $\tilde{\mathbf{A}}$ of any quantity $\mathbf{A}$, in a toroidal plasma, which is approximated by a periodic

cylinder, may be Fourier decomposed as

$$\tilde{\mathbf{A}}(r) = \sum_k \tilde{\mathbf{A}}_{\mathbf{k}}(r) e^{i(\mathbf{k}\cdot\mathbf{x}-\omega t)} = \sum_k \tilde{\mathbf{A}}_{\mathbf{k}}(r) e^{i(m\theta+n\varphi-\omega t)} \tag{1.23}$$

where $\mathbf{k} = (k_r, k_\theta, k_\varphi) = (k_r, m/r, n/R)$ is the wave-vector in toroidal coordinates, $\mathbf{x}$ is the position vector and m and n are the *poloidal* and the *toroidal mode numbers*, respectively. Thus, each pair (m, n) represents a helical perturbation, a mode.

For spatially uniform plasmas, small perturbations will generally have a wave-like spatial structure. In such cases, as discussed in section 1.4.2, a plane wave with a single wave-vector $\mathbf{k}$ generally has a single frequency ω: this plane wave is known as *normal mode*.
For non-uniform plasmas, e.g. those considered in the section 1.4.1, it is necessary to find the *eigenfunctions* of the normal modes of the perturbations, describing the spatial structure in the direction of non-uniformity; these modes have a single, usually complex, frequency $\omega = \omega_R + \imath\omega_I$, the real part describing the propagation velocity and the imaginary part the growth ($\omega_I > 0$) or the damping ($\omega_I < 0$) of the mode amplitude [5].

Generally, a plasma perturbation causes a bending of magnetic field lines and the instability is further stabilized by the natural behaviour of the plasma that reacts almost elastically to this bending. This stabilizing effect vanishes on the surface where the wave-front of the perturbation is parallel to the equilibrium magnetic field, $\mathbf{B} = (0, B_\theta, B_\varphi)$ in toroidal coordinates:

$$\mathbf{k}\cdot\mathbf{B} = 0 \qquad \longrightarrow \qquad \frac{m}{r}B_\theta + \frac{n}{R}B_\phi = 0 \tag{1.24}$$

Remembering the definition 1.20, the previous equation is equivalent to

$$\mid q \mid = \frac{m}{n} \tag{1.25}$$

This means that the most unstable helical instabilities are localized at radial positions where the safety factor assumes rational values. For this reason, the surfaces satisfying the eq. 1.25 are called *rational surfaces* and the instabilities defined by an (m, n) pair are called *resonant modes*. Different driving sources, generally the gradient of any physical quantity, can provide the necessary free-energy for a whatever small perturbation to grow unstable.

In the following subsections, some quite common instabilities are briefly described: they are not an exhaustive list of the main phenomena occuring in a plasma, but rather some theorical constructs about the modes that are investigated in this thesis.

1.4.1 Interchange modes

Interchange instabilities are ideal instabilities driven principally by the relaxation of pressure gradients or by expansion. The characteristic feature of the perturbation is the *interchange* of magnetic field lines without bending or otherwise distorting them in such a way as to produce a restoring magnetic force. A simple example of interchange instability, with a hydrodynamical nature, occurs when a heavier fluid is above a lighter one, i.e $\rho_1 > \rho_2$. Such an equilibrium is intuitively unstable and this is mathematically demonstrated by a linear stability theory [7]. Considering a small perturbation of the interface between the two fluids, whose complex frequency can be written as

$$\omega_I^2 = -\frac{kg(\rho_1 - \rho_2)}{\rho_1 + \rho_2}, \tag{1.26}$$

it can be seen that ω has a positive, imaginary solution when the denser fluid is above the thiner. The instability that arises is known as the *Rayleigh-Taylor instability*. Whereas Rayleigh's analysis [13] was for fluids in a gravitational field, Taylor [14] adapted the problem to the situation of accelerating fluids, thus these modes are also known as *g-modes*, where g stays for *gravity*.

In astrophysical plasmas, it is common to find a fluid accelerating against

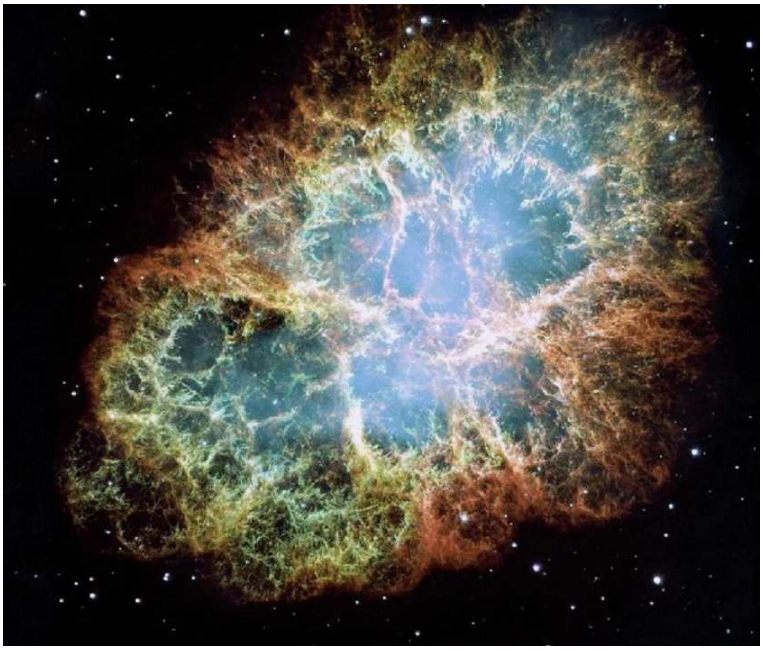

Figure 1.7: Optical photo of the Crab Nebula: it shows an intriguing filamentary structure.

a heavier one [15], for example in a supernova explosion, at the interface between the hot gas ejected in the explosion and the surrounding interstellar medium. Gull's studies [16] showed that the ejected gas, piled up in a thin shell behind the interface, gives rise to the Rayleigh-Taylor instability and lead to the formation of filaments growing in the outward direction. Figure 1.7 is a photograph of the Crab Nebula (the remnant of a supernova observed from the Earth in 1054) presenting the filamentary structure mentioned.
The MHD analogue of the Rayleigh-Taylor instability occurs when a plasma is supported against gravity by a magnetic field. In laboratory plasmas, gravity is of no significance, but particles moving in curved magnetic fields are affected by a centrifugal force which acts like an equivalent gravitational force. To discuss the instability qualitatively we refer to figure 1.8a that is characterized by a plane geometry: this minimizes the algebra without losing the essential physics.

Any charged particle, with mass M, moving along a curved field line with velocity $v_\parallel$, feels a centrifugal force $\mathbf{F} = Mv_\parallel^2 \mathbf{R_c}/R_c^2$, where $\mathbf{R_c}$ is a vector from the local centre of curvature to the position of the charge. Moreover, it is simple to demonstrate [7] that the particle, in the presence of a force F perpendicular to the main magnetic field, is subject to a drift velocity, that in our case is the so-called *curvature drift*,

$$\mathbf{v_c} = \frac{\mathbf{F} \times \mathbf{B}}{eB^2} = \frac{Mv_\parallel^2}{e} \frac{\mathbf{R_c} \times \mathbf{B}}{R^2 B^2}. \tag{1.27}$$

Consider a small wave-like ripple developing on the interface between the two plasmas having different densities, as shown in figure 1.8b; then, since $\mathbf{v_c} \propto M$, the ions in the plasma are evidently more affected by the drift than electrons. This causes positive charge to build up on one side of the ripple, as illustrated in the picture, while the depletion of ions causes a negative charge to build up on the other side of the ripple (obviously the drift operates on both plasma sides of the interface, but being $\rho_1 > \rho_2$, we consider the net effect). Due to this charge separation, a small electric field $\mathbf{E}$ develops, having different sign going from the crest to the trough of the perturbation. It is evident that the resulting $\mathbf{v_E} = \mathbf{E} \times \mathbf{B}/B^2$ is directed so that the initial ripple grows larger: $\mathbf{E} \times \mathbf{B}$ drifts are phased so as to amplify the initial perturbation [7].
Concluding, if the field lines curve towards the surface of the plasma, this corresponds to *unfavourable* curvature: because of the curvature direction an outward bulge on the surface places the plasma in a lower-field region, which tends to enhance the bulge. Conversely, when the field lines curve away from the surface of the plasma, the curvature is *favourable*: in this case an outward bulge of the surface places the plasma in a region of higher magnetic field, that tends to restore the plasma to its equilibrium position and it is thus stabilizing.

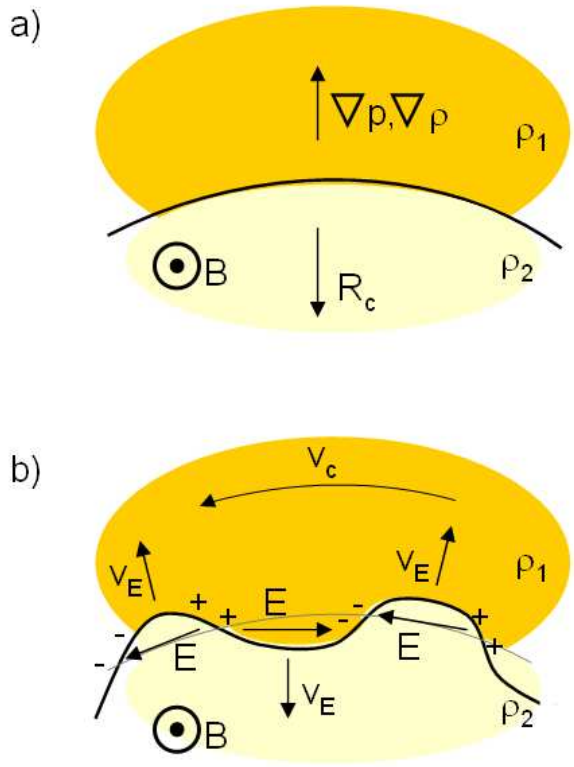

Figure 1.8: a) A denser plasma (ρ_1) is supported against centrifugal force by a magnetic field **B** perpendicular to the curved interface; b) A small perturbation and the curvature drift v_c generate a charge separation, causing the drift v_E that enhances the perturbation.

1.4.2 Alfvén waves

Electromagnetic waves in a highly conducting fluid in a uniform magnetic field were first investigated by Alfvén [17]. Alfvén waves are found to be characterized by a continuous spectrum of frequencies and some discrete solutions which constitute the Alfvén eigenmodes.
In this chapter, a brief review of the theory of Alfvén waves is presented [18, 9]. The ideal MHD stability theory shows that the plasma can support three different types of stable waves: the **Shear Alfvén Waves**, SAW, the **Compressional Alfvén Waves**, CAW (sometimes called the fast magnetosonic waves), and the **Sound Waves**, SW, (sometimes called the slow magnetosonic waves).

We can take into account the MHD equations (1.2-1.8), in the case of an infinite homogeneous non-conductive plasma: they are non-linear, but in

order to simplify them, it is possible to analytically treat only the case of linear stability, i.e. stability against infinitesimally small disturbances, in relatively simple geometries. For this purpose, any quantity f is written as the sum of an equilibrium time-independent term, f_0, and of a small first-order time-dependent perturbation, $\tilde{f}$:

$$f(r,t) = f_0(r) + \tilde{f}(r,t) \tag{1.28}$$

Without losing in generality, we can choose $\mathbf{B} \parallel \hat{\mathbf{e}}_\mathbf{z}$ and the wave-vector $\mathbf{k}$ lying in the $y-z$ plane: thus, the component of the wave-vector $\mathbf{k}$ parallel to the main magnetic field $\mathbf{B_0}$ is $k_\parallel = \mathbf{k}\cdot\mathbf{B_0}/\mid \mathbf{B_0} \mid = \mathbf{k_z}$ and the perpendicular one is $k_\perp = k_y$, being $\mid \mathbf{k} \mid = \sqrt{k_\parallel^2 + k_\perp^2} = \sqrt{k_z^2 + k_y^2})$. Moreover, since the equilibrium is static, $\mathbf{v_0} = 0$.
The linearized equations of ideal MHD, then, become

$$\frac{\partial\tilde{\rho}}{\partial t} + \nabla\cdot(\rho_0\tilde{\mathbf{v}}) = 0 \tag{1.29}$$

$$\rho_0\frac{\partial\tilde{\mathbf{v}}}{\partial t} = \tilde{\mathbf{j}}\times\mathbf{B_0} + \mathbf{j_0}\times\tilde{\mathbf{B}} - \nabla\tilde{p} \tag{1.30}$$

$$\tilde{\mathbf{E}} + \tilde{\mathbf{v}}\times\mathbf{B_0} = 0 \tag{1.31}$$

$$\nabla\times\tilde{\mathbf{B}} = \mu_0\tilde{\mathbf{j}} \tag{1.32}$$

$$\nabla\times\tilde{\mathbf{E}} = -\frac{\partial\tilde{\mathbf{B}}}{\partial t} \tag{1.33}$$

$$\nabla\cdot\tilde{\mathbf{B}} = 0 \tag{1.34}$$

$$\frac{\partial\tilde{p}}{\partial t} = -\tilde{\mathbf{v}}\cdot\nabla p_0 - \gamma p_0\nabla\cdot\tilde{\mathbf{v}}. \tag{1.35}$$

The last relation arises from $\partial p/\partial t = -\gamma p\nabla\cdot\mathbf{v}$, that can be easily derived from the state equation 1.8, using the mass continuity 1.2, in the case of uniform plasma.
At this point we introduce the *displacement vector field*, ξ, representing the perturbed shift of the plasma away from its equilibrium position, for which is

$$\tilde{\mathbf{v}} = \frac{\partial\xi}{\partial t}. \tag{1.36}$$

Substituting 1.36 in the equations 1.29, 1.33 (combined with 1.31) and 1.35 and integrating them in time, we obtain respectively:

$$\tilde{\rho} = -\nabla\cdot(\rho_0\xi) \tag{1.37}$$

$$\tilde{\mathbf{B}} = \nabla \times (\xi \times \mathbf{B_0}) \tag{1.38}$$

$$\tilde{p} = -\xi \cdot \nabla p_0 - \gamma p_0 \nabla \cdot \xi \tag{1.39}$$

Inserting the above relations into the equation of motion 1.30 and supposing that at equilibrium $\mathbf{j_0} = 0$ and p_0, ρ_0 and $\mathbf{B_0}$ are constants, we obtain the *force operator* formulation:

$$\rho_0 \frac{\partial^2 \xi}{\partial t^2} = \frac{\nabla \times [\nabla \times (\xi \times \mathbf{B_0})]}{\mu_0} \times \mathbf{B_0} + \gamma p_0 \nabla (\nabla \cdot \xi) \tag{1.40}$$

The most general form of the perturbation for the infinite homogeneous plasma can be written as

$$\xi(\mathbf{r}, t) = \hat{\xi}\, e^{\imath(\mathbf{k}\cdot\mathbf{r} - \omega t)} \tag{1.41}$$

where $\hat{\xi}$ is a complex amplitude. The 1.41 are exact solutions to the linearized partial differential equations: by using it, the 1.40 is easily derived by noting that each time derivative and each gradient operator produce respectively the multiplicative factors:

$$\frac{\partial}{\partial t} \to -\imath\omega \qquad\qquad \nabla \to \imath\mathbf{k} = \imath k_\parallel \hat{\mathbf{e}}_\mathbf{z} + \imath k_\perp \hat{\mathbf{e}}_\mathbf{y} \tag{1.42}$$

and the exponential factor can be canceled from each term.
Thus, the Fourier trasformed force operator is:

$$\rho_0 \omega^2 \hat{\xi} = \frac{1}{\mu_0} \mathbf{k} \times [\mathbf{k} \times (\hat{\xi} \times \mathbf{B_0})] \times \mathbf{B_0} + \gamma p_0 \mathbf{k} (\mathbf{k} \cdot \hat{\xi}) \tag{1.43}$$

The equation 1.43 can be rewritten as a set of scalar equations for the three vector components. The resulting terms can be cast in matrix form:

$$\begin{pmatrix} \omega^2 - k_\parallel^2 v_A^2 & 0 & 0 \\ 0 & \omega^2 - k_\parallel^2 v_A^2 - k_\perp^2 v_S^2 - k_\parallel k_\perp^2 v_S^2 & -k_\parallel k_\perp^2 v_S^2 \\ 0 & -k_\parallel k_\perp^2 v_S^2 & \omega^2 - k_\parallel^2 v_S^2 \end{pmatrix} \begin{pmatrix} \hat{\xi}_x \\ \hat{\xi}_y \\ \hat{\xi}_z \end{pmatrix} = 0. \tag{1.44}$$

It is useful to remind that

$$v_A = \frac{B_0}{\sqrt{\mu_0 \rho}} \tag{1.45}$$

is the *Alfvén velocity* and

$$v_S = \sqrt{\frac{\gamma p_0}{\rho}} \tag{1.46}$$

is the *adiabatic sound speed.*
Non-trivial solutions exist only when the determinant of the matrix is zero, which leads to the equation:

$$(\omega^2 - k_\parallel^2 v_A^2) \left[(\omega^2 - k^2 v_A^2 - k_\perp^2 v_S^2)(\omega^2 - k_\parallel^2 v_S^2) - (k_\parallel k_\perp v_S^2)^2 \right] = 0 \tag{1.47}$$

It is clear from a simple investigation that the determinant is cubic in ω^2. This implies that there are three separate roots for ω^2, corresponding to the three MHD waves previously mentioned:

- The **Shear Alfvén waves** (SAW) corresponding to a stable oscillatory wave.

$$\omega^2 = k_\parallel^2 v_A^2 \tag{1.48}$$

  The dispersion relation 1.48 is independent of the perpendicular component of the wave-vector component perpendicular to the magnetic field $k_\perp$ and of the sound velocity v_S.

The *fast* and *slow magnetosonic waves* are two further branches arising from eq. 1.47:

$$\omega^2 = \frac{k^2}{2}(v_A^2 + v_S^2)\left[1 \pm \sqrt{1-\tilde{\alpha}}\right] \quad \text{where} \quad \tilde{\alpha} = \frac{k_\parallel^2}{k^2}\frac{4v_A^2 v_S^2}{(v_A^2+v_S^2)} \leq 1 \tag{1.49}$$

- The fast magnetosonic wave corresponds to the $+$ sign in eq. 1.49. The physics can be pointed out by noting that $v_S^2/v_A^2 = \gamma\mu_0 p_0/B_0^2 \approx \beta$ (defined in 1.22) and then considering the limit $\beta \ll 1$: this is equivalent to assuming that $\tilde{\alpha} \ll 1$. The eigenfrequency in this case reduces to

$$\omega^2 = k^2 v_A^2 \ , \tag{1.50}$$

  i.e. the dispersion relation of the so-called **Compressional Alfvén Waves** (CAW) [19]. It is very stable for $k_\parallel << k_\perp$ and therefore is only weakly excited in most plasma conditions.

- The negative root in 1.49 gives rise to the slow magnetosonic wave: in the low$-\beta$ limit it becomes

$$\omega^2 = k_\parallel^2 v_S^2 \ , \tag{1.51}$$

  describing the **Sound Waves**, that are not usually strongly excited in most of the plasmas.

1.4.3 Tearing modes

The theory of **resistive tearing instabilities**, including their surprisingly large growth rates with respect to the characteristic time for resistive diffusion of plasma across a magnetic field, was developed first in a paper by H.P. Furth,

J. Killeen and M.N. Rosenbluth (1963) [20].
The tearing modes are driven unstable by the radial gradient of the equilibrium current density parallel to the magnetic field [11, 5]. The name of this instability comes from the fact that the magnetic field lines tear and reconnect during their evolution as a consequence of finite resistivity. This occur when, somewhere in the plasma, the convection term in eq. 1.9 vanishes and the diffusion term, however small, comes locally into play: the resistivity can be destabilizing since it frees the plasma from the constraint to remain "frozen" to the magnetic field. The simplest magnetic configuration in which a resistive tearing instability can occur is the "plasma current slab". Specifically, an infinite plasma that contains a finite slab of current, directed parallel to the surface of the slab is considered. Solving Ampère's law, the sheared magnetic field shown in figure 1.9a, is obtained: such a magnetic configuration is produced by the current profile with the gradient localized where the $B_y(x)$ component changes its sign at x_r.

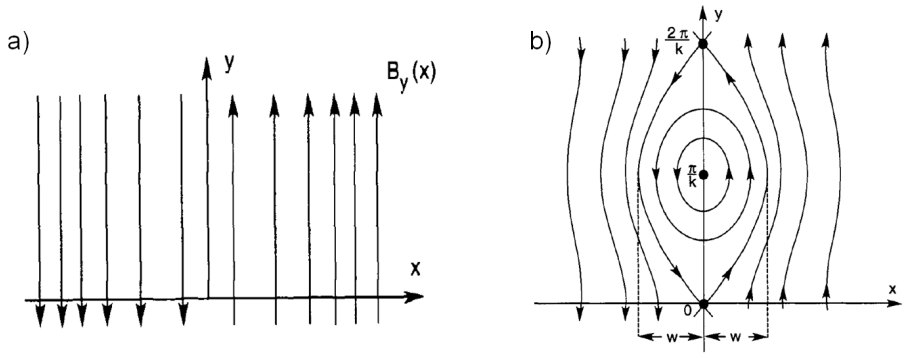

Figure 1.9: (a) Magnetic field lines for the "plasma current sheet" equilibrium. (b) Perturbed field line configuration of magnetic islands produced by a resistive tearing instability.

Neglecting the plasma resistivity, this field configuration represents a stable equilibrium state, assuming that we have normal pressure balance across the interface, by means of the occurence of a suitable pressure profile or of a strong perpendicular magnetic field, B_z.
On the contrary, the presence of resistivity in the slab makes the destabilization of tearing modes possible. In particular, by using a perturbative approach as in the previous section, 1.4.2, it can be seen that the x-component of the induction equation 1.9 can be written as

$$\frac{\partial \tilde{B}_x}{\partial t} = [\nabla \times (\tilde{\mathbf{v}} \times \mathbf{B})]_x + \frac{\eta}{\mu_0} \nabla^2 \tilde{B}_x \tag{1.52}$$

in the system here considered. In particular, since resistivity is important only in a narrow region around x_r, within which B is relatively sharply varying, and, on the other hand the tearing instability, in contrast to the resistive interchange instability, is related to long wavelength [21], the 1.52 can be approximated to

$$-\imath\omega\tilde{B}_x = \frac{\eta}{\mu_0}\frac{\partial^2\tilde{B}_x}{\partial x^2}. \tag{1.53}$$

where the same approach of the previous section (in particular, eq. 1.42) has been used.
Although B_y is continuous across the boundary layer ($B_y(x_r) = B_y(x_r^-) = B_y(x_r^+)$), its gradient in x_r is not. Thus, in order to obtain a stability relation, it is useful to consider the quantity

$$\Delta' = \frac{1}{\tilde{B}_x}\left(\frac{\partial\tilde{B}_x}{\partial x}\Big|_{x_r^-} - \frac{\partial\tilde{B}_x}{\partial x}\Big|_{x_r^+}\right). \tag{1.54}$$

Δ' is the **classical stability index** defined as the logarithmic jump of the radial magnetic field perturbation across the rational surface. So, since $\partial^2\tilde{B}_x/\partial x^2 \approx (\Delta'\tilde{B}_x)/(\epsilon L)$, where ϵ represents a unitary x coordinate inside the layer and L indicates the size, substituting into formula 1.53, yields

$$-\imath\omega \approx \frac{\eta}{\mu_0}\frac{\Delta'}{\epsilon L} = \frac{\Delta' L}{\epsilon\tau_R}. \tag{1.55}$$

This means that the tearing instability appears when $\Delta' > 0$.

The inclusion of plasma resistivity allows the negative B_y field to diffuse into the region of positive B_y field, thereby annihilating it. It is easy to see that this annihilation of magnetic field is energetically favored: if we consider the modification of $B_y(x)$ that would result from cancellation of the positive and negative components in some small region localized around x_r, it is clear that the magnetic energy, $\int(B_y^2/2)dV$, would be reduced. The magnetic energy released during the reconnection process eventually appears as plasma thermal energy. The magnetic configuration resulting from the breaking and the reconnection of the magnetic field lines, is characterized by the formation of a so-called *magnetic island*, as represented in figure 1.9b.
Such fast reconnections (on time scales between τ_A and τ_R) taking place at current sheets are important for violent events like solar flares on the one hand and major disruptions in tokamaks on the other.

The RFP configuration and the RFX-mod experiment

In this chapter an introduction about the RFP configuration and its main features is presented. In particular, the experiment RFX-mod operating in Padova, the device where the bulk of the experimental results presented in this thesis has been obtained, is described. The last section (2.3) concerns EXTRAP T2R, an RFP machine operating in Stockholm, where I have been engaged for a two-months experimental campaign performed in March and April 2011.

2.1 The dynamo effect and the RFP configuration

The Reversed Field Pinch (RFP) [22] is a toroidal axisymmetric configuration, in which plasma confinement arises from a combination of a poloidal magnetic field, created by the toroidal plasma current, and a toroidal magnetic field, generated by both the plasma current and external coils.
The term *pinch* defines any linear or toroidal plasma where the plasma column shrinks due to the Lorentz force generated by the interaction of a current carried by the plasma and the magnetic field it induces. The RFP is characterized by its natural tendency to relax in a configuration in which the toroidal field component reverses near the plasma edge, as the name *reversed-field* suggests. This phenomenon was observed for the first time on the experiment ZETA at Harwell in the middle of the sixties [23], but a theory for relaxed states was given only in 1974 by J.B. Taylor [24] and in a more precise form in 1986 [25]. This theory is based on a variational principle.
The main constructs about this historical theory are given in the follow. As mentioned at the end of the section 1.1, in the case of ideal MHD approximation, the magnetic topology is preserved in a magnetofluid. Thus, we expect

that the *magnetic helicity*, defined as

$$\mathcal{H} = \int_V \mathbf{A} \cdot \mathbf{B} d^3x, \tag{2.1}$$

where $\mathbf{A}$ is the *vector potential* of the magnetic field ($\mathbf{B} = \nabla \times \mathbf{A}$) and V is the plasma volume, would be an invariant for an ideal plasma: $d\mathcal{H}/dt = 0$. This was demonstrated by Woltjer in 1958 [26]. Moreover, Woltjer showed that the magnetic configuration that minimizes the magnetic energy preserving the helicity, is a *force-free* magnetic field satisfing the equation

$$\nabla \times \mathbf{B} = \mu \mathbf{B} \tag{2.2}$$

with μ necessarily uniform along the magnetic field lines.
In real plasmas, μ is not uniform, but presents a radial profile and the magnetic distribution is not purely force-free ($\nabla p \neq 0$).
Taylor's theory is based on the conjecture that, in low-β plasmas, the magnetic helicity is constant (or it does not change much) during plasma relaxation to the equilibrium.
In the limit of large *aspect ratio* (the ratio between the major and the minor radius, R/a), a good approximation for toroidal geometry will be the cylindrical one with periodic boundary condition. Thus, in a cylindrical approximation, it is straightforward to demonstrate that a solution for the linear equation 2.2 becomes:

$$B_r(r) = 0, \qquad B_\theta(r) = B_{\theta 0} J_1(\mu r), \qquad B_\varphi(r) = B_{\varphi 0} J_0(\mu r) \tag{2.3}$$

where J_0 and J_1 are the *Bessel functions* of zero and first order respectively; this model is known as the *Bessel function model* (BFM). Taylor gives an explanation for the final relaxed state, but does not specify the nature of the relaxation. Moreover, it has been demonstrated [27] that the μ profile in a turbulent plasma is uniform even without the necessity of Taylor's teory.

According to the linear MHD theory, in a resistive plasma the currents would decay with the characteristic resistive time τ_R (defined in 1.11), which would flatten the toroidal field profile and lose the magnetic reversal. On the other hand, the experimental evidence demonstrates that, generally, the RFP configuration lasts as long as the plasma current is sustained, thus longer than the predictive resistive diffusion time.
This suggests that some mechanism is necessary to regenerate the positive toroidal field in the centre and to maintain the configuration against resistive diffusion: it must convert the poloidal magnetic flux, produced by the external

circuit, into toroidal flux, by means of a poloidal current flowing in the plasma. The drive of this poloidal current is know as the classical *dynamo* [28].
The study of the dynamo effect rose from the observation of an astrophysical phenomenon: the magnetic field of celestial bodies presents a regeneration that balances the resistive decay. The original mathematical treatment of Parker (1955) [29, 8] was improved by Steenbeck, Krauser and Rädler (1966) [30]: it is a statistical model based on the average proprieties of the turbulence, named the *mean field magnetohydrodynamics* theory. In this model, the dynamo is originated by plasma turbulent motions ($\tilde{\mathbf{v}}$ and $\tilde{\mathbf{B}}$ are the fluctuating components of the velocity and of the magnetic field respectively, as defined in eq. 1.23), from which an additional source of mean current comes to life in the Ohm's law as written in eq. 1.4:

$$\mathbf{E} + \mathbf{v} \times \mathbf{B} + \mathbf{E_D} = \eta \mathbf{j} \qquad \text{where} \qquad \mathbf{E_D} = \langle \tilde{\mathbf{v}} \times \tilde{\mathbf{B}} \rangle. \tag{2.4}$$

E_D is the *dynamo electric field*, generated by the correlation between $\tilde{\mathbf{v}}$ and $\tilde{\mathbf{B}}$.
A bath of magnetic turbulence was, thus, considered to be intrinsic to the RFP, being necessary for the dynamo. This was supported by the Taylor theory of magnetic plasma relaxation and by numerical simulations of the MH state [31]. Nevertheless, it has been predicted [32, 33] that the RFP configuration can exist also in the chaos-free *single-helicity* condition, where only one of the core-resonant resistive modes would provide the dynamo term. A short description about the occurrence of a similar configuration in RFX-mod plasma is given in section 2.2.2.

The RFP configurations are commonly described by two parameters: the *reversal* and the *pinch* parameters are respectively,

$$F = \frac{B_\varphi(a)}{< B_\varphi >} \qquad \text{and} \qquad \Theta = \frac{B_\theta(a)}{< B_\varphi >}, \tag{2.5}$$

where the brackets $\langle ... \rangle$ indicate the average over the plasma cross-section:

$$\langle \mathbf{B}_\varphi \rangle = \frac{1}{\pi a^2} \int_0^a \mathbf{B}_\varphi 2\pi r dr. \tag{2.6}$$

The most common way to display the BFM model predictions is the $F - \Theta$ diagram (fig. 2.1), in which RFP states are supposed to exist for $\Theta > 1.2$. The experimental points overplotted in the graph show a qualitatively reasonable agreement. However, other more sophisticate models can obtain a better matching: they are usually phenomenological models taking into account a

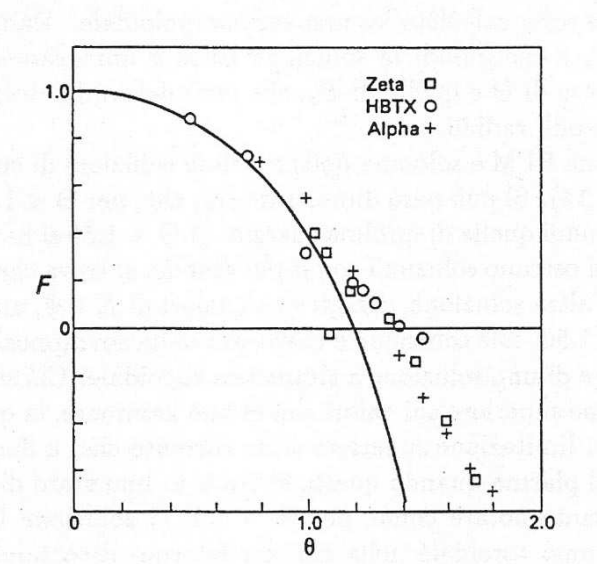

Figure 2.1: $F-\Theta$ diagram as predicted by the BFM model (continuous line) and experimental values found in different RFP devices.

$\mu = \mu_0 \mathbf{j} \cdot \mathbf{B}/B^2$ parameter having a radial dependence, e.g. [34].

Nowadays, the operating RFP machines are the Swedish, recently rebuilt, EXTRAP T2R (described more in detail in section 2.3) and two machines comparable to a medium-sized tokamak: MST [35] and RFX-mod (see section 2.2).
In fig. 2.2a the typical magnetic field profiles for the RFP equilibrium are shown. As mentioned at the beginning of this section, in this configuration the poloidal current gives rise to the peculiar radial profile of the toroidal field, with a reversal in the outer plasma region. Moreover, from fig. 2.2b, it can be noted that the safety factor $q(r)$ is everywhere lower than 1: the small value of $q(0)$ allows the destabilization of all the $m = 1$, $\mid n \mid < n_0$ modes, where $n_0 \approx 2R/a$ [36] is the inner resonant mode (thus $n_0 \approx 8$ in RFX and $n_0 \approx 13$ in EXTRAP T2R). Moreover, among all rational surfaces, we have to mention the *reversal surface* where the toroidal magnetic field cancels out (thus, $q = 0$ and $F = 0$): this surface is naturally unstable to $m = 0$ modes.

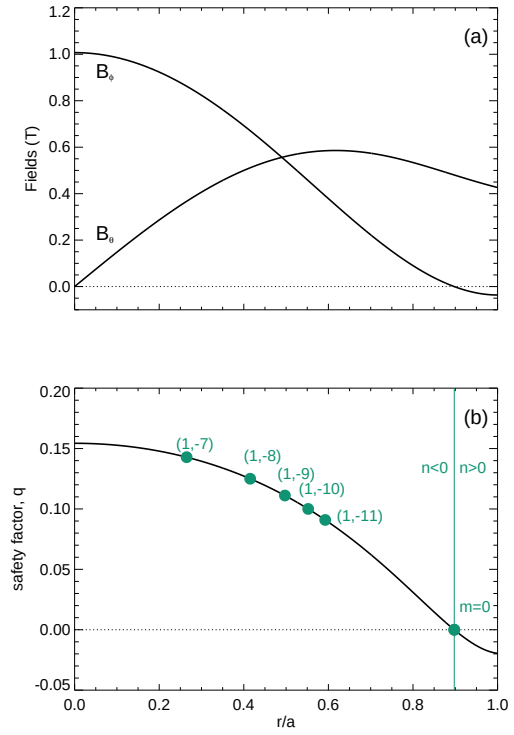

Figure 2.2: Typical poloidal and toroidal magnetic fields (a) and q profiles (b) in a RFP configuration. Some resonant modes are also indicated: the convention for the sign of the modes is that used in RFX-mod; at the reversal surface ($q = 0$) $m = 0$ modes arise.

2.2 RFX-mod experiment

2.2.1 The machine

The work described in this thesis has been carried out on RFX-mod (*Reversed Field eXperiment* modified [37]), the largest RFP device currently operating (see the photographic view in figure 2.3).

It is the upgraded version of the previous RFX [37], a toroidal device for the study of the magnetically confined plasmas in the RFP configuration.

Located at the Istituto Gas Ionizzati (IGI) [1], inside the italian Consiglio Nazionale delle Ricerche (CNR) area, in Padova, it is operational since 2004 under the management of the Consorzio RFX, a research organization promoted by CNR [38], ENEA (the italian National Agency for the new technologies, Energy and sustainable economic development) [39], the University of Padova [40], INFN [41] (italian National Nuclear Physics Institute) and

Figure 2.3: The RFX-mod machine.

Acciaierie Venete S.p.A.(a private partner) [42], within the framework of the Euratom-ENEA Association.
Consorzio RFX primary goals are focused on the scientific and technological research activity in the field of controlled thermonuclear fusion and the development of new equipment and diagnostic devices devoted to it.

The main parameters of the machine are listed in the Table 2.1. The aspect

Major radius	$= 2\ m$
Minor radius	$= 0.459\ m$
Plasma current	$\leq 2\ MA$
Discharge duration	$\leq 0.5\ s$
Plasma density range	$\approx 1 \div 10 \times 10^{19}\ m^{-3}$
Plasma volume	$\approx 10\ m^3$
Working gas	H, He

Table 2.1: Main parameters of RFX-mod device.

ratio for RFX-mod is relatively high ($R/a \approx 4$), so the cylindrical approximation can be applied, when it is helpful to simplify the geometry.

The main components of the machine, schematically shown in figure 2.4, follow [1, 43]:

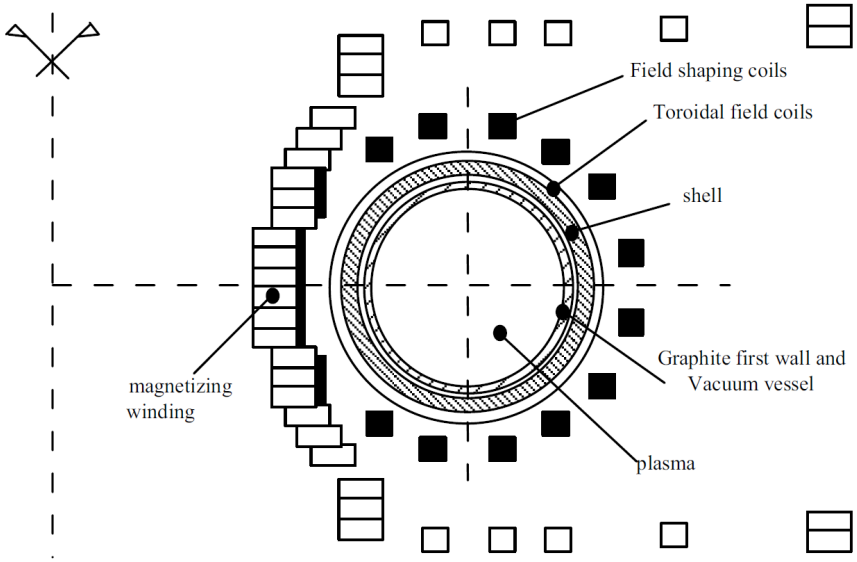

Figure 2.4: Schematic poloidal section of RFX-mod machine

- the **vacuum vessel** is a rigid toroidal structure, with major radius $R = 1.995\ m$ and minor radius $a = 0.459\ m$, realized in a non-magnetic alloy material, Inconel 625, which has been chosen because of its high electrical resistivity and its mechanical proprieties. It is provided with 12 pumping ports in the equatorial plane plus various other ports for diagnostic access;
- the **first wall** is composed by 2016 trapezoidal graphite tiles, 18 mm thick in radial direction, that protect the vacuum vessel from the plasma. The choice of graphite is due to the necessity of using low atomic number material, in order to keep the radiation as low as possible, and to have a good thermal shock resistance;
- the **stabilizing shell** is a copper structure, 3 mm thick, located just outside the vacuum vessel. It has a toroidal gap, on the equatorial plane, and a poloidal one, in order to allow the magnetic flux and toroidal electric field penetration respectively: the time constant for penetration of vertical magnetic field is $\approx 50\ ms$;
- the **toroidal field windings** consists of 48 coils evenly distributed and partially inserted into grooves machined in the stabilizing shell. The

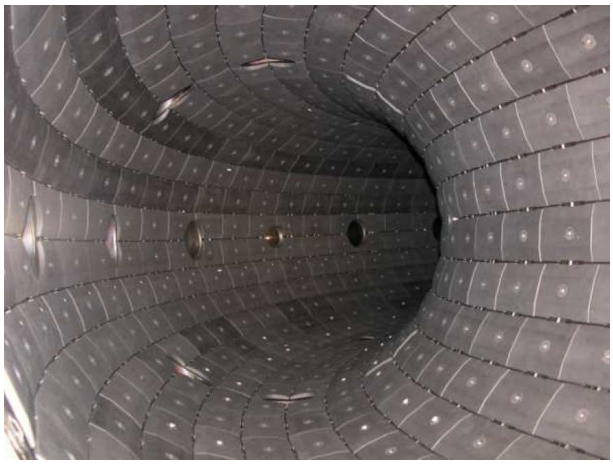

Figure 2.5: Graphite tiles in RFX-mod machine

maximum toroidal bias field is $B_0 = 0.7\ T$ at the beginning of the plasma pulse and a reversed field at the wall $B_w = 0.44\ T$ during the plasma current flat-top;

- the **magnetizing winding** provides the poloidal flux swing which causes the plasma current rise up to 2 MA. A number of 200 turns is wound to form 40 coils, each carring a maximum current of 50 kA;
- the **field shaping windings** are 16 coils providing a vertical magnetic field which guarantees the correct plasma position inside the vacuum vessel;
- the **active control system** is highly advanced: it is formed by 192 active saddle coils [37], covering the whole plasma boundary (see figure 2.6), each one operating indipendently. The *Clean Mode Control* algorithm (CMC) allows to mitigate the radial magnetic field at the edge and, thus, to drastically improve the performance of the device [44]. This feedback system is indeed essential to reach the improved-confinement regimes presented in the following section (2.2.2).

2.2.2 The plasma core

In the last years, the description of an RFP as an axisymmetric configuration, as reported in the previous section, has been found to be not complete. Spontaneous transitions to different equilibria, with a change of magnetic topology and an improved confinement, occur as the plasma current is increased. A

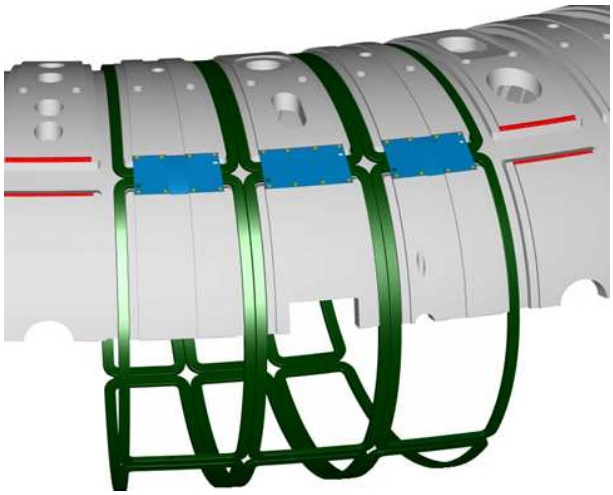

Figure 2.6: Saddle coils in RFX-mod machine

brief introduction to this topic and its effects on plasma core features is here given.
As previously mentioned, many modes with $m = 1, n > 1/q(0)$ are suited to be destabilized in an RFP device. In particular, in RFX-mod convention, the relation 1.25 is written as $q = -m/n$; for this reason, in fig. 2.2b, the n values of the resonant modes are negative inside the reversal surface and positive outside: the reversal surface represents a sort of limit which separates the central 'core' from the external region. It also constitutes an accumulation surface for the $m = 1$ modes, generating a wide spectrum of MHD activities. These modes, on the one hand, sustain the RFP configuration by the dynamo self-organization process, on the other hand, they give rise to overlapping magnetic islands, due to the closeness of rational surfaces, which result in a broad chaotic region. This condition is generally dubbed as the *multiple-helicity* (MH) state. The MH state is characterized by the presence of several $(1, n)$ normal modes, named also helicities, with similar time-fluctuating amplitudes in the magnetic spectrum; this is evident from figure 2.8, where a typical magnetic spectrum of the $m = 1$ modes in MH state is shown. In this state, the magnetic chaos, a region of overlapping of many incoherent modes, reigns, since the magnetic surfaces are suppressed in most of the plasma core. Moreover, various helicities can *lock in phase*, producing a toroidally localized deformation of the plasma column, called *phase locking*, as shown in fig. 2.7a. The locking process causes a discharge degradation because of strong localized plasma-wall interaction, intense heating of the graphite tiles and unwanted influx of gas and impurities from the tiles. These features are not favourable to good confinement.
Nevertheless, as mentioned in Sec. 2.1, it has been predicted the existence of

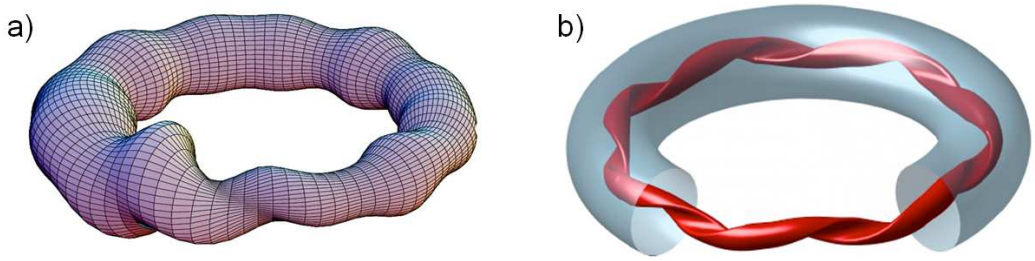

Figure 2.7: a) In Multiple Helicity state, the modes can lock in phase causing the deformation of the plasma column. b) In Single Helicity state, a helical ohmic equilibrium is self-sustained by a single mode.

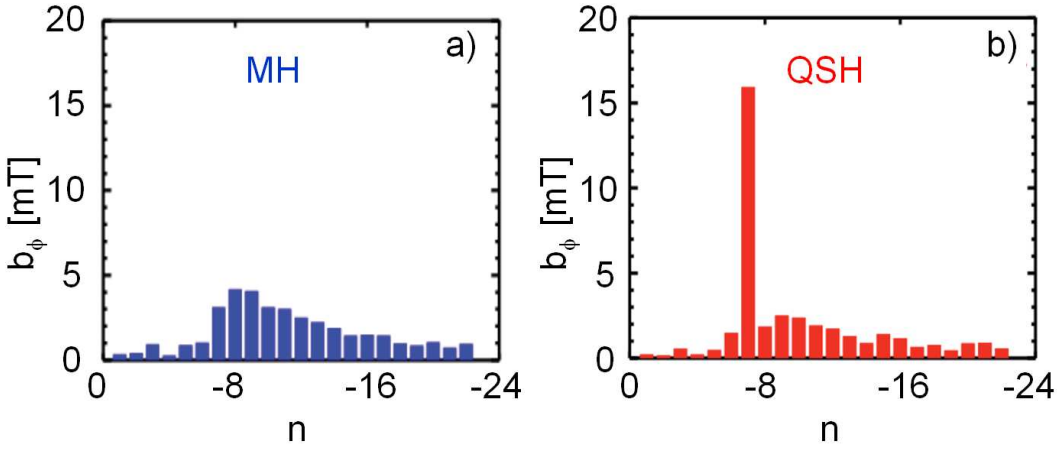

Figure 2.8: Toroidal mode number spectra of $m = 1$ modes in a typical RFX-mod discharge in MH (a) and in QSH (b) states.

a *single-helicity* (SH) configuration, characterized by the occurence of only one resonant mode providing the dynamo term. Up to now, the best experimental approximation of single helicity is the *quasi-single helicity* (QSH) state, where the most inner resonant $m = 1$ mode dominates over the other, so-called, secondary modes [45, 46]. An example of the toroidal mode spectrum in QSH regime is shown in fig. 2.8b: it is worth noting that the dominant mode in the RFX-mod device is the $(m, n) = (1, -7)$.
The achievement of the QSH state has been made possible by the operation at higher plasma current levels. The novel results are that, as the current is raised, the plasma exhibits an increasing probability of transition to the improved-confinement state (the normalized secondary modes amplitude is reduced), with only occasional occurrences of MH.
An example of a high plasma current discharge is shown in figure 2.9a; more-

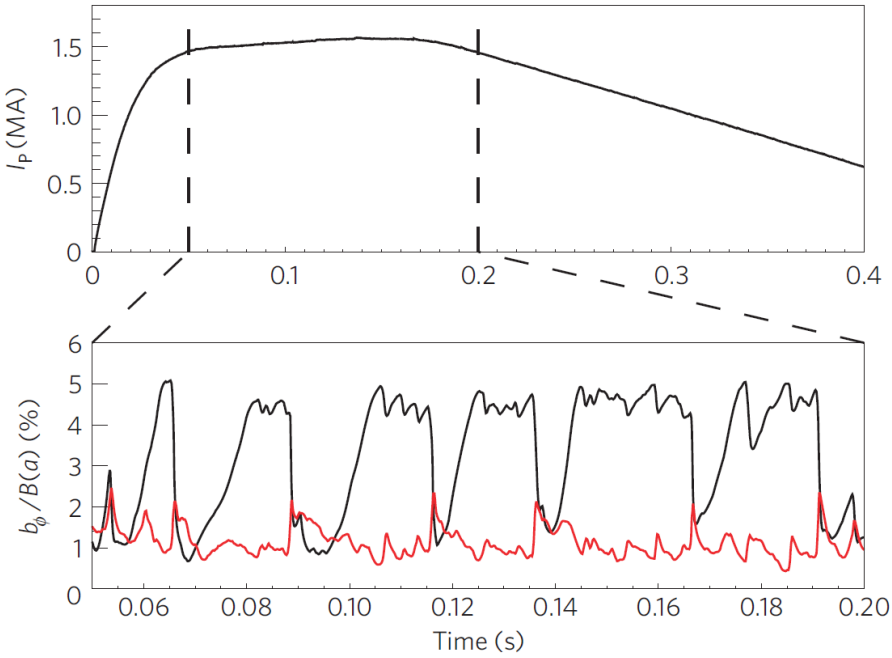

Figure 2.9: a) Plasma current as a function of time. The vertical dashed lines delimit the current flat-top phase. b) Amplitude of the $(m, n) = (1, -7)$ dominant mode (black curve) and of the secondary modes $(1, 8 \div 23)$ (red curve).

over, the dominant and secondary modes are compared during the flat-top phase of the current, in figure 2.9b. The black curve represents the normalized amplitude of the dominant mode and the red one the normalized amplitude of the secondary modes, defined as

$$b_\Sigma = \sqrt{\sum_{i=8}^{23} b_i^2}. \tag{2.7}$$

The amplitudes are those of the toroidal magnetic field component at the plasma surface, as obtained with a Fourier transform in space of the signals given by a system of 48×4 pick-up coils located outside the vacuum vessel, and are normalized to the average poloidal magnetic field measured at the same location.
It is worth noting that the system oscillates between two states, one where all modes have similar amplitudes (MH) and another one where the dominant mode and secondary ones are clearly distinguished (QSH).
More in detail, two magnetic topologies are distinguished in QSH states: the

Double Axis (DAx) and the *Single Helical Axis* (SHAx) states. DAx states are characterized by the presence of the resonant magnetic surface of the dominant mode torn into a magnetic island centered around a secondary magnetic axis (O-point), while the main magnetic axis is still present and in case shifted. Poloidally symmetric to the island O-point is an X-point, which is related to the island separatrix. Above a threshold of about 4% in the dominant mode normalized amplitude, the separatrix X-point merges with the main magnetic axis, and the two annihilate. Thus, the former island O-point becomes the only magnetic axis, i.e. the Single Helical Axis, and the helical plasma column is shaped by the dominant mode as shown in figure 2.7b. The DAx states are also known as *QSH with islands* [47].

In RFX-mod, the existence of different plasma states has been independently proved by different diagnostics. In particular, the figure 2.10 shows electron temperature radial profiles obtained by the Thomson scattering system (see section 3.1.3) in MH, DAx and SHAx states. As previously mentioned,

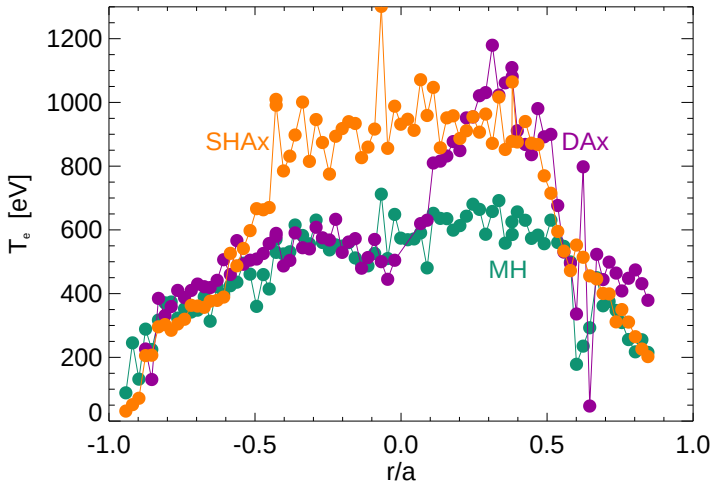

Figure 2.10: Electron temperature radial profiles in MH, DAx and SHAx states obtained by the Thomson scattering diagnostics.

the energy confinement properties of RFP plasmas in MH states are relatively poor, with only the outer plasma layer being able to sustain temperature gradients (green points). The occurrence of a magnetic island in DAx states gives rise to a thermal structure (violet points) over the nearly flat temperature level of the stochastic MH plasma core having a width of most 30% of the radius, always located off axis. Finally, the profiles in SHAx states (orange points) are

characterized by a temperature structure which is much larger than the DAx islands (more than 50% of the minor radius) extended to both sides of the geometric axis. This enlargement corresponds to an increase of the thermal energy content of the plasma.
The presence of strong gradients in the case of QSH states, indicates the formation of transport barriers that define a hot, bean-shaped region, centred off the geometric axis, on the resonant surface of the $(m, n) = (1, -7)$ mode.

2.2.3 The plasma edge

In the previous section (2.2.2), an introduction about the topological and thermal properties of the different states of the plasma equilibrium has been given. In the present one, some features regarding the edge plasma in the three regimes are highlighted. The edge has a great importance in particle and energy transport: fluctuations driving anomalous transport are often the main reason for the limited confinement.

As mentioned in Sec. 2.1, the safety factor profile of an RFP configuration

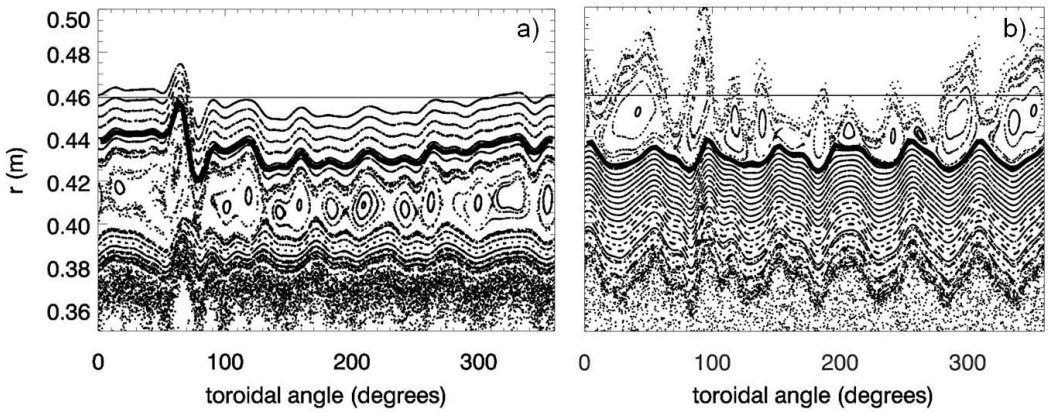

Figure 2.11: Poincaré plot of the magnetic field lines on the outer equator for a SHAx state at a deep reversal (a) and at shallow reversal (b). The thick line marks the position of the LCFS, while the horizontal one indicates the first wall position ($r/a = 1$).

is such that the $m = 0$ modes are resonant at the reversal, where a chain of poloidally symmetric islands is created. The radial position of the islands can be externally imposed by setting the value of the F parameter, defined in eq. 2.5.
In general, at more markedly negative F values ($F < -0.15$), the $m = 0$

islands close entirely into the chamber, so the the *Last Closed Flux Surface* (LCFS) is between them and the wall. On the other hand, for shallow F values ($F > -0.05$) the island field lines intercept the fist wall, so the LCFS in this case is radially located before the islands.
This can be observed in figure 2.11, where two *Poincaré plots* of the magnetic field lines in the $r - \varphi$ plane on the outer equator, realized at different F values, are shown. The first one has been obtained during a $1.5\,MA$ SHAx state at deep reversal ($F = -0.18$), while the second depicts a similar condition obtained at shallow reversal ($F = -0.02$). A thick line is superposed on each plot, depicting the position of the LCFS, computed from the field line tracing (FLiT) code outputs [48] by looking at where, for each toroidal and poloidal position, the most internal open field line is found. The new and striking result is that in the SHAx condition obtained at shallow reversal the LCFS is well separated from the wall by the $m = 0$ islands, and that their X-points act so as to form a divertor-like configuration. On the contrary, at deep reversal the LCFS is located beyond the $m = 0$ island chain and a limiter-like condition is obtained [49].

The topological characteristics of the external region in MH regime is quite complicated, with the large helical deformation due to phase and wall locking of both the $m = 0$ and $m = 1$ modes. On this topic, the development of the CMC algorithm (see Sec.2.2.1) and the consequent achievement of the QSH states drastically changed this picture. First of all, the locking of the modes is softened since the radial components of the secondary modes are much lower and the LCFS is interested by a uniform helical deformation, since the dominant helicity $(1, -7)$, imposes the same toroidal periodicity ($n = -7$) to the $m = 0$ pattern. This configuration is associated to a lower stress for the first wall because of a lower power deposition.
As result of the coupling of $m = 0$ and $m = 1$ modes, the external region presents a more regular behaviour, in which the field lines of the islands can eventually act as a kind of divertor for the inner confined plasma, if operating at shallow F values [49].

Furthermore, as mentioned in the previous section, the QSH states are characterized by a transient behaviour, that is related to the dynamo relaxation events that recurrently determine a temporary transition to the chaotic MH regime, destroying the precast magnetic order also at the edge.
The time evolution of the F signal, as shown in figure 2.12b, exhibits rapid changes, being a sort of rearrangement of the magnetic topology to a new MHD equilibrium state, through the reconnection of the magnetic field lines [50].

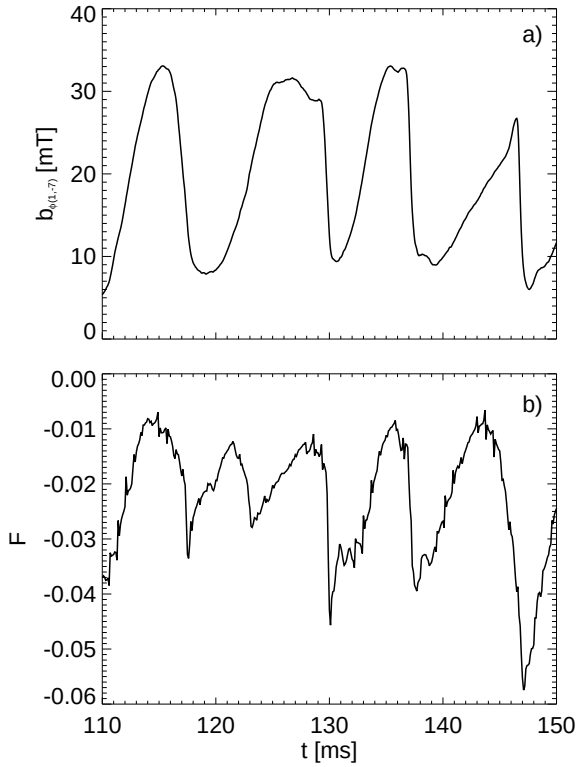

Figure 2.12: Time evolution of the dominant mode amplitude, $b_{\varphi(1,-7)}$, (a) and of the reversal parameter, F (b): when a DRE occur, the plasma has a transition from QSH to MH states.

These phenomena are known as the *Discrete Reconnection Events* (DRE). It is worth noting from fig. 2.12a that the amplitude of the dominant mode $b_{\varphi(1,-7)}$, index of the equilibrium state, falls down in coincidence with the occurrence of a DRE.

Finally, another feature of the plasma at the edge, is the presence of a radial electric field, E_r. Since the main component of the magnetic field in a RFP device is poloidal, the relative drift velocity

$$v_D = \frac{\mathbf{E} \times \mathbf{B}}{B^2} \tag{2.8}$$

is mostly toroidal. Moreover, since E_r is characterized by a sign inversion, v_D changes direction along the radial coordinate.

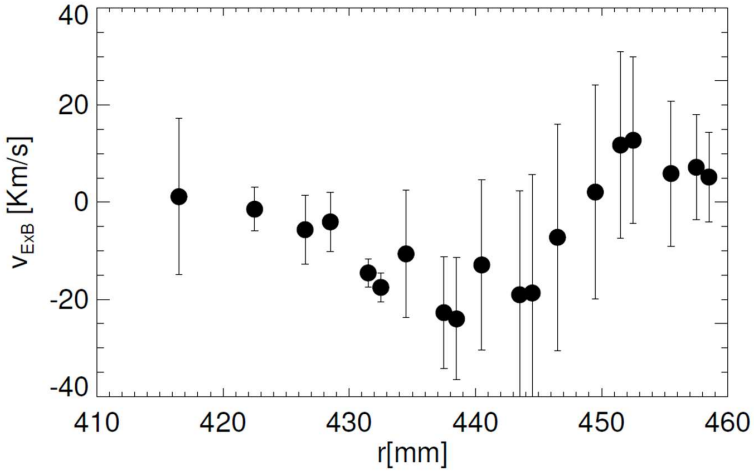

Figure 2.13: Radial profile of the $E \times B$ velocity evaluated by the electrostatic pins of the U-probe as an average of data from discharges with a shallow F value. The red line represents the chamber wall.

In figure 2.13, the v_D has been measured by means of the electrostatic pins of an insertable probe, the U-probe (more details in Sec. 3.1.1). Each symbol has been obtained averaging the data over the flat top phase of shallow F discharges. An inversion of the velocity direction is observed at $r/a \approx 0.98$.

2.3 EXTRAP T2R

The EXTRAP T2R device is a reversed-field pinch located at the Alfvén Laboratory in the Royal Institute of Technology, Stockholm (Sweden), in operation since 1994. A picture of the experiment is given in figure 2.14.

The EXTRAP T2R vacuum chamber is covered with a set of sensor coils and active coils that make it an optimal facility, along with RFX-mod, for the study of active feedback control. The main research area is the development of active feedback technique for the control of plasma instabilities using modern control theory tools [51] and the study of external magnetic perturbation effects on the plasma dynamics [52].

Resistive Wall Modes (RWM) and Edge-Localized Modes (ELM) are a problem for the success of the international experiment ITER and the development of techniques for their control is mandatory. RWM can be suppressed by developing feedback algorithms, such the intelligent shell. Among the techniques for ELM suppression, a promising candidate is the application of external magnetic perturbations resonant in the plasma (RMP). However, the ELM

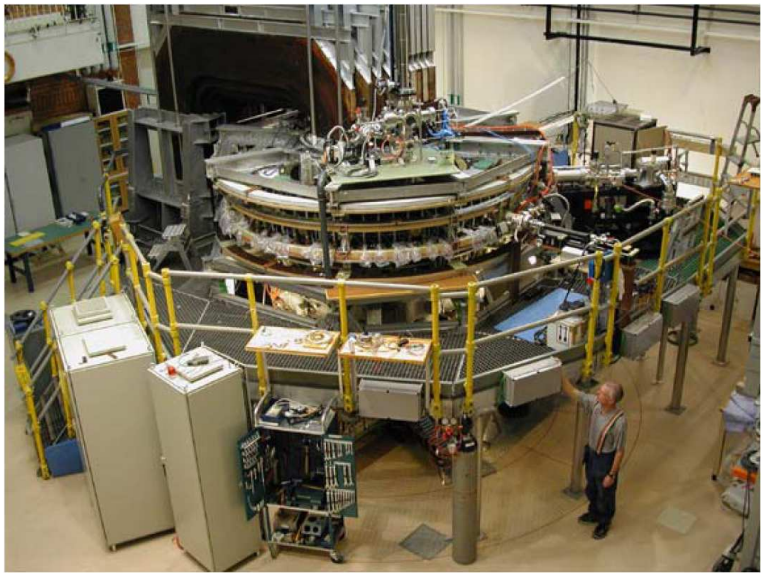

Figure 2.14: The EXTRAP T2R machine.

suppression mechanism via RMP and the external perturbation effect on the plasma are not yet fully understood. EXTRAP T2R with its feedback system gives a good opportunity for the study of the underlying physical mechanism that regulates the interaction between RMP and the plasma. Regarding the study of RWM control, that is a part of the European effort in the RWM area, the device expedites the study of these stationary instabilities, since they can be easily distinguished from the rotating tearing modes.
The dynamics of the rotating tearing modes is another important research area, since the RMP affect the TM dynamics and the plasma flow. In particular, RMP can induce oscillations in the TM amplitude, phase jumps and velocity reduction [53]. Finally, statistical studies of turbulence in the edge region of EXTRAP T2R are carried out in collaboration with the Consorzio RFX. In these contexts, the experimental campaigns performed during the last spring and reported in the Chapter 7 are included.

EXTRAP T2R is a medium-sized reversed field pinch device with high aspect ratio and an iron core. The main parameters of the experiment are summarized in table 2.2. Operation of EXTRAP T2R resumed in September 2000 after a major rebuilding [54], where the front-end system was completely replaced and equipped with a new resistive shell. Basic features of the new device are the following [54]:

- The torus shaped *vacuum vessel* is constituted of 15 sections of bellows,

Major radius	$= 1.24\ m$
Minor radius	$= 0.183\ m$
Plasma current	$\approx 70 \div 100\ kA$
Discharge duration	$\leq 100\ ms$
Plasma density range	$\approx 0.5 \div 1.5 \times 10^{19}\ m^{-3}$
Plasma volume	$\approx 1\ m^3$
Working gas	H

Table 2.2: Main parameters of EXTRAP T2R device.

joined by rigid flat sections supporting plasma limiters and port tubes for diagnostic and pumping access to the vessel. The material used is 316L stainless steel: EXTRAP T2R is one of few devices in the EU with an all metal first wall

- Array of *molybdenum limiters*, having the shape of convex disks, replaced graphite tiles for first wall protection (see fig. 2.15). There are a total of 180 limiters installed in the flat vessel sections.
- The thin, copper *double-layer shell*, with four times longer time constant than the single-layer thin shell used in the earlier configuration, reduces the magnetic field error at the poloidal gap. The new shell has a vertical field penetration time of $6.3\,ms$, to be compared to the $1.5\,ms$ of the previous EXTRAP T2.
- Solenoid type *toroidal field coil* minimizes field ripple compared to the helical coil used before. The axis of the toroidal field coil is displaced outward relative to the vacuum vessel in order to achieve the same field ripple on inboard and outboard sides.

In this configuration, RFP discharges are sustained for more than three shell times and a high density shot-to-shot reproducibility is achieved. Moreover, EXTRAP T2R plasma dynamics is in general dominated by the rotation [55] of the internally resonating tearing modes, since the field penetration time for the shell is long compared to the tearing mode relaxation cycle time scale but short compared to the pulse length. This is reflected in the low radial field amplitudes at the wall, which remains low until the end of the flat-top phase of the discharge, when the modes lock to the wall.

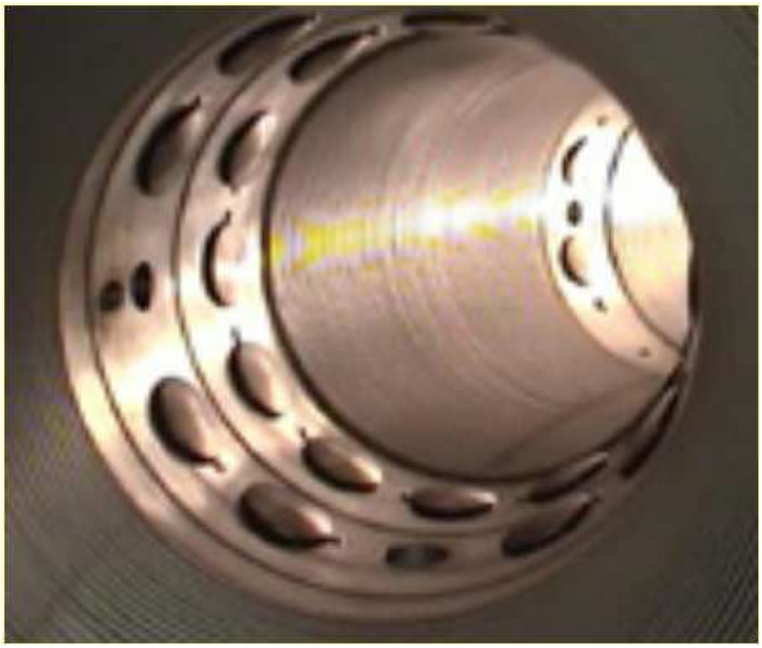

Figure 2.15: Vacuum vessel with Mo limiters in EXTRAP T2R device.

Diagnostics and data analysis

3.1 Diagnostics

The experimental results presented in this work have been achieved using different diagnostics. In particular, in both RFX-mod and EXTRAP T2R devices, the study of the high frequency coherent magnetic activities, which are the main topic of this thesis, has been performed using edge sensors measuring the time derivative of the magnetic fluctuations. The first two, installed in RFX-mod device, are:

- the insertable *U-probe* (Section 3.1.1) and
- the *Integrated System of Internal Sensors*, ISIS, (Section 3.1.2);

The third, located at the edge of EXTRAP T2R device, is

- the insertable *Alfvén probe* (Section 3.1.4).

They all are highly space- and time-resolved in-vessel systems: more details are in the following paragraphs. Some information about other RFX-mod diagnostics, mentioned in the thesis, are collected in paragraph 3.1.3.
Finally, the techniques used to analyze the data are presented in section 3.2.

3.1.1 U-probe

The analysis of magnetic fluctuations at the edge of RFX-mod plasma is extremely useful in order to investigate this complex region, characterized by a very fast dynamics and by the presence of strong gradients. The use of a probe that can measure inside the plasma gives important contributions on this topic.
An insertable probe, named *U-probe* for its shape (see picture 3.1), measuring electrostatic and magnetic fluctuations at the plasma edge is installed at RFX-mod device. The probe is made of two boron nitride cases, toroidally separated by $\Delta x = 88\,mm$.

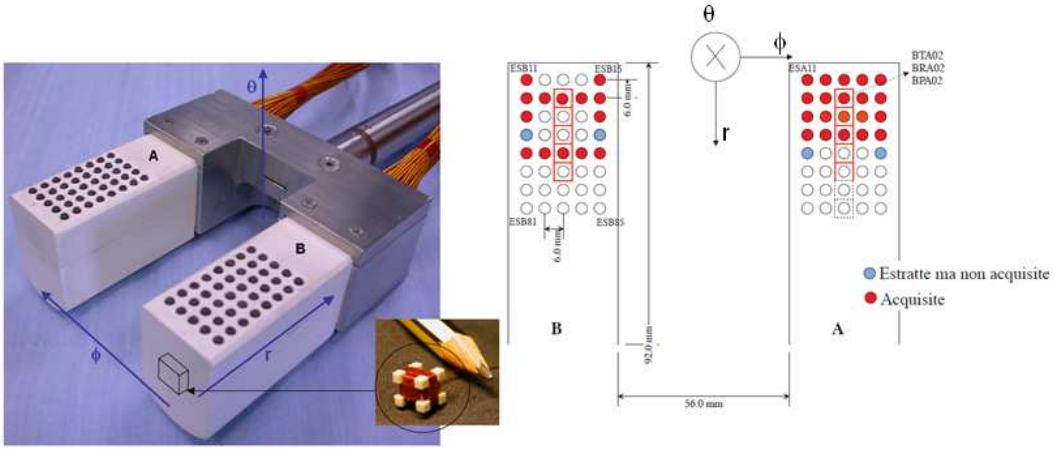

Figure 3.1: Schematic view of the U-probe and pictures of the total assembly and of a triaxial magnetic coil.

This diagnostic system is placed on the equatorial plane on the low field side of the machine ($\theta_{Up} = 0°$) and, toroidally, at $\varphi_{Up} = 217° 30'$, according to the RFX-mod notation.
The significant power loads delivered even during low plasma current discharges ($I_p \leq 500\,kA$) do not allow probe insertions deeper than the 10% of the minor radius. On the other hand, in higher plasma current discharges, the insertion of any solid object inside the plasma can be very dangerous, so the probe must be confined at the extreme edge of the vacuum chamber ($r/a \approx 1$). In this conditions, no remarkable perturbation of the plasma caused by the probe insertion has been observed.
As picture 3.1 shows, each case includes 2D arrays of electrostatic sensors (40 electrostatic pins, combined in eight 5-pins balanced triple probes), spaced by $6\,mm$. Together with the electrostatic pins, a radial array of 7 triaxial magnetic coils, $6\,mm$ radially spaced, are located in each case in order to measure the time derivative of the three components of the flutuating magnetic field.
As above mentioned, the probe can be inserted up to $\Delta r = 50\,mm$ inside the plasma. It can be useful to specify that the insertion Δr is measured from the head of the case to the level of the graphite tiles. The magnetic sensor closer to the plasma is $d = 13\,mm$ far from the head of the probe and the first electrostatic pin at $d = 7\,mm$; this means that to calculate their effective radial position (in mm) the follow relation must be used:

$$r_{coil} = a - \Delta r + d. \tag{3.1}$$

The electrostatic sensors have been extensively used in the last years in order to delineate electron density and temperature features at the edge [56].

Moreover, various results regarding the characterization of the toroidal plasma flow at the edge have been achieved [57, 58].
Nevertheless, since in this work, only the signals coming from the magnetic sensors are considered, these are presented in more detail.
In general, a simple way to measure the magnetic field fluctuations in the vicinity of a point in space is using a small coil. By means of the Faraday's law (1.6), it is easy to see that the voltage V_c induced on a coil endings by a uniform, time-varying magnetic field $B(t)$ is

$$V_c = \frac{d\Phi}{dt} = \dot{\mathbf{B}} \cdot \mathbf{A} \tag{3.2}$$

where A is the total area of the coil, given by $A = NA_1$, being N the number of turns of the wire and A_n the area of a single one [59].
As shown in the small central photo of picture 3.1, the magnetic sensor consists in a cubic structure less than $1\,cm$ large, thus the A_1 areas are enough small to consider the field crossing them as uniform. Three copper wires are wound around the support each in a different side. This configuration allows, since the V_c signals can be normalized for the respective area, to measure the time derivative of the three components of the magnetic field in almost the same position: radial $\dot{B}_r$, poloidal $\dot{B}_\theta$ and toroidal $\dot{B}_\phi$.
In most of the analysis presented in this thesis, it is possible to directly use the derivative signals, without integrating them in time, in order to avoid the introduction of numerical errors, without losing the physical meaning. Thus, unless otherwise indicated, the magnetic signals present in this work refer to the derivative ones. An example of typical U-probe time derivative magnetic signals is displayed in 3.2a.

The maximum sampling frequency is $10\,MHz$, with a bandwidth up to $3\,MHz$; nevertheless in various experimental campaigns this value had been reduced to $5\,MHz$, in order to collect less data without losing important physical information.
In figure 3.2b, the power spectra (see Sec. 3.2.1) relative to the mentioned signals are shown. The spectra show that the highest fluctuation levels occur in the $\dot{B}_r$ and $\dot{B}_\phi$ signals, which correspond to the perpendicular components at the edge of the RFP configuration, where the dominant magnetic field is the poloidal one.

Moreover, the presence of two coils toroidally spaced enables to measure the toroidal mode number n by means of the two-point tecnique, briefly illustrated in Sec. 3.2.3. It will be see that a system characterized by two sensors separated of an angle $\Delta\varphi$, permits to investigate toroidal numbers up to $\mid n \mid = \pi/\Delta\varphi \approx 87$.

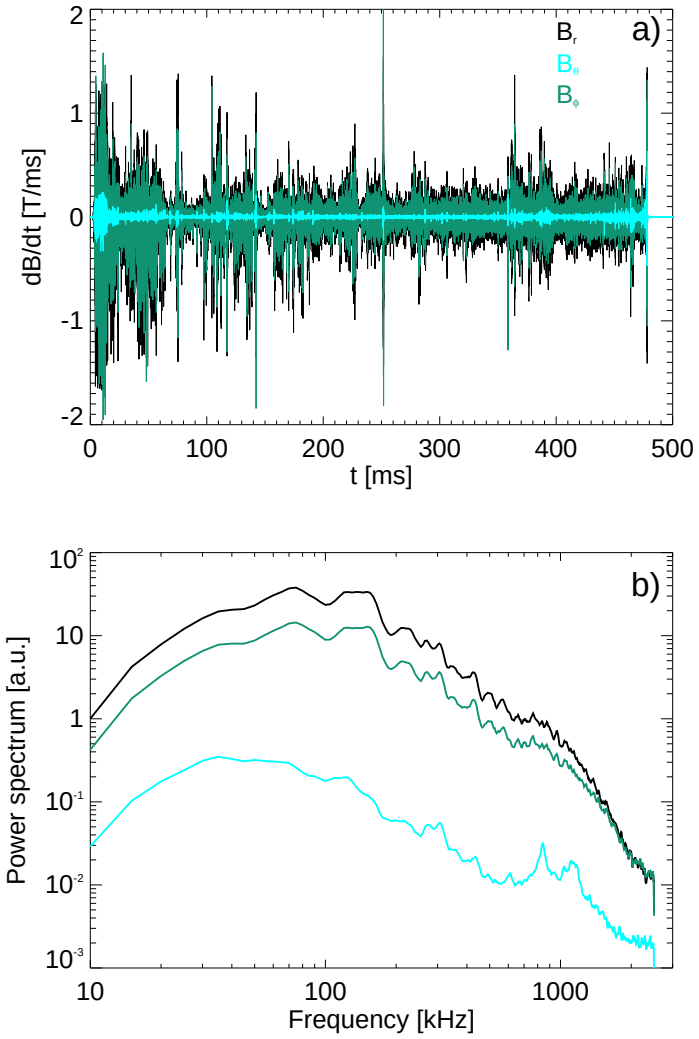

Figure 3.2: U-probe magnetic signals (a) and relative power spectra (b) of a typical RFX-mod discharge.

In the U-probe case, the angular distance of the two coils can be roughly approximated to $\Delta\varphi = \Delta x/(R+a)$, since the probe is located at the edge of the outer side of the machine. Moreover, some experimental campaigns with the probe turned of 90° has been performed: This allowed the measurement of the poloidal mode number m of the activities under investigation for some discharges. The maximum m that can be determined is $\mid m \mid = \pi a/\Delta x \approx 16$. A further consideration about the magnetic probes is that the measurement performed refers to an average value of plasma fluctuations localized in a radius

of some centimeters. So we probably can observe also magnetic perturbations that develop rather inside the plasma.

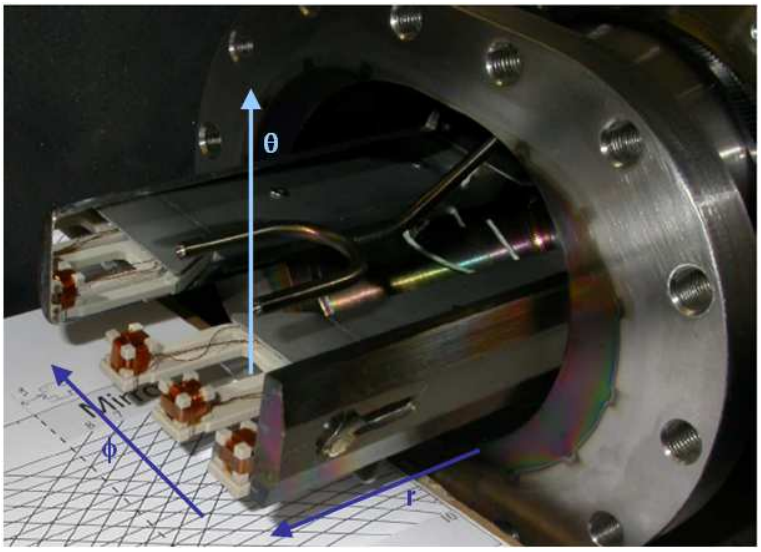

Figure 3.3: Picture of the "naked" triaxial magnetic coils installed on the GPI diagnostics.

GPI diagnostics coils.
Furthermore, a set of three magnetic coils, totally similar to those installed on the U-probe, have been placed on the Gas Puff Imaging (GPI) diagnostics. The GPI is an optical, non-intrusive diagnostics, measuring visible light emitted, generally, by the neutral atoms present in the plasma edge [60].
The toroidal position is $\phi_{GPI} = 322° 30'$ and the magnetic probes are nominally radially located at $r/a = 1$. The picture 3.3 shows the triaxial magnetic coils without the boron nitride cage that covers them as protection from heat and particle flux. They are recognized simply by enumeration: the order $1-2-3$ follow the conventional direction of the φ angle. The space between two close coils is $\Delta x = 22\,mm$, thus very high toroidal mode number values can be measured by this diagnostics: $\mid n \mid \approx 351$. The sampling frequency is $10\,MHz$.

3.1.2 ISIS

RFX-mod vacuum chamber is equipped with a large set of calorimetric, electrostatic and magnetic probes located inside the vacuum vessel, which constitute the Integrated System of Internal Sensors (ISIS) diagnostic. They are placed at $r/a \approx 1$, behind the graphite tiles which cover the first wall of the machine

and protect the sensors from the plasma. This system is mainly devoted to the acquisition of high frequency data and in order to provide a thorough description of fluctuating quantities in the RFX-mod edge plasma.

As above-mentioned, ISIS is composed of three subsystems:

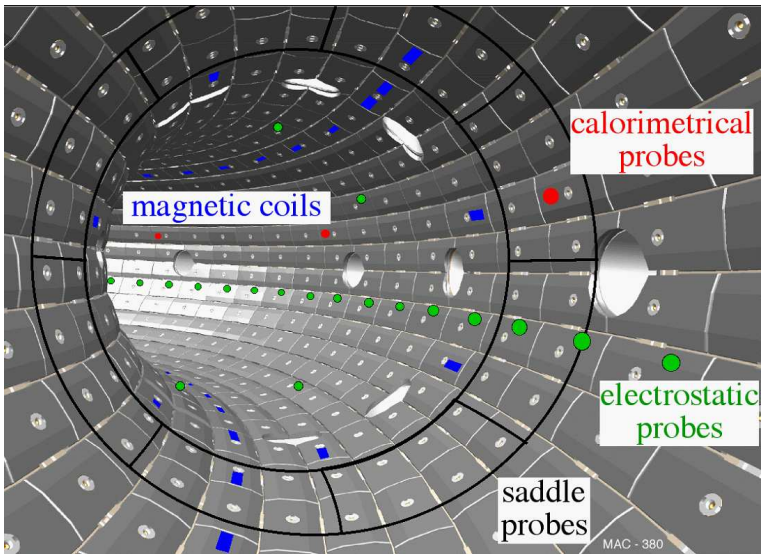

Figure 3.4: Schematic view of ISIS system: electrostatic and magnetic toroidal arrays and some calorimetric sensors are indicated.

- The **thermal probes** are thermocouples, measuring the average temperature of the whole tile, mounted on the back of some of the first wall graphite tiles. The system consists in one partial toroidal array of 8 probes, located at the poloidal angle $\theta = 6.5°$, on the outboard side, and adjacent to the pumping ports, which allow access to them. A description of the sensors is available in [61].

- The **electrostatic sensors** (Langmuir probes) are electrodes, measuring the *floating potential* V_f, that is the potential of an electrically insulated object immersed into the plasma. Some hints about the basic Langmuir probe theory are given in paragraph 3.1.4. The system is composed of a toroidal array of 72 pins equally spaced located at $\theta = 340.7°$, a poloidal array of 8 triple probes at $\phi = 248.6°$ and of additional single and triple probes. A description of the sensors is available in [62].

- The **magnetic sensors** are saddle and pick-up coils located on the back of the first wall graphite tiles: the nominal radial position of the measurements is $r/a = 1.03$.

Since, in this thesis, the analysis of RFX-mod plasma edge is limited to the study of the high frequency magnetic activities, only the magnetic sensors of the ISIS system are considered. As previously for the U-probe, all the signals investigated in the thesis represent the time derivatives of the magnetic fields. ISIS magnetic system consists in:

- two evenly spaced toroidal arrays, each made of 48 pick-up coils measuring the toroidal magnetic field $\dot{B}_\varphi$, located at the top ($\theta = 70.7°$) and the bottom ($\theta = 250.7°$) of the discharge chamber.

- a poloidal array of eight saddle probes measuring $\dot{B}_r$ and located at $\varphi = 210°$,

- a poloidal array of eight pick-up coils measuring $\dot{B}_\theta$ and located at $\varphi = 216.2°$,

- a poloidal array of eight pick-up coils measuring $\dot{B}_\varphi$ and located at $\varphi = 208.7°$,

- a partial poloidal array of six pick-up coils measuring $\dot{B}_\varphi$ and located at $\varphi = 28.9°$,

- a cluster of additional coils measuring $\dot{B}_\varphi$ and $\dot{B}_\theta$ in various poloidal and toroidal positions.

The sampling frequency is $2\,MHz$, while the estimated bandwidth of the measurement is up to $400\,kHz$. Magnetic pick-up probes are wound in two layers, for a total of 80 turns (see the picture 3.5). To obtain a reproducible and stable winding, special cables with a very thin and resistive sheath, made of Inconel 600 were realized and an appropriate elliptic shape was studied for the MACOR core [63].
In this thesis, one of the toroidal and the poloidal arrays measuring $\dot{B}_\varphi$ have been used for the analysis. The two arrays allow a resolution of the toroidal and poloidal mode numbers n and m up to 24 and 4, respectively due to the Nyquist theorem (the study of the mode numbers by means of an array of probes is summarized in 3.2.3).
Moreover, using two probes belonging to the cluster, toroidally spaced by $\Delta\varphi = 3.2°$, toroidal mode numbers up to $\mid n \mid \approx 56$ can be measured by means of the above-mentioned two-point technique.

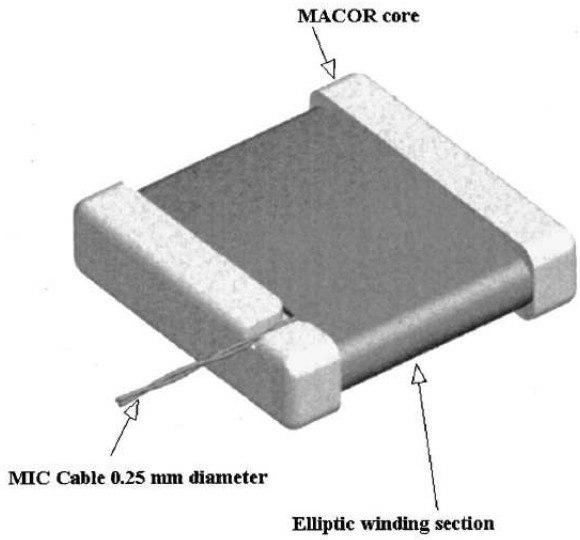

Figure 3.5: Three-dimensional model of the ISIS pick-up coils.

3.1.3 Other diagnostics and radial profiles reconstructions

Since electron temperature, density and safety factor profiles have been extensively used in the analyses presented in the following chapters, it is necessary to introduce the relative diagnostics to the reader. Moreover, some information about the pellet injectors and the neutral particle analyzer, that are mentioned in the following chapters, are given.

Electron temperature profile, $\mathbf{T_e(r)}$
RFX-mod is equipped since 2005 with a multi-point *Thomson scattering* system, designed to provide a single-shot highly spatially resolved radial profile of plasma electron temperature and, in principle, density simultaneously [64]. The laser beam passes through the plasma chamber along a diameter $-0.94 \leq r/a \leq 0.84$ in the equatorial plane. Scattered light is collected at approximately 90° from the incident beam through 3 windows where 84 pairs of optical fibers are located. The repetition rate is of about $25\,ms$, for a maximum number of 10 pulses in a discharge.
Recently some improvements in the Thomson diagnostics have been delivered. In particular, a better beam profile has been installed and the repetition rate is of $10\,ms$ for a maximum of 100 shots in a single discharge.

Electron density profile, $n_e(r)$

A *multi-chord infrared interferometer* measures the line-integrated electron density along 14 lines of sight placed on the same poloidal plane. The sampling frequency of the acquisition system is $1\,MHz$. The system is mounted at the toroidal angle $\phi_I = 22.5°$, on a granite structure C-shaped to be inserted between the magnetizing and the field shaping coils of the machine. The density is evaluated measuring the phase variation induced in a CO_2 laser beam ($\lambda = 10.6\,\mu m$) by passing through the plasma. The profile is thus reconstructed by numerical invertion of the interferometer data [65].

Safety factor profile, $q(r)$, $q(\rho)$
The safety factor profiles $q(r)$ are deduced by a suitable reconstruction of the equilibrium (e.g. [66]), that must match the external magnetic measurements, used as boundary conditions [67].
In the case of SHAx states, the equilibrium is modelled as a superposition of the zeroth-order axisymmetric equilibrium and of the dominant mode eigenfunction. In this geometry the safety factor is rescaled to the proper radial coordinate ρ, related to the helical flux, χ:

$$\rho = \sqrt{\frac{\chi - \chi_0}{\chi_a - \chi_0}}, \tag{3.3}$$

χ_0 being the helical flux on the helical axis and χ_a at the outermost surface [68]. The more evident different between the safety factor associated to the toroidal equilibrium, $q(r)$, and that associated to the helical one, $q(\rho)$, is the while the first is characterized by a monotonous decreasing profile (see fig. 2.2b), the second exhibits a maximum (see fig. 5.13) in correspondence to the steep internal temperature gradient characterizing the plasma during SHAx states.

Pellet injectors
A *room temperature pellet injector* [69] has been installed in RFX-mod with three aims: the first wall conditioning, impurity transport studies and the measurement of the pitch of the magnetic field lines. The injector uses pneumatically accelerated sabots to launch the pellets. Pellets of different sizes, speeds ($50 \div 200\,m/s$) and materials can be injected in the plasma; in particular, up to now, experiments with Litium and Carbon pellet injection have been performed.

Furthermore, a *cryogenic injector for H and D pellets* built at Riso National Laboratory is operating on RFX-mod [70]. The injector produces, by in-situ solidification, 8 pellets with masses of $1.5 \div 5 \times 10^{20}$ atoms and pneumatically accelerates them at velocities up to $1.5\,km/s$.

Neutral Particle Analyzer
A Neutral Particle Analyzer (NPA) of the ACORD series, developed by the IOFFE Institute of the Russian Academy of Sciences has been recently put in operation in the RFX-mod device. The NPA is equipped with a Nitrogen gas stripping cell and with 22 channeltron detectors (11 for Hydrogen, 11 for Deuterium) and by a magnetic deflection system to resolve the energy distribution of the neutral H^0 particles produced by charge exchange (CX) processes and leaving the plasma [71].

3.1.4 Alfvén probe

The study of the edge properties of EXTRAP T2R developed during my work at the Alfvén Laboratoriet and presented in chapter 7, has been performed by means of an integrated probe system, dubbed the *Alfvén probe*. This system consists in various electrostatic and magnetic probes, realized in order to study the Alfvénic nature of the edge plasma and the correlations between the $\mathbf{E} \times \mathbf{B}$ velocity field and the magnetic field.
All the signals are sampled at a frequency of $2\,MHz$, while the measured bandwidth is $1\,MHz$ for the magnetic coils and up to $700\,kHz$ for the Langmuir probes. The Alfvén probe is placed in the equatorial plane on the outboard side of the machine and it can be radially inserted up to $r/a = 0.92$. The insertion is strongly limited to the extreme edge when the electrostatic pins are set to collect ion saturation current, because the interaction between biased electrodes and streaming plasma, especially in low density discharges, can produce severe current arcs, potentially dangerous for the experimental equipment.

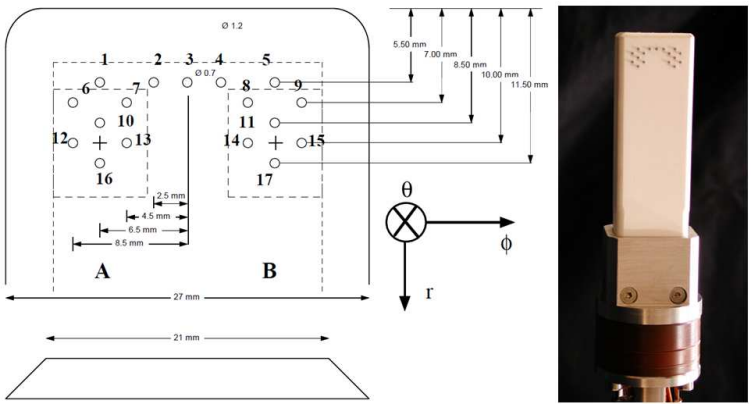

Figure 3.6: Schematic view and photo of the top of the Alfvén probe.

Electrostatic sensors

In figure 3.6, the scheme and a photo of the probe are shown.
On the top 17 pins are visible. In particular, the electrodes located in the inner row (the row closer to the plasma) are used as a combined triple Langmuir probe, allowing time resolved measurements of electron density, electron temperature and plasma potential, whereas all the other pins measure the floating potential in different positions.
In the following, a general description of Langmuir probe theory is given [72].
A characteristic feature of the plasma, as explained in paragraph 1.1, is its ability to screen out electrical charge, by the attraction of a cloud of particles of the opposite charge having the dimension of the Debye length, λ_D (eq. 1.1).
A solid surface in contact with the plasma will be in general hit by electron and ion fluxes, both drifting towards the probe with a velocity of the order of the ion sound velocity v_S [59].
It is easy to see that another way to write the 1.46 is

$$v_S = \sqrt{\frac{(T_i + T_e)}{m_i}} \tag{3.4}$$

Thus, on the one hand, it can be demonstrated that the ion saturation current density collected by the electrode is

$$j_{sat} = \zeta \, n_i \, v_S \, e \tag{3.5}$$

where the constant ζ is linked to the ratio between the ion density at the Debye sheath edge and in the background plasma, and it is usually approximated to 1/2 [73].
On the other hand, regarding to the electrons, since v_S is much smaller than the thermal one the electron distribution function is still close to a Maxwellian one. Their density can be written as:

$$n_e = n_0 \, exp[e(V - V_p)/T_e] \tag{3.6}$$

where n_0 is the density of the background plasma and V_p is the *plasma potential*.

In the case of a sensor electrically isolated, thus *floating*, the electrode will charge negatively relative to the plasma potential due to mass difference between ion and electrons, so further collection of electrons is retarded and ions are accelerated until the net current to the electrode is zero and electron and ion fluxes are equal. The main part of the charge difference between the solid and the plasma will be confined to a narrow sheath region restricted to some Debye lengths in thickness. It can be shown that V_p is related to the *floating potential* V_f, which is the potential adopted by a floating probe, by

$$V_p = V_f + \alpha \, T_e \tag{3.7}$$

The voltage dropped in the plasma sheath is consequently proportional to the electron temperature. The coefficient α can be calculated and varies generally between $2 \div 3$ depending on probe geometry, type of plasmas etc. [74].
When a bias voltage V_B applied on the probe is sufficiently negative with respect to the plasma potential, the probe collects only ion saturation current. Positive ions continue to be collected by the probe until the bias voltage reaches V_p, at which point ions begin to be repelled by the probe. On the contrary, for $V_B >> V_p$, all positive ions are repelled, and only the electron flux achieves the probe.

The estimate of floating and plasma potentials entails the measurement of various plasma parameters.
Different configurations of Langmuir probes exist, that can be distinguished in:

- **single probe**: from one single pin, with a sweeping bias and using for example the vacuum vessel as reference potential, can be extracted the electron temperature and density by means of the acquired current-voltage characteristic.

- **double probe**: a bias is applied between two equal probe tips so that all the system is floating. The collected current is proportional to the voltage difference between the two probes.

- **triple probe**: Temperature measurements using the single and double probe techniques requires a sweeping bias which limits the temporal resolution of these methods; in the triple probe, instead, a fixed bias is used. The triple probe uses a floating double probe biased to saturation, together with a single probe tip measuring the floating potential. The potential of the positive leg [75, 11] is

$$V_+ = V_f + ln(2)T_e \tag{3.8}$$

  A finer scheme is the so-called *five-pin balanced triple probe* [75], which has the advantage of reducing phase-shift problems between the signals. If this is the case, in the previous formula (3.8), $ln(3)$ instead of $ln(2)$ must be used.

Magnetic sensors

Two triaxial coils, very similar to those installed in the U-probe (section 3.1.1) measuring the time-derivative of the three components of magnetic field, are located into the Alfvén probe at the same radial and poloidal position and toroidally spaced of $\Delta x = 13\,mm$, so very high toroidal mode numbers can

be measured ($\mid n \mid \lesssim 335$). Their position is represented by the square dashed boxes in fig. 3.6.

3.2 Data analysis techniques

The purpose of this chapter is to briefly describe the basic fluctuation analysis techniques that have been applied to extract the results presented afterwards. These techniques are applicable to signals coming from sensors yielding local measurements, such as floating potentials obtained by Langmuir probes and magnetic field fluctuations measured by pick-up coils.
In particular, since physical theories and models are often formulated in terms of frequency rather than time, it is useful to transform the data from the *time domain* to the *frequency domain* e.g. to identify periodicities. This approach is known as *spectral analysis*. Single-point measurements yield information about the time behaviour of the fluctuations (e.g. power spectrum, spectrogram), but the minimum arrangement which can give an indication about their spatial structure is that of two measurement points (e.g $S(k, f)$ spectrum).

It can be here specified that spectrograms $S(t, f)$ and wavenumber-frequency spectra $S(k, f)$, being three-dimensional, are graphically represented by a colour-coded contour plot. Since the spectra amplitude is generally expressed in "arbitrary units", the absolute values are not indicated in the colour scale.

3.2.1 The power spectrum

It is known from mathematical analysis courses that, for a given function of time $x(t)$ defined in $-\infty \leq t \leq +\infty$, the continuous Fourier transform (CFT) is a function of frequency $X(f)$. CFT and its inverse are respectively defined by the relations

$$X(f) = \int_{-\infty}^{+\infty} x(t)\, e^{-\imath 2\pi f t} dt \qquad\qquad x(t) = \int_{-\infty}^{+\infty} X(f) e^{\imath 2\pi f t} df \tag{3.9}$$

A useful property regarding the CTF is an energy conservation law for the time and frequency domain representations of a signal, the *Parseval's theorem*, asserting that

$$\int_{-\infty}^{+\infty} \mid x(t) \mid^2 dt = 2 \int_{-\infty}^{+\infty} \mid X(f) \mid^2 df. \tag{3.10}$$

The interpretation of this theorem is that the total energy contained in a waveform $x(t)$ summed across all of time t is equal to the total energy of the waveform's Fourier Transform $X(f)$ summed across all of its frequency components f. (The coefficient 2 on the right side of the 3.10 is needed being positive and negative frequency indistinguishable.)
Nevertheless, in the practical case, experimental data are not continuous, but sampled, both in space and time, so that the definitions given in eq. 3.9 have to be revised. Thus, being $x_n = x(n\Delta t)$, with $n = 0, 1, ..., N-1$, a discrete and finite sequence of real numbers obtained sampling every Δt the continuous function $x(t)$ in the time range $T = N\Delta t$, the following definitions are given:

$$f_s = \frac{1}{\Delta t} \qquad \text{the sampling frequency} \tag{3.11}$$

$$f_N = \frac{1}{2\Delta t} \qquad \text{Nyquist frequency} \tag{3.12}$$

The f_N is the maximum frequency that can be achieved sampling every Δt. It ensues from the so-called **Nyquist sampling theorem**, which states that a function $x(t)$ such that $X(f) = 0$ for $\mid f \mid > f_N$ is completely determinated by its samples x_n. Thus, generally, the sampling time is chosen in such a way that the maximum frequency required to analyze a certain phenomenon is the Nyquist one.

If frequencies larger than f_N are present in the system, they would be seen

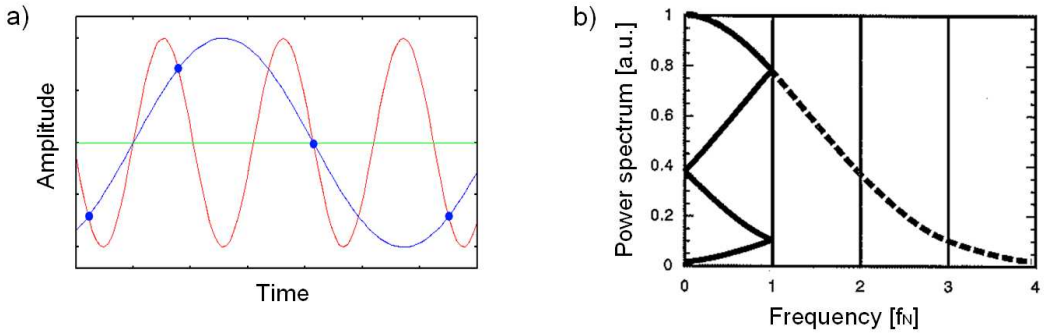

Figure 3.7: (a) The blue dots subsample the red signal, so they interpolate the blue wrong signal. (b) Power spectrum of a signal with frequencies $f > f_N$: they are shifted and/or folden back to within the frequency range $0 < f < f_N$.

in the digitized signal as a spurious frequency. A simple example is given in the figure 3.7a, where the red sine wave signal is sampled by the blue dots. Clearly they are not enough to reconstruct the original signal, so the blue signal results from their interpolation. It follows that any spectral component with frequency $f_N < f < 2f_N$ is "folden back" into the spectrum, appearing at a frequency $f_N - f$. The shifting of high frequencies so that they appear

below the Nyquist value, is the phenomenon known as *aliasing*. The mechanism can be understood by looking at figure 3.7b, where it is shown how the aliasing operates on the power spectrum at frequencies $f >> f_N$. The inverse process can be apply in order to correct the fraction of spectra clearly subject to aliasing, by shifting them at proper frequency values.
Obviously, spatial aliasing can also occur, as experimentally observed measuring high periodicity values in RFX-mod plasma.

Such kind of discrete signals can be described in the frequency domain by means of the so-called *Discrete Fourier Transform* (DFT). In particular, a sequence of N frequencies is defined, for which $f_n = n\Delta f$, where, in order to cover the whole frequency range allowed by the sampling theorem, it is chosen $\Delta f = 1/T$ (in this way $-f_N \leq f \leq f_N$). With this definitions, the first of the two relations 3.9 evaluated at f_n becomes:

$$X(f_n) = \int_{-\infty}^{+\infty} x(t) e^{-\imath 2\pi f_n t} dt \tag{3.13}$$

Since time is sampled, the integral is approximated to a discrete sum over the samples $t_j = j\Delta t$. Then, putting $X_n = X(f_n)\Delta f$, the discrete Fourier Transform and its inverse are defined:

$$X_n = \frac{1}{N} \sum_{j=0}^{N-1} x_j e^{-\imath 2\pi jn/N} \qquad\qquad x_j = \sum_{n=-N/2}^{N/2} X_n e^{\imath 2\pi jn/N} \tag{3.14}$$

However, the DFT is not generally calculated using the expression 3.14, since a more fast algorithm, the Fast Fourier Transform, proposed in 1965 by J.W. Cooley and J.W. Tukey, remarkably reduces the number of operations.
The *power spectrum* $S(f)$, in the discrete case, is the square of the magnitude of the DFT. Here "power" can mean the actual physical power, or more often, for convenience with abstract signals, can be defined as the squared value of the signal.

The signal $x(t)$ can be treated as a stationary random process, whose *autocorrelation function* $R(\tau)$ is defined as

$$R(\tau) = E[x(t)x(t-\tau)] \tag{3.15}$$

being $E[...]$ the expected value, that is the average over the probability distribution function. It quantifies how well correlated are couples of values of $x(t)$ having a time distance of lag τ.

Thus, the power spectrum is the Fourier transform of the auto-correlation function:

$$S(f) = \int_{-\infty}^{+\infty} R(\tau)\, e^{-\imath 2\pi f \tau} d\tau \text{ , thus } R(\tau) = \int_{-\infty}^{+\infty} S(f)\, e^{\imath 2\pi f \tau} df \tag{3.16}$$

It is worth noting that in the case $\tau = 0$,

$$E[\mid x(t) \mid^2] = \int_{-\infty}^{+\infty} S(f) df \tag{3.17}$$

which means that $S(f)$ describes how the mean square value of $x(t)$ is distributed over frequencies.
Typically, the problem of estimating the expected value is effectively overcome by ensemble averaging over M sample spectra. The approach used is to divide the signal under analysis in M slices $x_T^{(k)}(t)$, each of lenght T, and treating each slice as indipendent realization of the process under study. In the continuous case, $S(f)$ can be estimated using

$$\hat{S(f)} = \frac{1}{M} \sum_{k=1}^{M} S^{(k)}(f) \quad \text{where} \quad S^{(k)}(f) = \frac{1}{T} \mid X_T^{(k)}(f) \mid^2 . \tag{3.18}$$

In the discrete case, the power spectrum estimator is

$$\hat{S}_n = \frac{1}{M} \sum_{k=1}^{M} \mid X_n^{(k)} \mid^2, \tag{3.19}$$

where $X_n^{(k)}$ is the n-th element of the DFT of slice k. Thus, it is possible to demonstrate that the discrete analogous of eq. 3.17 is

$$\frac{1}{N} \sum_{j=0}^{N-1} \mid x_j \mid^2 \simeq \sum_{n=0}^{N-1} S_n \tag{3.20}$$

To reduce leakage, each slice is multiplied by the Hanning window [76]. The relation 3.20 is then finally computed.

3.2.2 Spectrogram

A spectrogram is a time-varying spectral representation, that shows how the spectral density of a signal varies with time, $S(t, f)$. The most common format is a colour-code contour plot whose horizontal axis represents the time t, the

vertical axis the frequency f and a third dimension referring to the amplitude of a particular frequency at a particular time is indicated by a colour scale for each point in the image.
Spectrograms are usually calculated from the time signal using the short-time Fourier transform (STFT). Creating a spectrogram using the STFT is usually a digital process, where the signal is broken up into chunks associated to the time τ, which usually overlap, and Fourier transformed to calculate the magnitude of the frequency spectrum for each chunk. In the continuous-time case, the signal to be transformed is multiplied by a window function $w(t)$ which is nonzero for only a short period of time. Thus, the spectrogram of a signal $x(t)$ can be estimated by computing the squared magnitude of the STFT of the signal, as the window moved along the time axis, as follows:

$$S(\tau, f) = |\mathrm{STFT}(\tau, f)|^2 = \int_{-\infty}^{+\infty} x(t)w(t-\tau)e^{-\imath 2\pi f t}dt \tag{3.21}$$

Each chunk corresponds to a vertical line in the image, that carries a measurement of power spectrum versus frequency for a specific moment in time. The frequency spectra are finally "laid side by side" to form the image.

3.2.3 Wavenumber-frequency spectrum

The analysis of the signals coming from different measurement points, can provide some information about the spatial structure along the direction connecting the points. In particular, a wavenumber-frequency power spectrum can give a presention of the dispersion relation of the fluctuating activity under study, easy to read. Moreover, since frequency and wavenumber spectral indices are found independently, both frequency-integrated wavenumber spectrum $S(n)$ and wavenumber-integrated frequency spectrum $S(f)$, that is analogous to the power spectrum derived in sec. 3.2.1 but for selected wavenumber values, can be computed.

One method for the calculation of the $S(k, f)$ spectrum has been developed by Beall [77] and it is known as the *two-point technique*, since it uses fixed probe pairs. An alternative method is the spatial Fourier decomposition of probes equally distributed along a circular (or periodic) array.

Two-point technique
We introduce the concept of the local wavenumber and frequency spectral density, which can be estimated using spatially fixed, point data sources ("fixed probe pairs"), and discuss the relationship of this spectral density to the conventional wavenumber and frequency spectral density and the cross-power

spectral density. The local wavenumber and frequency spectral density is shown to be equivalent to the conventional wavenumber and frequency spectral density when the fluctuation is stationary and homogeneous and consists of a superposition of wave packets; such a fluctuation is the basic model used in many turbulence theories. A digital method for estimating the local wavenumber spectrum is described and applied, in the context of this thesis, to the magnetic signals coming from the coils of the U-probe, GPI diagnostics and Alfvén probe and furthermore from two ISIS magnetic sensors belonging to the cluster of probes.
Since the relevant information is the phase difference between the two signals, in order to extract a physically relevant measurement, the points must be close enough to give correlated measurements, but distant enough to yield a measurable phase difference.

The *cross-correlation function* of two signals $x(t)$ and $y(t)$ is defined, in analogy to the auto-correlation function 3.15, as

$$R_{yx}(\tau) = E[y(t)x(t-\tau)]. \tag{3.22}$$

It is related to the *cross-covariance function*

$$C_{yx}(\tau) = E[(y(t) - m_y)(x(t-\tau) - m_x)] \tag{3.23}$$

by $C_{yx}(\tau) = R_{yx}(\tau) - m_y m_x$, with $m_y = E[y(t)]$ and $m_x = E[x(t)]$.
In analogy with the power spectrum of one signal (Sec. 3.2.1), the *cross-power spectrum* (CPS) of two signals is defined as the Fourier transform of their cross-correlation function. CPS and its inverse are respectively

$$S_{YX}(f) = \int_{-\infty}^{+\infty} R_{yx}(\tau)\, e^{-\imath 2\pi f\tau} d\tau \;\text{ and }\; R_{yx}(\tau) = \int_{-\infty}^{+\infty} S_{YX}(f)\, e^{\imath 2\pi f\tau} df. \tag{3.24}$$

But contrary to the power spectrum, the CPS is complex-valued:

$$S_{YX}(f) = C_{YX}(f) + \imath Q_{YX}(f), \tag{3.25}$$

where $C_{YX}(f)$ is known as the *co-spectrum* and $Q_{YX}(f)$ as the *quad-spectrum*. Using a polar representation,

$$S_{YX}(f) = \mid S_{YX}(f) \mid e^{\imath\Theta_{YX}(f)}. \tag{3.26}$$

From the 3.26, two very important quantities are defined. On the one hand, $\Theta_{YX}(f)$, called the *phase spectrum*, gives the average phase difference of the Fourier components of the two signals, frequency by frequency. On the other

hand, the amplitude $\mid S_{YX}(f) \mid$ of the CPS is generally expressed in the normalized form

$$\gamma_{YX}(f) = \frac{\mid S_{YX}(f) \mid}{\sqrt{S_Y(f) S_X(f)}} \tag{3.27}$$

where $S_Y(f)$ and $S_X(f)$ are the power spectra of the two signals. $\gamma_{YX}(f)$ is called *coherence spectrum* (or simply *coherence*) and gives the degree of linear correlation of the signals frequency by frequency. A very important point to keep in mind is that the phase spectrum is significant only at frequencies where the coherence is not too low when the coherence is almost zero the two signals are uncorrelated at that given frequency, so that their phase difference is random.
The practical evaluation of the CPS proceeds along the same lines as the power spectrum: the two signals are divided into M slices, multiplied by the Hanning window and Fourier transformed. So, analogously to eq. 3.19, the cross-power estimator to be computed is

$$\hat{S}_{YX,n} = \frac{1}{M} \sum_{k=1}^{M} Y_n^{(k)} X_n^{*(k)}. \tag{3.28}$$

In order to determine the wavenumber $k(f)$ as a function of the frequency, it is useful to distinguish the case of measured phenomena characterized by a deterministic dispersion relations rather than by turbulently broadband ones. In the first case,the fluctuating quantity $g(x,t)$ can be represented as a superposition of plane waves. Each component, in travelling from one sensor (1) of the probe to the other (2) located at a distance Δx, undergoes a phase shift, so that

$$\hat{k}(f) = \frac{\hat{\Theta}_{12}}{\Delta x}. \tag{3.29}$$

In the general case of turbulent phenomena, a well defined relationship between frequency and wavenumber does not exist. One should therefore aim at computing a spectral density function giving the power present in the fluctuatting field for each couple of frequency and wavenumber values. For continuous space and time and considering the field $g(x,t)$ stationary and homogeneous, its *space-time correlation function*

$$R(\chi, \tau) = E[g(x,t) g(x-\chi, t-\tau)] \tag{3.30}$$

depends only on time and space lags. The space-time CFT of $g(x,t)$ and its inverse, in terms of k and of the angular frequency $\omega = 2\pi f$, are defined as

$$\begin{aligned} G(k,\omega) &= \iint_{-\infty}^{+\infty} g(x,t)\, e^{-\imath(\omega t - kx)} dx dt \quad \text{and} \\ g(x,t) &= \tfrac{1}{(2\pi)^2} \iint_{-\infty}^{+\infty} G(\omega,k)\, e^{\imath(\omega t - kx)} dk d\omega. \end{aligned} \tag{3.31}$$

The wavenumber-frequency spectrum is the extension to space-time of the power-spectrum. Thus, the CFT of the space-time correlation function 3.30 and its inverse are

$$S(k,\omega) = \iint_{-\infty}^{+\infty} R(\chi,\tau)\, e^{-\imath(\omega\tau - kx)} d\chi d\tau \quad \text{and}$$
$$R(\chi,\tau) = \iint_{-\infty}^{+\infty} S_(k,\omega)\, e^{\imath(\omega\tau - kx)} dk d\omega. \tag{3.32}$$

It can be demonstrated that, for lenght (L) and time (T) scales large enough, an appropriate estimator for the wavenumber-frequency spectrum is

$$\hat{S}(k,\omega) = \frac{1}{LT} E[G_{LT}(k,\omega) G^*_{LT}(k,\omega)] \tag{3.33}$$

Therefore, in the case that only two measurement points are available, the *two-point estimate* of the wavenumber-frequency spectrum uses the phase difference between the two signals as an estimate of the wavenumber at each frequency. In particular, after the usual division of the signals $x_T(t)$ and $y_T(t)$ into M slices, required for the computation of the ensemble average, the DFT of the slices are used to built an histogram representing the $S(k,f)$: for each j-th slice, a local wavenumber is computed as

$$k_n^{(j)} = \frac{arg(Y_n^{*(j)} X_n^{(j)})}{\Delta x} \tag{3.34}$$

(n is the index running over the frequencies). The 2D-histogram of $S(k,f)$ is then incremented at the locations by a quantity equal to

$$S_n^{(j)} = \mid Y_n^{*(j)} X_n^{(j)} \mid \tag{3.35}$$

that is the power at frequency n and wavenumber $k_n^{(j)}$. This is repeated for all the slices and the resulting histogram is divided by M.
Keeping in mind the Nyquist theorem, it can be seen that the maximum wavenumber that can be detected is $\pi/\Delta x$. If larger values are present in the system under study, they will give rise to aliasing. Moreover, the probe spacing must be large enough so that the phase difference corresponding to the wavenumber resolution that we want to obtain is large enough to be detected, but, in case of turbulent phenomena, it must be smaller than a coherence length, since, otherwise, the phase errors would be quite large in a low coherence situation.

Circular array
The previous discussion can be now extended to the case of several spatial

points. In particular, it can be taken into account the situation where M measurement points are available and equally spaced in a circular array. Actually, the assumption here is that we are measuring the properties of our system around a symmetry axis. Thus, it is possible to estimate the wavenumber-frequency spectrum without the statistical approach used in the two-point technique, but rather by using a discrete version of the estimator derived in equation 3.33. Due to the fact that we are considering a set of probes arranged in a periodic fashion, the Fourier transform in space (at different θ angles) is really a determination of the coefficients of a Fourier series. In practice, amplitudes and phases are computed by applying the FFT algorithm to the M measurements at each time sample. The amplitudes $a_m(t)$ and the phases $\alpha_m(t)$ are related to the measured field $x(t)$ by

$$x(\theta, t) = \sum_{m=0,1...} a_m(t) \cos[m\theta + \alpha_m(t)] \tag{3.36}$$

Furthermore, the frequency-wavenumber power spectrum is computed as

$$S(m, f) = \lim_{T\to\infty} \frac{1}{T} \langle \mid X_T(m, f) \mid^2 \rangle \tag{3.37}$$

where the angular brackets represent an ensemble average computed as an average over the time slices in which the signals have been divided, whereas $X_T(m, f)$ is the double Fourier transform of the array of signals $x(\theta, t)$, recorded for a time T, over both time and angle.
The maximum wavenumber value that can be measured by a circular array is estimated by means of the Nyquist theorem: $\mid k \mid = M/(2R)$, where R is the radius of the array.

Resistive Interchange Modes in RFX-mod

In this chapter, the first direct experimental evidence of magnetic fluctuations due to unstable *resistive interchange modes* in RFX-mod plasma is presented. After an introduction about the features of these modes in fusion and, in particular, in RFP plasmas (Sec. 4.1), the experimental observations performed by means of a sophisticated setting of in-vessel detectors, are described. The instabilities detected are characterized by relatively high frequency, high toroidal mode number ($n > 20$) and they resonate in the edge region of RFX-mod plasma (Sec. 4.2). A comparison with modelling prediction has also been exposed in Sec. 4.3.

4.1 Resistive Interchange Modes theory

As exposed in the introductive section dedicated to *Interchange modes* (1.4.1), a plasma in a curved magnetic field can exhibit the unstable growth of interchange perturbations when the radius of curvature vector is directed oppositely to the direction of the pressure gradient. This can occur whenever a plasma is confined in a magnetic field that is concave towards the plasma itself.
In a tokamak configuration, the main magnetic field is toroidal. Thus, as highlighted in fig. 4.1a, the toroidal curvature is *favourable* (convex towards the plasma) on the inner side of the machine (small R_c) and *unfavourable* (concave towards the plasma) on the outer side (large R_c). This means that the modes could appear in the outer side region of the plasma. Anyway, the $1/R$ weight of the small R-side is slightly greater than the weight of the large R-side, so the net effect is stabilizing. Regarding to a RFP configuration, since the main magnetic field is poloidal, the situation is different: as shown in picture 4.1b, only regions of unfavourable curvature are present.

Nevertheless, the magnetic field has two stabilizing roles: on the one hand, any bending of the field lines tends to oppose to the growth of the perturba-

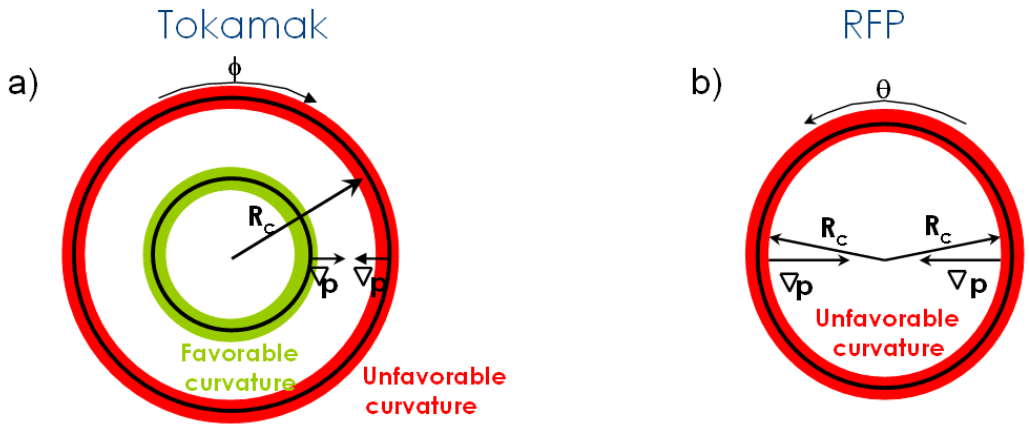

Figure 4.1: a) In a tokamak configuration the curvature of the main magnetic field is favourable on the inner side and unfavourable on the outer side. b) In a RFP configuration the curvature is always unfavourable.

tion with wavelengths below a certain critical value; on the other, the magnetic shear s (defined in eq. 1.21) limits the region of instability when this occurs. The presence of a *shear* of the magnetic field lines activates a mechanism that inhibits the charge separation which would otherwise build up. Since a field line traced many times around the torus maps out a flux surface, charges are rapidly dispersed, being transported along the field lines. This is known as *shear stabilization*.
The first linear stability analysis on this topic was presented by Bergen R. Suydam in 1958 [78] for a linear pinch (with B_z being the axial magnetic field). The theory provides a necessary condition for the $m \neq 0$ modes to be stable:

$$\frac{dp}{dr} + \frac{rB_z^2}{8\mu_0}\left(\frac{1}{q}\frac{dq}{dr}\right)^2 > 0 \tag{4.1}$$

where q is the safety factor (see definition 1.20). This relation is called *Suydam's criterion*, which asserts that to stabilize interchange modes the magnetic shear must be large enough to overcome the destabilizing effect of the pressure gradient, i.e. $dp/dr < 0$. Two years later, in 1960, Claude Mercier generalized the stabilization criterion for a toroidal plasma [79]. Then further, more complete formulations followed (e.g. [80]).
The unique regions where the shear stabilization cannot operate are the rational surfaces (defined in 1.4), because there the field lines close upon themselves and do not outline a flux surface, so charge build up is not inhibited. If a perturbation, having the same field line pitch of a rational surface, occurs,

interchange instabilities can locally grow.
Thus, the interchange modes tend to be localized around resonant surfaces, where a small displacement of magnetic field lines is possible without distortion of the lines themselves, so as to minimize the magnetic field line bending energy. The driving force for these modes is the pressure gradient across surfaces with average unfavourable curvature.

In real plasmas, resistivity must be taken into account. Indeed, the presence of finite resistivity favours the destabilization of the modes at pressure gradient values lower than those predicted by ideal MHD theory [81]. The relation between the growth rates and the Lundquist number, that is inversely proportional to the resistivity, is known to scale as $\sim S^{-1/3}$. This point is one of the features that can help to distinguish between interchange and tearing modes, the last being the most common resonant modes in fusion devices. The tearing modes growth rate, indeed, scales with $\sim S^{-3/5}$ [82, 20].

Moreover, resistivity gradients have been demonstrated to drive a different kind of modes, named *rippling modes*, having features very similar to those of the pressure-gradient-driven interchange (they are resonant, localized at the edge, they interchange internal to external plasma regions in a fusion device), so to become almost indistinguishable in our case. Anyway, the contributions of pressure and resistivity gradients are summed [20], thus, in general, a cumulative effect can occur. But, since the possible presence of the mentioned rippling mode cannot be verified, we will not take into account the previous considerations in the following analysis.

4.2 Experimental observations

The study of the modes, interpreted as belonging to the interchange branch, starts from the analysis of the magnetic spectra measured by the insertable U-probe, presented in Sec. 3.1.1. The space-time properties of the magnetic fluctuations have been obtained by Fourier transforming the signals obtained from the complete toroidal array of coils measuring B_φ of the ISIS system (Sec. 3.1.2).
The whole analysis covers a set of 200 discharges, performed in a relatively low plasma current range ($300\,kA < I_p < 600\,kA$). This selection is due, on the one hand, to the fact that the U-probe cannot be inserted inside the plasma during high current discharges and, on the other hand, because the magnetic

spectra measured at high I_p levels by the ISIS system are affected by the presence of various coherent fluctuations, thus an analysis that can distinguish the contributions from different modes would be more complex.
The spectra in fig. 4.2 show that large magnetic fluctuations are present for frequencies up to about $200\,kHz$, with about 60% of the total magnetic fluctuating energy concentrated in the frequency region spanning from 30 to $150\,kHz$.
In particular, it is observed that the magnetic spectrum peaks around $100\,kHz$

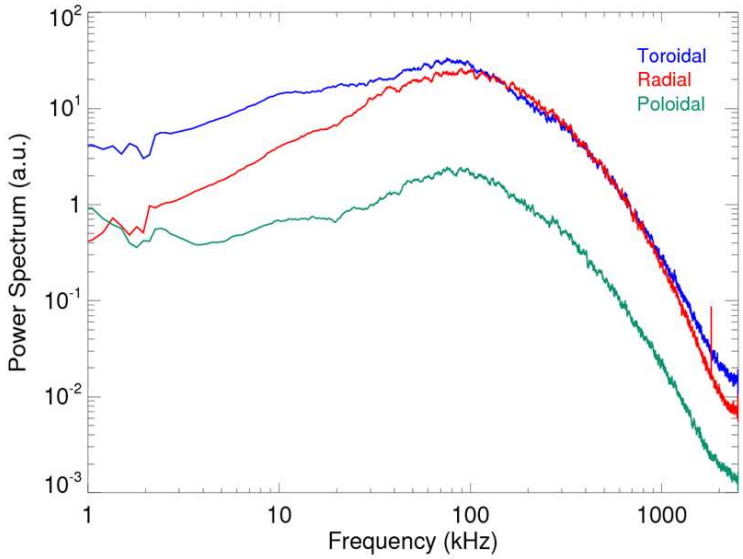

Figure 4.2: Typical power spectra of the time derivative of the three components of the magnetic field, measured by the U-probe

during the discharges characterized by a deep reversal of the toroidal magnetic field. In this context, "deep reversal" means values of the parameter $F < -0.1$ or, analogously, values of the safety factor profile at the edge $q(a) < -0.025$. Although in the RFP configuration the parameter F is usually adopted to represent the reversal depth, in this thesis I prefer to use the more common $q(a)$.
Two $S(n, f)$ spectra, obtained as a conditional average over discharges selected at two different $q(a)$ values, are shown in figure 4.3. Magnetic activities exhibiting different characteristics (frequency, periodicities, dispersion relations) are found in the two different equilibria.

Shallow reversal.
Figure 4.3a shows the $S(n, f)$ spectrum obtained as an average over discharges characterized by a shallow reversal of the toroidal magnetic field, corresponding to $q(a) = -0.015$. A coherent structure is observed at frequencies below

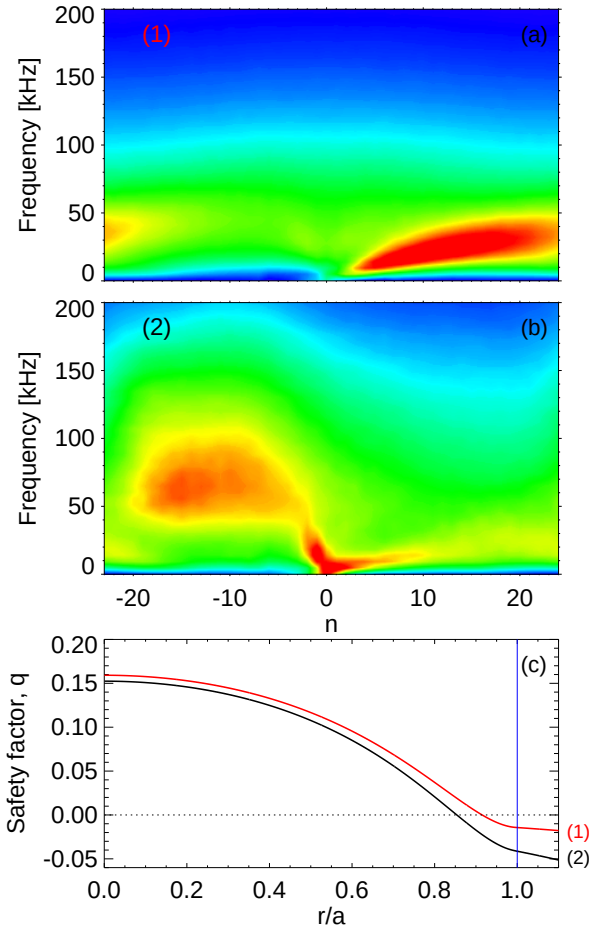

Figure 4.3: Typical colour-coded contour plot of the $S(n, f)$ spectra of magnetic fluctuations for two different experimental conditions: (a) $S(n, f)$ spectrum obtained at shallow reversal of the magnetic field, $q(a) = -0.015$; (b) $S(n, f)$ spectrum obtained at deeper reversal, $q(a) = -0.050$; (c) the two reference $q(r)$ profiles. The vertical line marks the plasma wall.

$50\,kHz$ arranged on an almost continuous linear dispersion relation, in the form $\omega = (n/R)v_{ph}$, with $\omega = 2\pi f$, where f is the frequency and v_{ph} is the phase velocity of the fluctuations in the toroidal direction. The measured phase velocity is of the order of $20 \div 30\,kms^{-1}$ in the counter toroidal plasma current direction corresponding to the electron diamagnetic direction, which is

in good agreement with the plasma flow velocity at the edge of the RFX-mod device deduced by means of gas puffing imaging diagnostics [83] and is also consistent with the $\mathbf{E} \times \mathbf{B}$ flow measured by the Langmuir probes [84].
The analysis of the poloidal periodicity, performed by means of the poloidal array of ISIS sensors, reveals the main $m = 0$ nature of this magnetic fluctuation, whose origin is still under investigation. Thus, **in shallow reversal discharges, a $m = 0$ activity, that is probably associated to the global flow propagation, is measured**. More information on this topic is provided in Sec. 4.2.2.

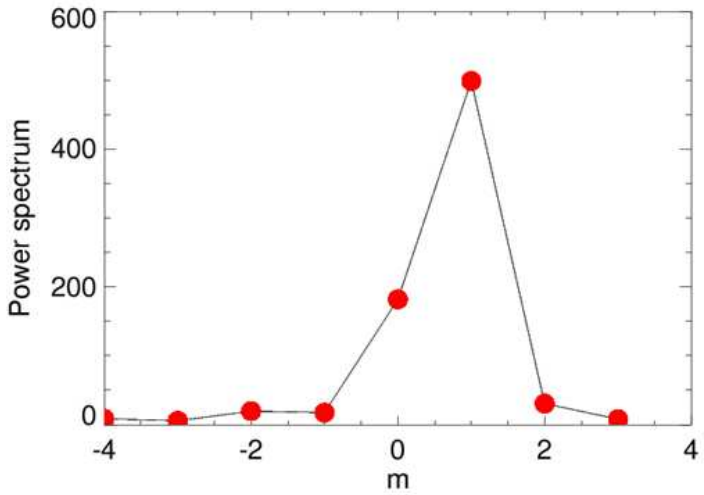

Figure 4.4: $S(m, f)$ spectrum from the ISIS poloidal array measuring $\dot{B}_\varphi$ obtained selecting in frequency the magnetic activity observed at deep reversal discharges: the poloidal mode number measured is $m = 1$.

Deep reversal.
The $m = 0$ fluctuations are observed to become of smaller amplitude in deeply reversal discharges, as can be seen in figure 4.3b, obtained by analyzing data taken selecting the discharges with $q(a) \approx -0.050$. In this $S(n, f)$ spectrum, a different coherent structure at frequencies in the range $40 \div 100\,kHz$, is observed to dominate. The Fourier decomposition of the signals from the ISIS poloidal array of probes shows that its dominant periodicity is $m = 1$. This result is exhibited by the curve in picture 4.4, obtained by integrating the $S(m, f)$ spectrum provided by the ISIS array over the frequency range spanned by the modes under investigation.
In particular, the mentioned $S(n, f)$ spectrum (fig. 4.3b) exhibits the excitation of magnetic fluctuations in the form of a broad peak at high ($n \approx 35$) posi-

tive toroidal mode numbers (the modes resonate outside the reversal surface, Sec. 3.2.3). This value of the toroidal mode number results from a correction

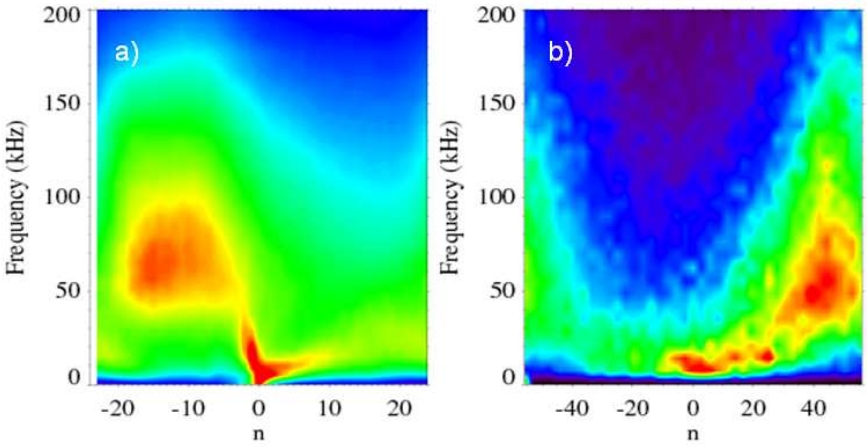

Figure 4.5: (a) $S(n, f)$ spectrum obtained by means of the toroidal array of ISIS coils, measuring n up to 24. (b) $S(n, f)$ spectrum obtained by means of two closely toroidally spaced array ISIS coils, measuring n up to 56.

of the periodicity scale, that is necessary since the spatial resolution of the toroidal array of ISIS coils is limited ($\mid n \mid \leq 24$) and so the computed $S(n, f)$ spectra are affected by aliasing. As mentioned in 3.2.1, in some cases it is possible to correct spectra affected by aliasing by means of a proper shift. In this case, the correction provides that each negative n values, $n_{<0}$, is substituted by $n_{<0} + \Delta n$, where $\Delta n = n_{max} - n_{min}$ is the width of the toroidal mode number scale i.e. $\Delta n = 48$. The presence of an aliasing problem is suggested also by observing the 4.3a spectrum, where the right extremity of the $m = 0$ structure is cut and reappears at negative values. For what concernes $m = 1$ fluctuations, the aliasing is confirmed by a comparison with the $S(n, f)$ spectra deduced by applying the two-point technique to the signals from two closely spaced ISIS magnetic coils. As it is clear observing the two spectra in figure 4.5, the peak under investigation actually corresponds to high positive n values and the aliased toroidal mode number spectra, deduced by the toroidal array must thus be corrected.
Summarizing, **a $m = 1$ magnetic activity, characterized by high positive mode numbers and frequency around $70\,kHz$, arises in deeply reversed discharges.**

In figure 4.6, the gradual weakening of the $m = 0$ fluctuations and the concurrent emersion of the $m = 1$ structure, moving towards deeper reversed

discharges, are exhibited. The different $S(n, f)$ spectra are averaged over discharges associated to $q(a)$ values centred around that one specified above each image. The spectra of the sequence have been corrected for the aliasing as

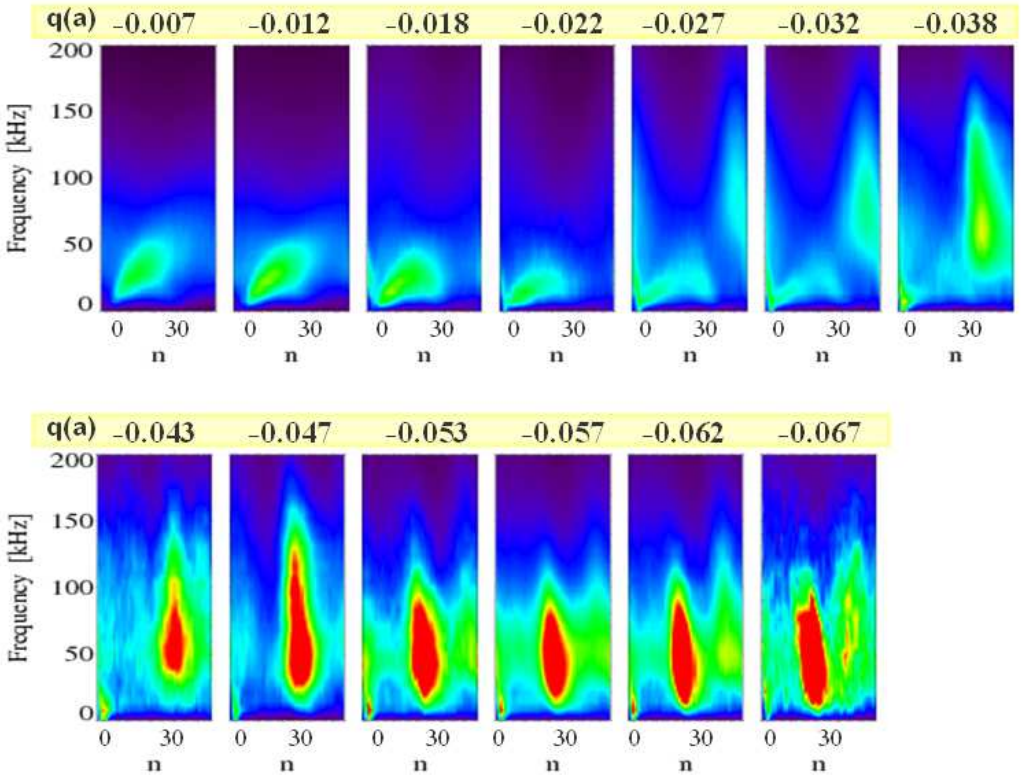

Figure 4.6: Series of $S(n, f)$ spectra obtained by ISIS toroidal array, associated to decresing $q(a)$ values.

explained above. Analyzing this picture, at least three important observations arise. I will treat them in detail in the next three paragraphs.

4.2.1 Externally resonant modes

The analysis of the magnetic activity under investigation at different values of $q(a)$ reveals that the toroidal mode number n, corresponding to the maximum of the fluctuation amplitude is inversely proportional, i.e. $n \cdot \mid q(a) \mid = 1$.

This point is exhibited in figure 4.7. Since the measured poloidal number is $m = 1$, the relation indicates that the observed high frequency modes correspond to magnetic perturbations resonating at the edge of the plasma

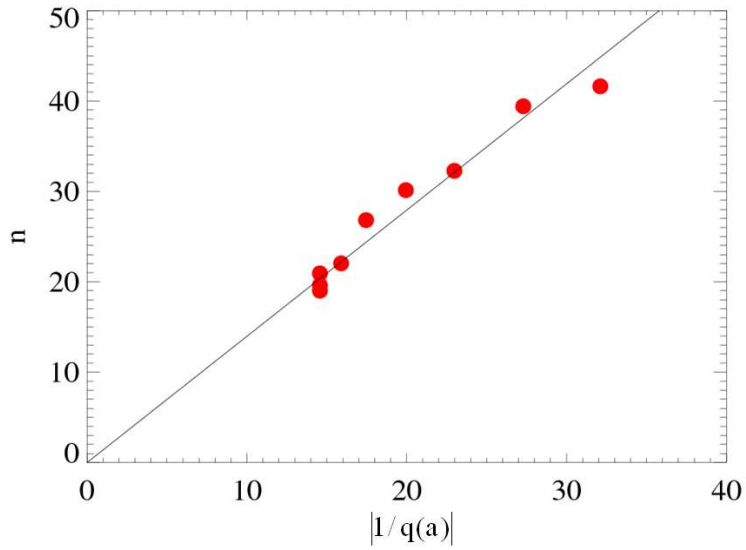

Figure 4.7: The toroidal mode number n referring to the maximum of the activity is inversely proportional to $q(a)$, the value of the safety factor at the edge.

column. Moreover, the determination of the direction of the wave propagation (described in the next section 4.2.2) permits to assert that the modes are characterized by high positive toroidal numbers. In accordance with the RFP nomenclature, these modes are called **externally resonant modes**.

4.2.2 Mode rotation

In figure 4.6, it can be noted that the $m = 1$ peak in the (n, f) plane appears to be almost aligned with the linear dispersion relation characterizing the continuum low frequency $m = 0$ fluctuation. In particular, this can be observed focusing on the spectra where both the activities are present i.e. $q(a) = -0.27,\ -0.32$.
Anyway, figure 4.8 highlights this observation. It shows the same $S(n, f)$ spectra presented in fig. 4.3 after the correction of the aliasing effect. The alignement of the two magnetic activities could provide information about the nature of the frequency of the $m = 1$ modes, since the $m = 0$ fluctuation can be interpreted as the toroidal plasma flow and, thus, the Doppler effect can affect the observations.
The idea that the $m = 0$ activity is associated to the plasma flow is not only due to the fact that the fluctuation phase velocity, v_{ph}, is comparable, both

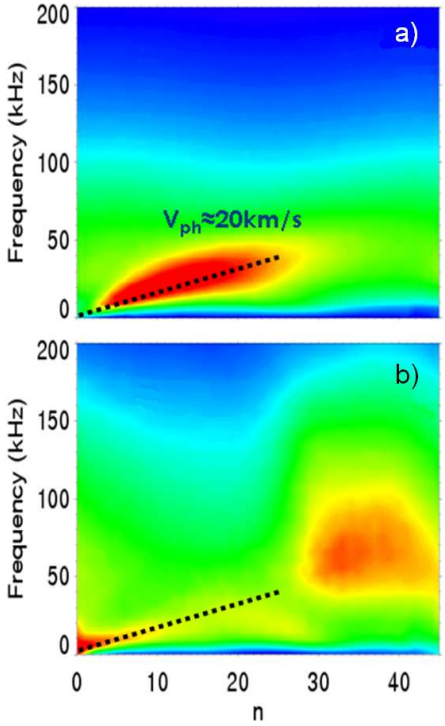

Figure 4.8: $S(n, f)$ spectra at shallow (a) and deep (b) reversal of the magnetic field, after correction of the aliasing effect.

in magnitude and direction, to that of the rotating flow (as mentioned in the first part of section 4.2). Actually, an inversion of the phase velocity sign of the fluctuation is observed when the radial position of the probe is changed, similarly to that measured for the plasma flow, as mentioned at the end of the section 2.2.3 (in particular, fig. 2.13).

In figure 4.9, various $S(n, f)$ spectra, realized by means of the insertable probe at different radial positions are shown. The v_{ph} is observed to exhibit a propagation reversal. The presence of the aliasing affecting the $S(n, f)$ spectra makes some of them difficult to read, but it can be noted that the slope of the activity is directed towards positive n values at more external positions, while towards negative ones at innermost plasma layers.
It is worth noting that in the last image a possible $m = 1$ activity is slightly visible, being probably associated to very high n values since the spectra is affected by aliasing.

A confirmation of the fact that the $m = 1$ mode frequency is associated to the plasma flow rotation is provided by the analysis represented in fig. 4.10. The key to understand the figure is to keep in mind that the modes are resonant

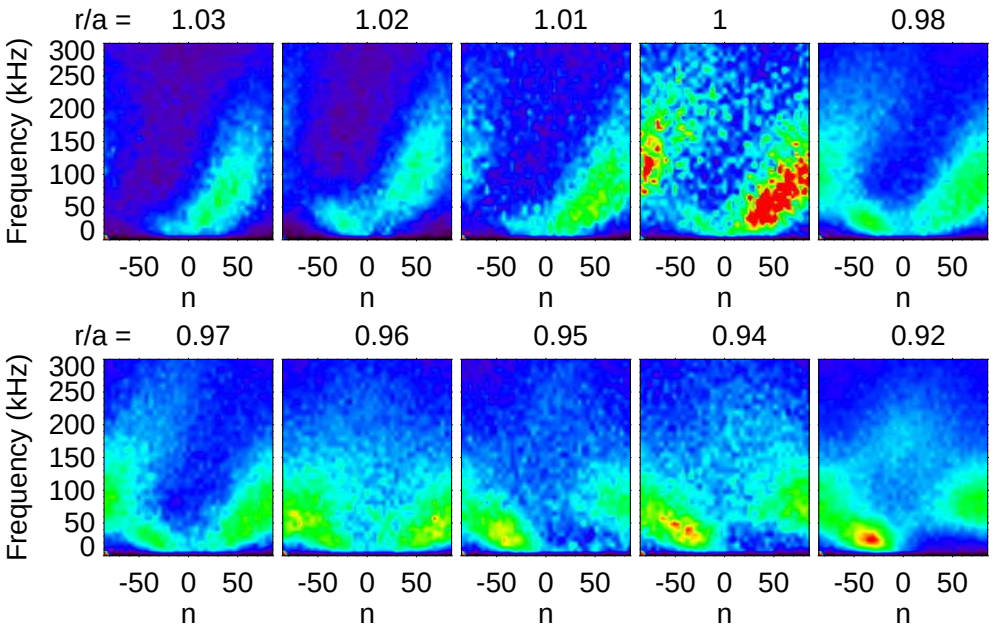

Figure 4.9: Series of $S(n, f)$ spectra obtained by the U-probe at different probe insertions for discharges with shallow $q(a)$ values.

(as shown in 4.2.1), thus the relation $n = 1/\mid q(a) \mid$ is valid. Red points, referring to the *mode frequency*, result by plotting the experimental frequency of the $m = 1$ modes, evaluated as the frequency relative to the maximum of the peak observed in 4.6, versus the inverse of the corresponding $q(a)$ value indicated above the images. Black points, indicated in the figure legend as *Doppler frequency*, have been obtained by means of an extrapolation of the linear dispersion relation of the $m = 0$ fluctuation observed at shallow $q(a)$ values, performed for high frequencies. This extrapolation permits to determine how the modes could be located in the (n, f) plane if they were present at shallow $q(a)$ values, in the case that their frequency would be aligned with the flow dispersion relation: the mentioned relation associates high frequencies to high n values, thus, since the modes are resonant, to high $1/\mid q(a) \mid$ values. It can be seen that the two curves match quite well, thus the alignement is confirmed.
It can be finally restated that this relation between the mode frequency and the plasma equilibrium is due to two constructs: the fact that the modes are resonant relates the equilibrium with the mode number n and the rotation of the modes with the plasma connects n with the mode frequency.

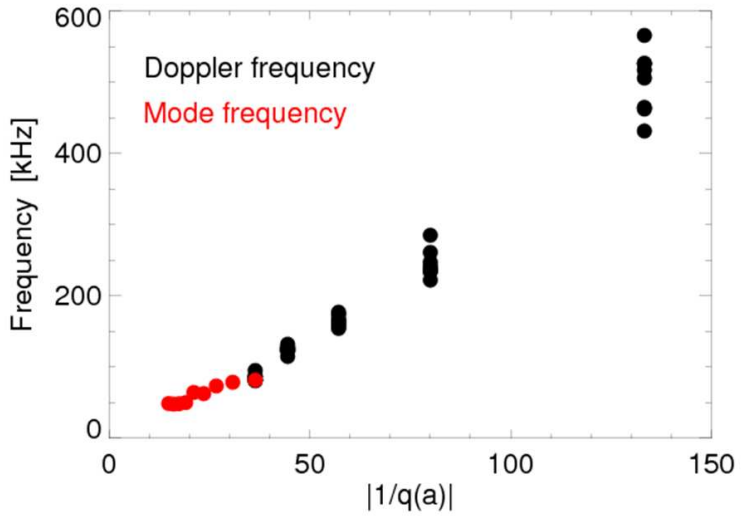

Figure 4.10: Red points are the mode experimental frequencies measured at different $q(a)$ values. Black points are the extrapolated frequency of Doppler affected modes that would grow in shallow reversal discharges.

Summerazing, from this analysis it can be deduced that **since the $m = 0$ fluctuation has been interpreted as the toroidal plasma flow, the alignement of the two modes is an indication that the frequency associated with the $m = 1$ mode is mainly due to a *Doppler effect*, as the mode rotates with the plasma.**

4.2.3 The mode amplitude

The third observation that can arise looking at figure 4.6 is a relevant growth of the power spectrum amplitude of the $m = 1$ fluctuation.
The chromatic scale used in the contour plot, however, does not allow to catch the tendency of the mode intensity at very deep reversal discharges, because the color (red in the picture) is uniform (saturated) beyond a certain threshold amplitude.
A more exahustive and quantitative information is given by figure 4.11, where the experimental amplitude of the fluctuations is plotted versus the value of the safety factor at the edge. Since the signals used for this analysis measure the time derivative of the magnetic field, $\dot{B}_\varphi$, the amplitude of the modes has been evaluated using the integrated signals and selecting the part of spectrum where the $m = 1$ mode is excited. A rapid growth of the amplitude of the

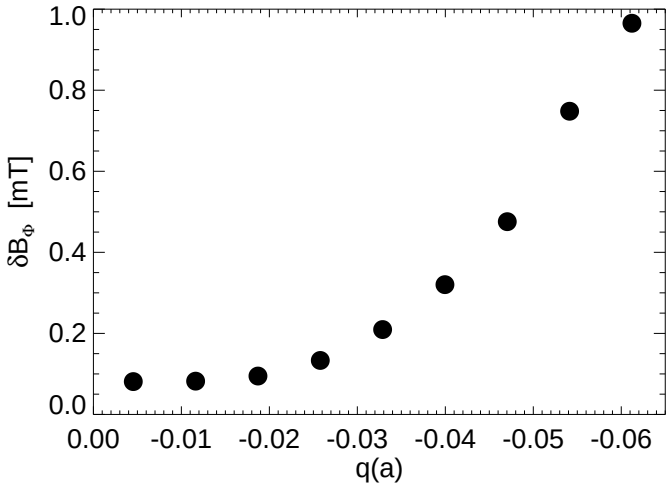

Figure 4.11: The amplitude of the mode fluctuations grows while the safety factor at edge becomes more negative.

modes moving towards deeper reversal equilibria is clearly visible.
The amplitude of the total perturbation produced by these modes is observed to reach values up to almost 1% of the equilibrium magnetic field at the edge in deeply reversed discharges.

4.2.4 Radial eigenfunction

A complementary analysis of the behaviour of the periodicities has been performed by means of the insertable U-probe. In this case, a set of discharges with a safety factor at edge in the range $-0.036 \leq q(a) \leq -0.030$ has been selected. By inserting the U-probe at different radial positions, the series of $S(n, f)$ spectra shown in fig. 4.12 has been produced. The numbers located above each spectrum indicate Δr, the insertion of the probe inside the plasma, as defined in the paragraph 3.1.1. The blank spaces between the spectra are due to the lack of discharges in the required conditions.
In particular, it is worth noting that the amplitude of the fluctuation is modulated along the radial coordinate. Thus, by measuring it as described in 4.2.3, it has been possible to reconstruct the radial eigenfunction of the mode, exhibited in fig. 4.13. The shape of the eigenfunction shows that the mode is localized at the edge of the plasma column.
In the figure the maximum of the mode is localized in corrispondence of the first wall of the vacuum chamber. This can be explained by the fact that

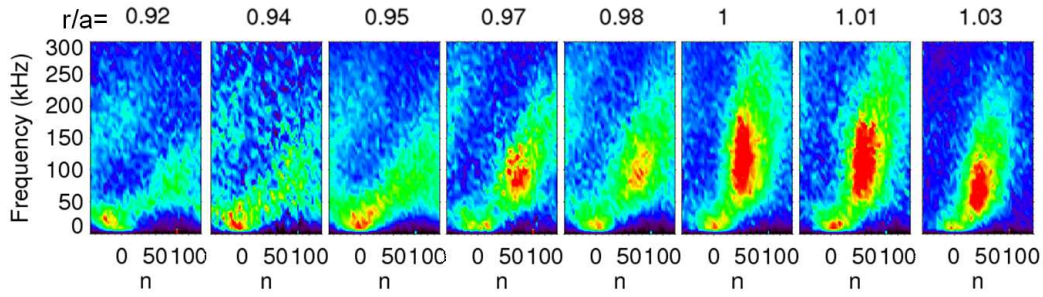

Figure 4.12: Series of $S(n, f)$ spectra obtained by the U-probe at different probe insertions. The q(a) value is included in a narrow range.

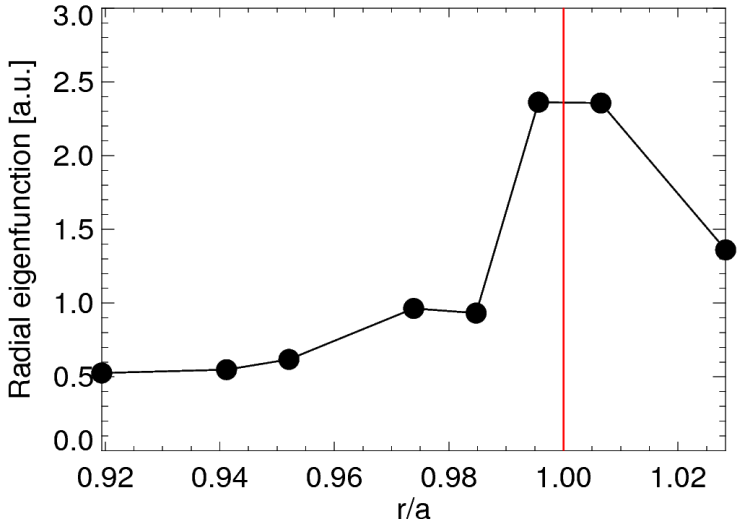

Figure 4.13: The radial eigenfunction of the mode.

the measurement of the magnetic sensors refers to an average value of plasma fluctuations localized in a radius of some centimeters. Thus, since most of the contribution to the measurement comes from the region where the plasma is denser, we can imagine the measurements to be radially shifted, so as to localize the peak inside the plasma. Anyway, for discharges with this equilibrium, the reversal of the magnetic field is located at $r/a \approx 0.9$. This is a further confirmation that these modes resonate externally with respect to the position of the reversal of the magnetic field.

4.2.5 Fast dynamics of wavenumber and frequency spectra

An interesting correlation of the toroidal mode number value and of the frequency of the mode with the fast time evolution of the safety factor at the edge, has been found. Figure 4.14a shows the time evolution of the wavenumber spec-

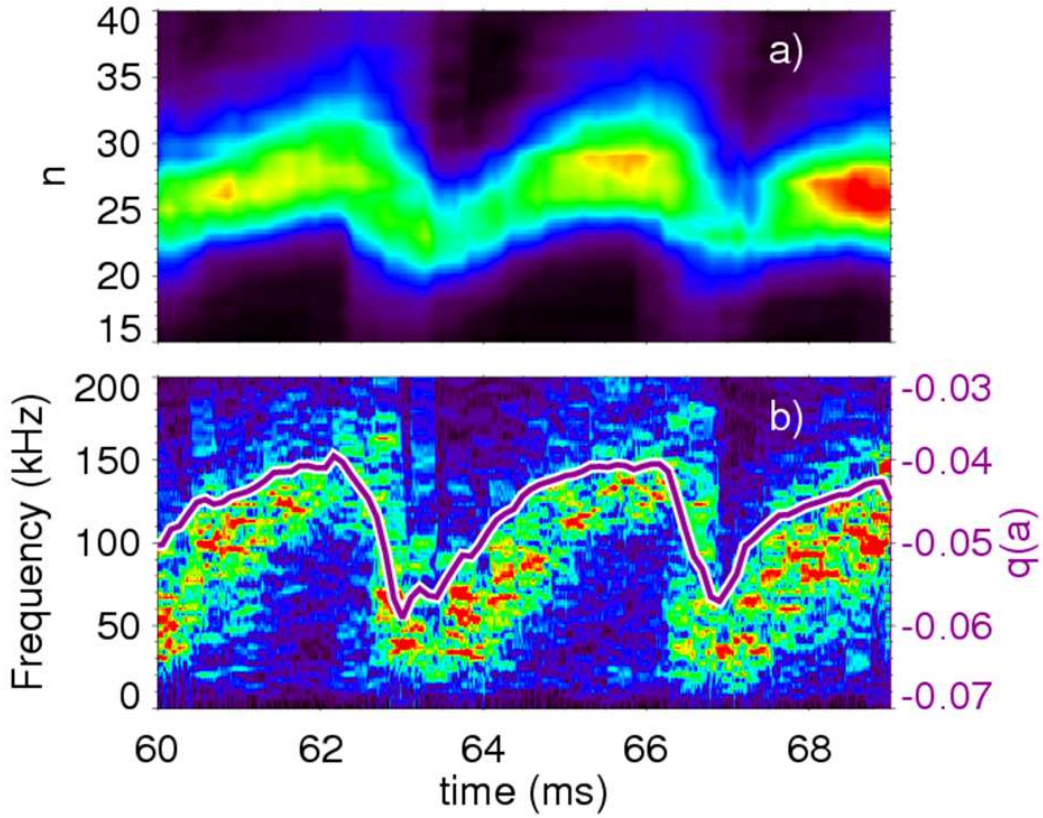

Figure 4.14: (a) Wavenumber specrogram for the toroidal mode number n in the time. (b) Frequency spectrogram. The violet line represents the safety factor at the edge $q(a)$.

trum of the $\dot{B}_\varphi$ signal. It has been calculated by realizing, for successive time lags, an integration of the $S(n, f)$ spectrum over the frequencies relative to the fluctuation under investigation. The relation between n and $q(a)$ (represented by the violet line in 4.14b) is not surprising in the light of what exposed in section 4.2.1, but a so rapid time response of both the modes to grow and the probe system to measure the variation, was not a priori obvious.
In figure 4.14b a frequency spectrogram (see sec. 3.2.2) measured on some milliseconds during the flat top phase of a single discharge is exhibited. The

dynamics of the mode frequency is in turn involved in this fast evolution since the frequency changes in order to maintain the mode aligned with the dispersion relation of the $m = 0$ activity (i.e. to mantain the same phase velocity).

4.2.6 Polarization measurement

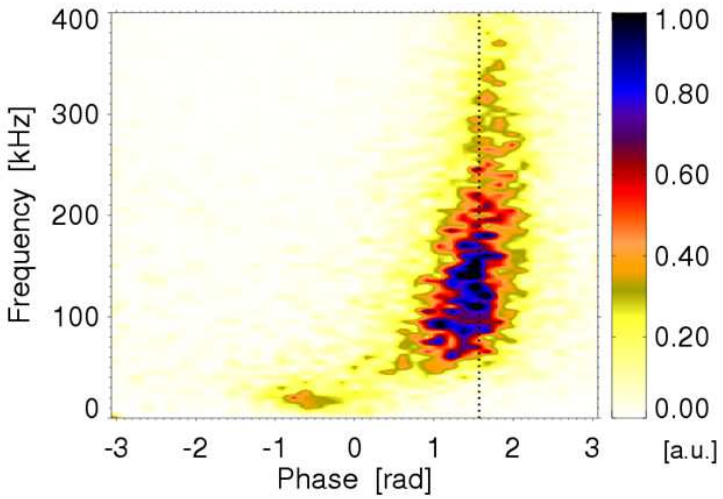

Figure 4.15: Measurement of the phase difference between the radial and toroidal components of the mode.

A measurement of the relative phase (mode polarization) between $\dot{\mathbf{B}}_{\varphi}$ and $\dot{\mathbf{B}}_{\mathbf{r}}$ fluctuating components detected by means of the U-probe coils has been performed.
As shown in 4.15, the phases of the radial and toroidal components of the mode are in quadrature, as expected for a fluctuation of the plasma current component aligned to the main magnetic field (poloidal at the edge of a RFP plasma) that is toroidally propagating with the plasma flow [85].
Thus, the polarization measurement is in agreement with that expected for resonant modes.

4.3 Physical interpretation

In order to formulate a proposal for the physical interpretation of the modes presented in the previous section, the measured spectra have been compared to

the prediction of a linear stability analysis performed by means of the cylindrical code ETAW, already extensively used for RFP calculations [66] and, more recently, successfully benchmarked against the MARS code [86].
The code solves the linear cylindrical resistive incompressible and inviscid single-fluid MHD equations, using a spectral formulation and a matrix shooting eigenvalue scheme. Up to two resistive walls can be considered for the boundary conditions, with a thin shell approximation. The plasma model is solved inside the first wall and the solution is then matched with the external solution of the vacuum cylindrical Laplace equation, analytically known in terms of modified Bessel functions.
For the problem under consideration we have assumed that only one wall is present, which corresponds to a perfect ideal shell located at $r/a \approx 1.05$, i.e. 5% of the plasma minor radius. This choice appears to be the most appropriate, since, as it has been measured (Sec. 4.2.2), the modes rotate at a relatively high speed together with the plasma, and a metal liner with $1 \div 2\, ms$ magnetic field penetration time is present in the RFX-mod device. Therefore, the liner acts as a perfect conductor for these fast rotating modes.
It must be specified that these instabilities evolve through a linear growth phase followed by a nonlinear one and that what we have observed are the saturated energy spectrum of the modes. Thus, it can be objected that a linear model would not satisfy the requirements for a proper description of the modes behaviour. Nevertheless, it is found that the spectral mode properties are in good agreement with the predictions of the linear stability analysis. This point will be more extensively addressed in section 4.3.1.

Figure 4.16 allows a comparison between the spectra of the growth rates obtained by the code (a) and the experimental ones (b). Theoretical growth rates γ (normalized to the Alfvén time) have been calculated for two different q profiles, both deep enough to observe a fully developed $m = 1$ instability: in the case of a deeper reversal, corresponding to $q(a) = -0.05$, the spectrum is peaked at a value $n \approx 25$, while at a shallower reversal, $q(a) = -0.03$, the maximum of the spectrum is at $n \approx 40$.
The experimental data ensue from an average over 10 discharges, comparable in terms of I_p, n_e and $q(a)$, for each of the two reversal values. The toroidal mode number spectra $S(n)$ are obtained by selecting, in the (n, f) plane, the frequencies where the $m = 1$ mode is mostly excited and taking an average of them (in order to obtain the value of the fluctuating magnetic field, magnetic signals have been numerically integrated).
It is worth noting that the theoretical predictions are in good agreement with the experimental $S(n)$ spectra. On the one hand, the values of the toroidal

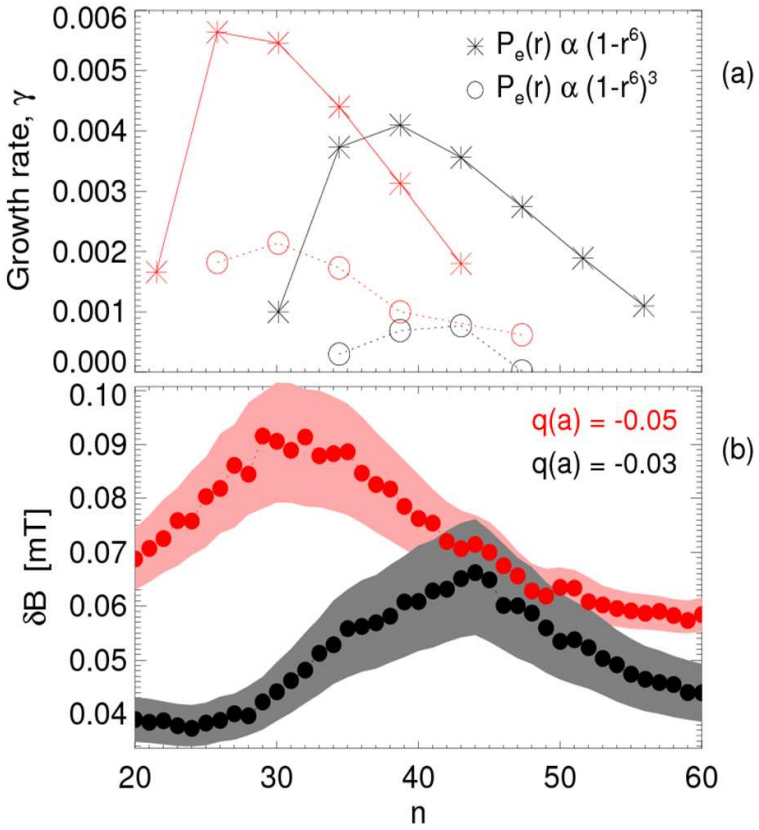

Figure 4.16: (a) Theoretical growth rate (normalized to the Alfvén time) for different toroidal mode numbers, corresponding to two different $q(a)$ values. Different symbols mark the two different plasma pressure profiles used for the simulation. (b) Experimental $S(n)$ spectra under the same $q(a)$ conditions of (a).

mode number are consistent in both equilibria; on the other hand, the relative amplitude of the spectra is the same, i.e. both in the experiment and in the simulation the maximum of the spectrum at shallower reversal is lower. Moreover, similar to the experimental results, the toroidal mode number spectra for a given equilibrium shows that the growth rate vanishes for modes that resonate close to the stabilizing wall (at low n's) and also for modes resonant close to the reversal of the toroidal magnetic field (at high n's), where the effect of the magnetic shear is stronger.

The value of β (defined in 1.22) adopted in the simulation is 2%, comparable to the experimental one for the considered case. It must be added that due to the rather narrow range of the explored β values, the role of this parame-

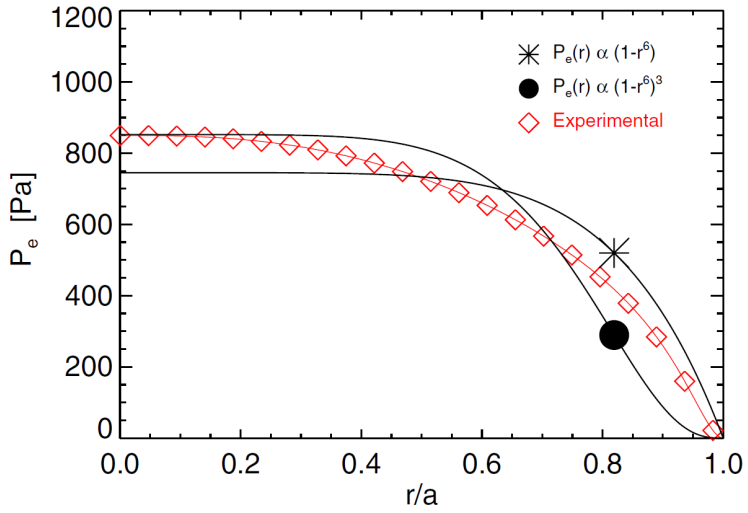

Figure 4.17: The two different radial pressure profiles adopted in the theoretical analysis (black lines) compared with a typical experimental profile (red diamonds).

ter in determining the different dynamics at deep and shallow reversal cannot be experimentally determined. Nevertheless, a useful information can anyway arise by means of the simulations, where two different pressure profiles, shown in figure 4.17, have been considered.
The two profiles for the theoretical estimations (black lines in the picture) are actually intended to represent those corresponding to the minimum and maximum edge gradients measured in the RFX-mod plasmas under the experimental conditions explored here. The two chosen profiles are compared with a typical experimental one in RFX-mod (red diamonds), obtained from density and temperature profiles published in [87, 64], respectively, measured in almost identical discharges.
In figure 4.16a, the different symbols distinguish the two different pressure profiles: the spectra associated to the pressure profile indicated with a "star" is characterized by a growth rate almost triple than those obtained in the case of the "dot" pressure profile, as expected for the interchange instability. Thus, we can infer that the theoretical growth rates at a given β are strongly influenced by the pressure profile. It can be clearly seen that larger edge pressure gradients are associated with larger γ values. Moreover, the results of simulations performed imposing a zero β show that the modes are linearly stable in the absence of pressure.
This observation can be related to what asserted in the section 4.1, that the pressure gradient has a destabilizing effect on the inter-

change modes.

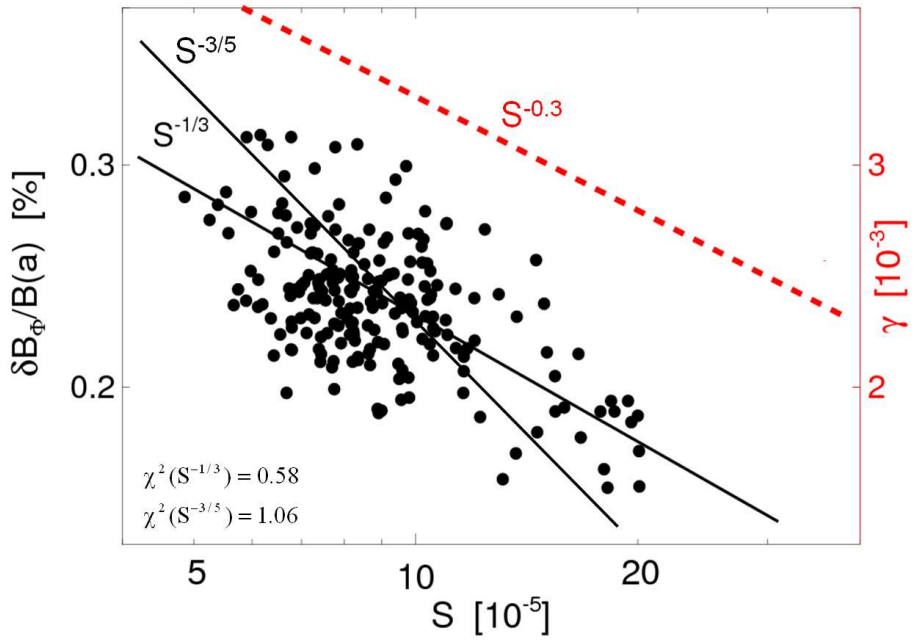

Figure 4.18: Total normalized amplitude of the magnetic fluctuation as a function of the Lundquist number, S, for a given plasma equilibrium ($q(a) = -0.03$). Two theoretical S scalings are overplotted: the $S^{-1/3}$ scaling, predicted for interchange modes, and the $S^{-3/5}$ scaling, predicted for tearing modes. The dashed line, referring to the right-hand side y-axis, represents the dependence on S of the growth rate predicted by the ETAW code for the same plasma equilibrium.

Another interesting observation arising from the comparison between experimental results and the code is that the amplitude of the modes on the one hand and the theoretical growth rate on the other scale in a comparable way with the Lundquist number, S (defined in 1.12) and, in particular, this scaling is in agreement with what expected for interchange modes.
In figure 4.18, the experimental normalized amplitude of the magnetic fluctuations, $\tilde{B}_\varphi/B(a)$, obtained by summing the contribution from each single toroidal harmonic, are plotted versus the relative Lundquist number. The data are consistent for a plasma equilibrium corresponding to $q(a) = -0.03$, chosen as equilibrium, exhibiting a clear $m = 1$ high frequency activity for which the largest range of S values is experimentally available.

Since, as mentioned in Sec. 4.1, it can be seen that the S scaling expected for the interchange modes is different from that expected for the tearing modes,

both the relations are plotted in the figure, in order to compare them with the experimental data and with the trend predicted by the ETAW code, indicating a growth rate scaling as $S^{-0.3}$ (red dashed line referring to the right-hand side y-axis).
Despite the large dispersion of the experimental points, a scaling close to $S^{-1/3}$ is fully compatible with the data. Furthermore, the results of the χ^2 test applied to the experimental data for the two theoretical scalings are indicated in the figure: they state that the $S^{-1/3}$ scaling fits the experimental data better than the $S^{-3/5}$ one.
Other considerations can be added in order to reasonably exclude an interpretation of the observed magnetic fluctuations in terms of tearing modes. First of all, they are generally observed to only slowly rotate in RFX-mod [88], so that they are easily distinguishable from the high frequency magnetic activity under investigation here. Moreover, in the case of tearing modes, any relation with the pressure profile is not expected and finally, such high n values are usually stable.

4.3.1 Quasi-linear saturation model

At this point, we want to address the problem of the nonlinear saturation of these modes.
For this purpose, a nonlinear model would be required (see for example [89]), and/or models taking into account the effects which could affect the stability properties of interchange modes extensively described in the literature, e.g. finite Larmor effects, parallel ion viscosity and diamagnetics effects ([90, 91] and references therein).
However, we want to present here a simple quasi-linear model in which the growth rate is balanced by a dissipation mechanism proportional to the squared mode wave number, which is the consequence of having a Laplacian-like dissipation term in the equations. From the previous observations, it is expected that the measured fluctuation amplitude correlates with some quantity which takes into account both the growth rate and the mode number.
Viscous dissipation operates more effectively on high n, which is the case corresponding to less negative $q(a)$.
As shown in figure 4.19, despite the simplicity of the model, a very good correlation is found between the experimental amplitude of the fluctuations and γ/n^2, that is the maximum growth rate divided by the square of the relative mode number, at different $q(a)$ values.
Future studies are required to better understand why the "footprints" of the linear stability properties are so clearly impressed in the nonlinear saturated

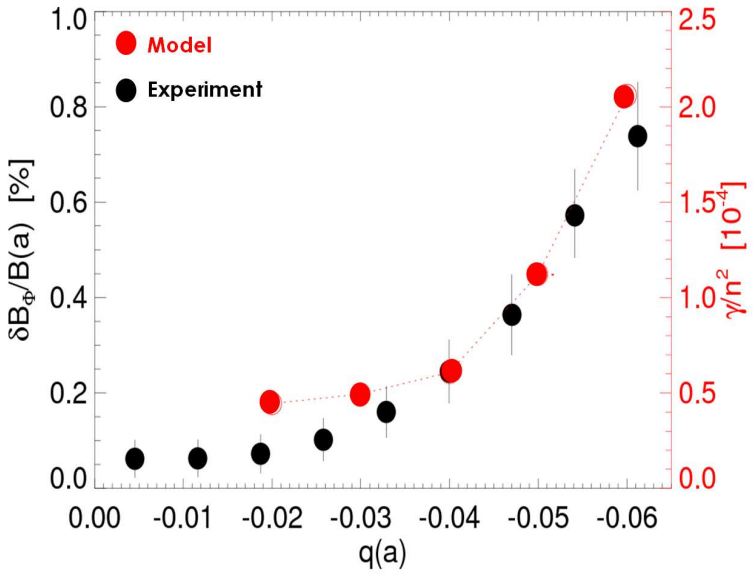

Figure 4.19: The amplitude of the mode fluctuations (black points) and the groth rates normalized to n^2 (red points) towards deeper reversal equilibria.

state of MHD interchange resistive turbulence in our device.

Alfvén Eigenmodes in RFX-mod

In the last decades, Alfvén waves and in particular Alfvén eigenmodes (AE) have been intensively studied by the fusion scientific community. The interest on this topic has grown since wave-particle interactions can have both harmful and beneficial implications. On the one hand they can induce the loss of energetic ions, such as *alpha*-particles (see eq. 1.13), via direct or inverse Landau damping, thus influencing the performance of future reactors [92, 19]. On the other hand they can be used to channel energy from the fast ion population to the background one [93] or to diagnose fundamental plasma parameters [94].

In section 5.1, the theory of Alfvén Eigenmodes (AE) is briefly presented. Then, the first experimental observation of Alfvén eigenmodes in RFX-mod is described and a discussion about their physical interpretation is carried out. Some considerations about the driving mechanism are given in the last section.

5.1 Alfvén Eigenmodes theory

In Sec. 1.4.2, a general introduction about Alfvén waves in infinite homogeneous plasmas, has been given. Solving the MHD equations, three independent dispersion relations for hydromagnetic waves were found (1.48, 1.49 and 1.51) in the axisymmetric cylindrical approximation.
Since it is known that in the RFX-mod plasma $v_S \approx 15\%\, v_A$, the equations to take into account are

$$\omega_A^2 = k_\parallel^2 v_A^2 \qquad \text{and} \qquad \omega_A^2 = k^2 v_A^2 \ , \tag{5.1}$$

describing, respectively, the Shear and Compressional Alfvén Waves (SAW and CAW, respectively)
. In fusion devices SAW are more extensively studied because they are rather likely to become unstable, since $k_\parallel \leq k = \sqrt{k_\parallel^2 + k_\perp^2}$, and therefore, with respect to CAW, less energy is needed to bend the magnetic field lines [95].

It is worth specifing that in real plasmas the distinction between SAW and CAW is not so sharp: they can be coupled together mainly by perpendicular plasma non-uniformities [96]. This topic will be considered in the next section.

The dispersion relations of the Alfvén waves, in a sheared magnetic field, are part of a continuous spectrum, called *Alfvén continuum*. It is difficult to excite instabilities in the Alfvén continuum, because of a damping mechanism. Each wave of a hypothetical wave-packet of finite radial extent generally has different velocities at different radii, so the pulse rapidly disperses. This mechanism is known as *continuum damping*. Nevertheless, in the radially localized points where the continuum damping is not effective, a large variety of discrete modes can be destabilized. In the case of Shear waves, the modes, called **Shear Alfvén Eigenmodes** (SAE), can be divided into two main classes [97]:

- the first one includes discrete eigenmodes which can develop where the degeneracy between two rational surfaces with the same toroidal number is removed by the non-linear coupling of the two modes, creating a gap in the continuum spectrum (e.g. TAE, EAE, HAE).
  The Toroidal Alfvén Eigenmodes (TAE) are probably the most studied Alfvén eigenmodes in toroidal devices: they were first computed by C.Z. Cheng and M.S. Chance (1986) [98] and they are observed in essentially all toroidal confinement configurations [99, 100, 101, 102]; TAE can appear when the degeneracy between two modes with $\mid \Delta m \mid = 1$ and same n is removed by the toroidal coupling.
  In helical equilibrium plasmas, as in stellarators and, maybe, during SHAx states of RFP devices, the symmetry of the configuration is broken in both poloidal and toroidal directions, thus more varieties of AE should exist [103]. These modes are associated with the crossing of two cylindrical Alfvén branches coupled by the helical equilibrium component.

- the second family can occur near an extremum of the continuous spectrum (e.g. GAE, RSAE).
  The Global Alfvén Eigenmodes (GAE), also known as "Discrete Alfvén Waves" or "Alfvén frequency modes" [104], were at the beginning theoretically studied by K. Appert (1982) [105] and experimentally observed by G.A. Collins (1986) [106]; they can be excited at frequencies just below a minimum in the dispersion relation profile.
  Another example of SAE are the Reversed Shear Alfvén Eigenmodes (RSAE) that occur in tokamak plasmas with a minimum in the q profile. The mode resides near the minimum and has a frequency that is above

the continuum frequency, thus avoiding strong continuum damping.

Similarly, the formation of potential wells in the CAW spectrum, due to a combination between the radial variation in density and the perpendicular wave number, allows the development of weakly damped *Compressional Alfvén Eigenmodes* (CAE) [107].

A first experimental study of Alfvén Eigenmodes (AE) in Reversed-Field Pinch (RFP) plasmas, in the form of small wavelength toroidally induced AE, was proposed by G. Regnoli *et al.* [102] in the EXTRAP T2R device; as will be recalled later, the modes described in the mentioned paper have some different features with respect to the ones observed in RFX-mod, in particular, they are characterized by a completely different toroidal periodicity. Moreover, on the Madison Symmetric Torus (MST), interesting studies concerning Alfvén Eigenmodes in RFP plasmas, driven by the fast ions produced with a Neutral Beam Injector, are presently carried out [108].

5.2 Alfvén Eigenmodes: experimental observations

The magnetic activity described in this chapter have been analysed mainly by means of the experimental observations obtained by inserting the U-probe at the level of the graphite tiles, i.e at $r/a = 1.03$. The analysis performed by means of the U-probe data shows coherent magnetic activities at a frequency in the range $0.1 \div 1.3\,MHz$, which will be shown to depend on the Alfvén velocity.
Two kinds of modes have been distinguished in the experimental observations. They can be observed in figure 5.1, representing the spectrogram of the $\dot{B}_\theta$ signal. In order to facilitate the description of the different characteristics, the two modes at higher frequency will be named "Type I" and the other three, intermittent in time, "Type II".

In figure 5.2 we show an example of power spectra of the signals from three U-probe coils measuring the radial, toroidal and poloidal magnetic fields time derivative, $\dot{B}_r$, $\dot{B}_\varphi$ and $\dot{B}_\theta$ respectively, computed in the flat-top phase of a single discharge. Two broad peaks are present in the power spectrum of the $\dot{B}_\theta$ signal, at frequencies around 1000 kHz, in the region characterised by a power law decay of the spectrum.
The $\dot{B}_r$ and $\dot{B}_\varphi$ spectra, instead, are quite different with respect to the $\dot{B}_\theta$

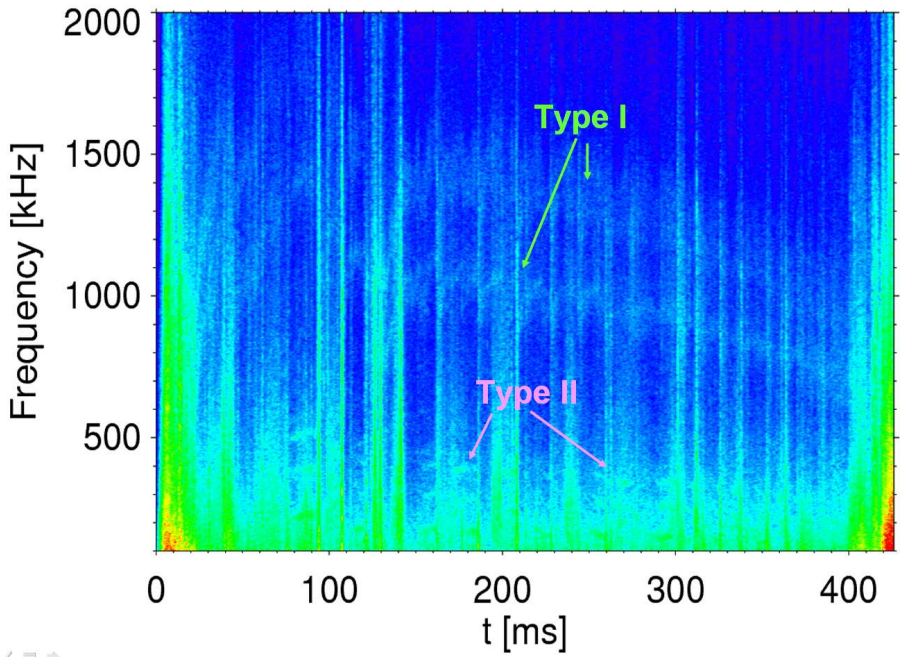

Figure 5.1: Spectrogram of the $\dot{B}_\theta$ signal. Two different kinds of modes are observed: one, named 'Type I', at higher frequency and enduring all the dischange time; the other, named "Type II" at lower frequency and intermittent in time.

one: their fluctuations amplitude is much higher and no coherent peaks are present, but a large bulge occurs at the same frequency of the modes under investigation.
MHD theory requires that SAE would be characterised by the condition $\tilde{B}_\perp >> \tilde{B}_\parallel$, nevertheless they exhibit in general, elliptical polarization (both parallel and perpendicular components), while CAE are expected to have a nearly linear polarization aligned along the equilibrium field [100]. Thus, since in a RFP configuration the magnetic field at the edge of the plasma column is mainly poloidal, a speedy reading of this experimental result would suggest an interpretation of the modes in terms of CAE. Nevertheless, a more careful study of the spectra cannot exclude the SAE interpretation. In particular, the spectrum amplitude of the peaks under investigation is about two orders of magnitude smaller than that of the perpendicular components at the same frequencies: we wonder whether their highly fluctuating and turbulent background, due to different instabilities (mainly resistive tearing and interchange [2] modes), would make it impossible to distinguish in these spectra the coherent, but relatively small, Alfvén modes. Actually, the little bulge could be an indication

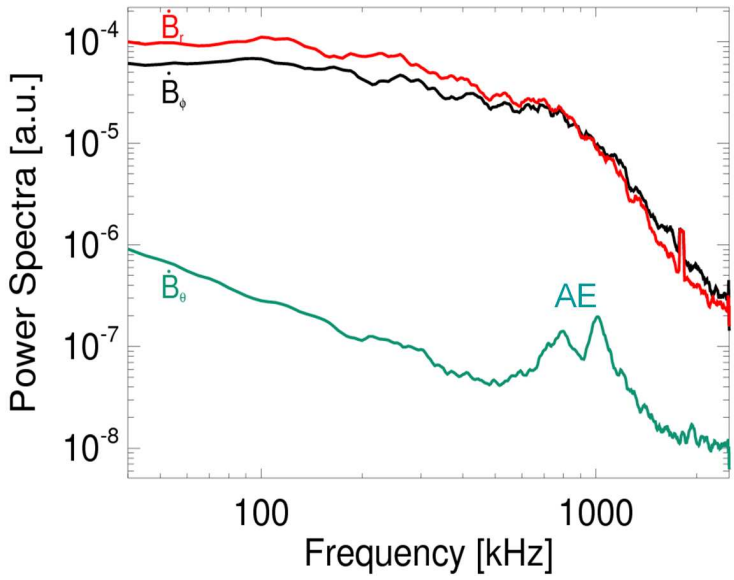

Figure 5.2: Power spectra of $\dot{B}_r$, $\dot{B}_\varphi$ and $\dot{B}_\theta$ signals measured at the position $r/a \approx 1.03$ by the insertable edge probe.

of the presence of alfvénic peaks hidden by the large fluctuation.
Anyway, it is important to remark that in the existing literature it has been proven that perpendicular non-uniformities can lead to the coupling of the Shear and the Compressional Waves [96]. For instance, in NSTX plasmas, some magnetic perturbations characterized by a SAW polarization in the core and the compressional component dominating at the edge, have been observed; these experimental results are in agreement with the simulations performed by the hybrid 3D HYM code (a non-linear, global stability code in toroidal geometry, including fully kinetic ion description) [109, 110]. This means that in real plasmas the SAE and CAE branches are not mutually exclusive.

The Alfvénic nature of the modes is confirmed by an analysis performed in various experimental conditions, corresponding to different plasma current (I_p) and density values and using different working gases (H and He).
As shown in figure 5.3, a linear relation between mode frequency and Alfvén velocity v_A is found. In this analysis, the Alfvén velocity v_A has been evaluated considering the magnetic field at the edge,

$$B(a) \approx B_\theta(a) = \mu_0 I_p \;/\; 2\pi a, \tag{5.2}$$

and the ion mass density as

$$\rho \equiv n_i\, m_i = Z_{eff}^{-1}\, \langle n_e \rangle\, A\, m_p \tag{5.3}$$

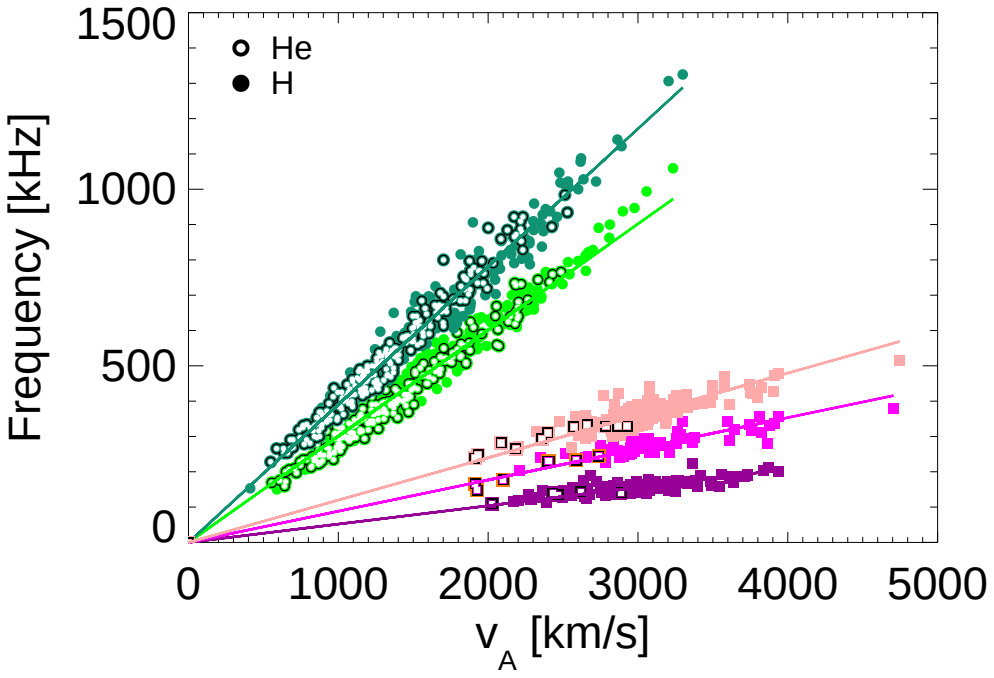

Figure 5.3: Mode frequency versus Alfvén velocity v_A for a wide range of experimental conditions. *Full* points concern the Hydrogen discharges and *open* ones the Helium discharges. Different symbols distinguish the two modes named "Type I" (light and pine green *circles*) and the three modes named "Type II" (pink, orange and purple *squares*).

where m_p is the proton mass, A is the atomic mass and Z_{eff} is the effective ion charge [111].
The electron density value, $\langle n_e \rangle$, used in the computation is actually a line averaged value, obtained from an internal chord of the interferometric diagnostics. The Z_{eff} value has been fixed to 1.5 for H discharges (*full* symbols in the picture), which is typical for RFX-mod H plasmas; the value of Z_{eff} for He shots (*open* symbols), being not measured in the set of discharges considered for the analysis, has actually been chosen in order to make the He curves coinciding with the H ones: $Z_{eff,He} = 3.5$.
It is worth noting that the slopes of the curves constitute distinct experimental wave-vectors. **The observed clear linear relation between the mode frequency and the Alfvén velocity for distinct wave-vectors values suggests that the modes under investigation are actually Alfvén Eigenmodes**.

The experimental values of the so-deduced wave-vectors are reported in the follow. For the Type I modes, they are $k_{exp,1} \approx 2.5\ m^{-1}$ (pine green circles in the picture) and $k_{exp,2} \approx 1.9\ m^{-1}$ (light green circles). Please note that $k_{exp,2} \approx 75\ \%\ k_{exp,1}$: this experimental observation will be used in section 5.3.4. The wave-vector values deduced by the linear relation for the Type II modes are: $k_{exp,3} \approx 0.75\ m^{-1}$, $k_{exp,4} \approx 0.55\ m^{-1}$ and $k_{exp,5} \approx 0.33\ m^{-1}$.

5.3 Global Alfvén Eigenmodes (Type I)

Type I modes consist in two coherent magnetic fluctuations close in frequency, lasting for the whole discharge at a frequency in the range $600 \div 1200\ kHz$ (higher order harmonics are also slightly seen).
Their Alfvénic origin is clearly seen in figure 5.4, where the dynamic evolution of the mode frequency (b) is compared with the plasma current and density time behaviour (a) in a single discharge. In particular, the mode frequency slowly decreases following I_p and, on the other hand, has a sharp reduction in corrispondence with a Lithium pellet injection (at 190 ms), recognizable as a sudden surge of the density measurement.

5.3.1 Mode number measurements

By means of two probes measuring the poloidal magnetic field fluctuations in different toroidal positions and applying the two-point technique, the toroidal periodicity associated with the two Type I modes has been estimated. The result is shown in figure 5.5, where the frequency power spectrum of each toroidal Fourier mode number n, $S(n, f)$, is plotted in a colour-coded contour plot. The modes are visible as two light broad peaks, centred roughly around $n = 0$. The $S(n)$ spectra, overplotted in the picture as continous lines, were obtained by integrating the $S(n, f)$ spectra over the frequency range delimited by the horizontal dashed lines in the figure, corresponding to the two Alfvénic peaks. The lighter curve is associated to the higher frequency peak and the other to the lower one: it must be pointed out that, despite in the example proposed in figure 5.5, the higher frequency peak has a larger amplitude than the one at smaller frequency, this condition is not always verified.
Despite the large width of the $S(n)$ curves, imputable to the statistical approach, both spectra are observed to have a maximum corresponding to a $n = 0$ periodicity; it must be added that this estimate seems to be the most frequently measured value on a statistical basis over more than 50 discharges.

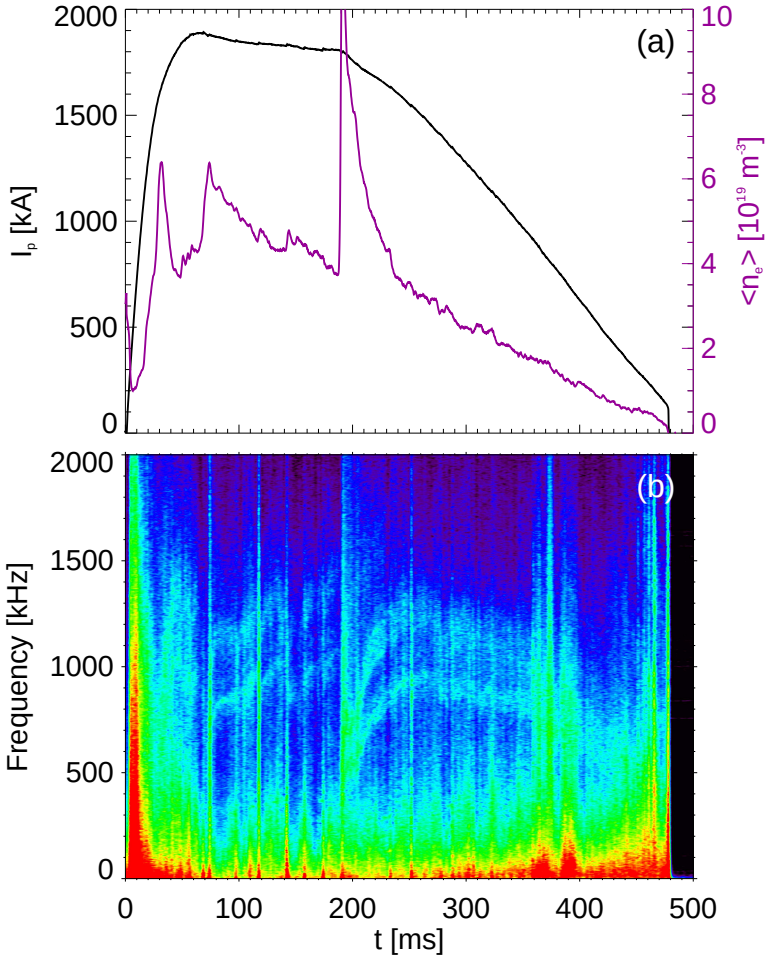

Figure 5.4: a) Plasma current I_p (left axis) and electron density $\langle n_e \rangle$ (right axis) time evolutions; b) spectrogram of a $\dot{B}_\theta$ signal for the same discharge.

Moreover, in some experimental campaigns the U-probe has been rotated in order to measure the poloidal periodicity associated with the AE under investigation. An analysis similar to that described for the measurement of the toloidal mode number gives a statistical evaluation of m. The poloidal mode number value is consistent with $m = 1$ for both peaks.

Finally, the radial wave-vector component k_r has been estimated using

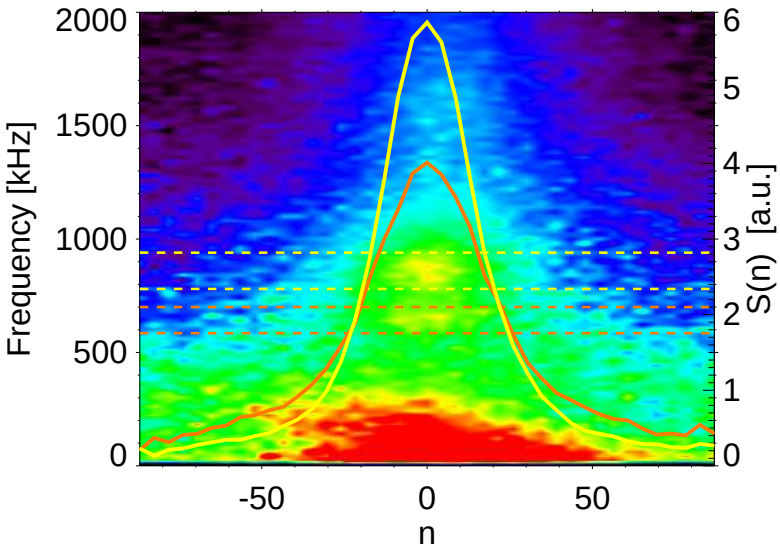

Figure 5.5: $S(n, f)$ deduced by the two-point analysis using two poloidal magnetic coils toroidally separated. The right handside y-axis refers to the $S(n)$ spectra relative to the two Alfvénic peaks, shown as continous lines.

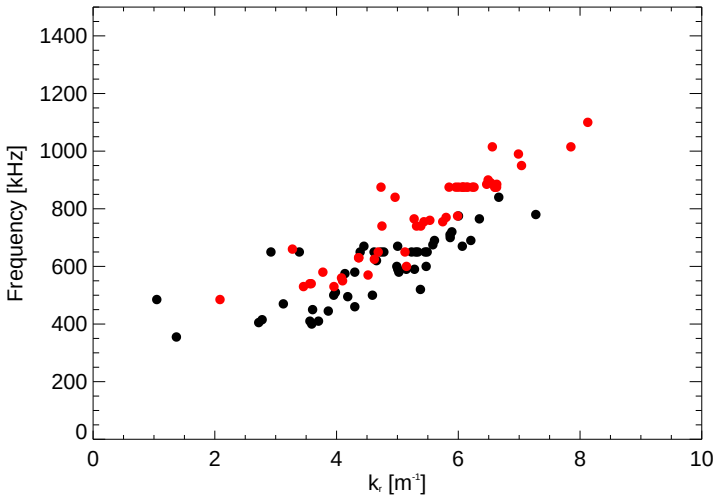

Figure 5.6: Linear relation between the mode frequency and the relative radial wavevector component. The two colors distinguish the two peaks: the red symbols refer to that at higher frequency.

two $\dot{B}_\theta$ probes belonging to the same radial array, at different radial positions ($\Delta x = 12\,mm$) and applying the two-point technique: an unexpected, and still under investigation, linear relationship between the frequency of the

modes and the radial wave-vector has been observed. The average value of the measurements gives $k_r \gtrsim 5\ m^{-1}$.

5.3.2 Frequency splitting

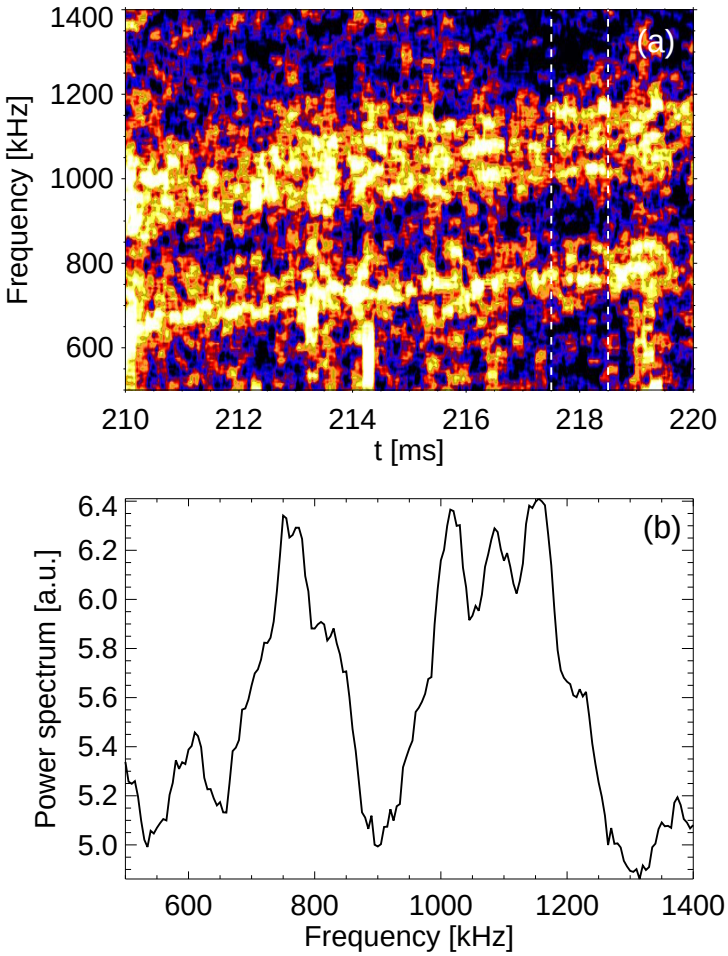

Figure 5.7: a) Spectrogram of a $\dot{B}_\theta$ signal. b) Power spectrum of $\dot{B}_\theta$ evaluated in the time range $217.5 \div 218.5\ ms$.

An interesting phenomenon has been observed performing an analysis of the spectra in plasma conditions characterized by a high Alfvén velocity, i.e. by

modes with a frequency of the order of MHz: in some discharges **it is possible to recognize a splitting of the mode frequency**. In particular, as can be observed in the spectrogram of figure 5.7a, the mode at higher frequency is mainly involved in this phenomenon. A fine structure can be, indeed resolved observing in detail the higher mode.
By means of an integral of the spectrogram in the time range delimited by the two vertical dashed lines ($217.5 \div 218.5\ ms$), the spectrum in figure 5.7b has been obtained: three thin peaks, composing the higher frequency mode, can be distinguished.
It is interesting to note that similar phenomena have been already observed to arise in TAE at JET [112] and in CAE at MAST [113]. It has been shown [112] that a non-linear model for kinetic instabilities developed by Berk and Breizman [114] predicts that a single-frequency mode can split into multiple lines when the instability growth rate dominates the effective collision frequency of the resonant particles.

5.3.3 The role of magnetic reconnection

As mentioned in section 2.2.3, RFP plasmas are characterized by quasi-periodic spontaneous relaxation events, known as Discrete Reconnection Events (DRE). Two interesting effects regarding the Alfvénic mode behaviour during these rapid events have been observed. The first one, concerning the enhancement of the amplitude of the spectrum associated to Type I AE in correspondence of a reconnection event, is exposed in this section; the second effect, by which it has been possible to radially localized the modes, is set out in next section, devoted to the physical interpretation of the modes (Sec. 5.3.4).

Enhancement of the mode spectrum amplitude during DRE.
In order to study the mode response during DRE dynamical phases, a statistical approach has been adopted, by means of a conditional averaging procedure over a number of single events: different DRE, recognized by the rapid fall of the safety factor at the edge $q(a)$, have been selected from a discharge having a quite uniform time evolution of I_p and $\langle n_e \rangle$; then a new time base t_c has been defined fixing the zero at the instant when the $q(a)$ has a minimum.
In figure 5.8b the evolutions of $q(a)$ (solid line) and of the relative spectrogram, both obtained by a conditional averaging process over multiple events, are shown: the two modes can be recognized at 650 and 850 kHz and a global increase of the fluctation amplitude is observed at $t_c \approx 0$. The last point becomes evident in figure 5.8a, where a comparison between the power spectra

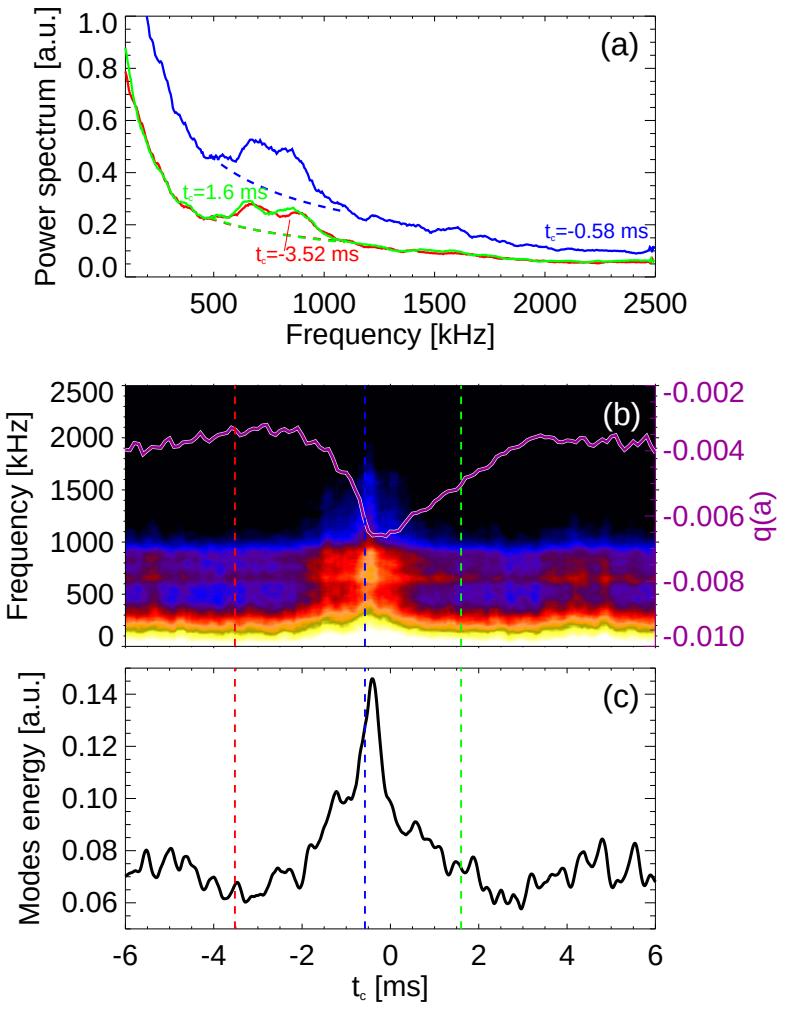

Figure 5.8: a) Power spectra of a $\dot{B}_\theta$ signal referring to three instants of the crash evolution. b) Spectrogram obtained by a conditional average over different time intervals centered on a single DRE (the solid line represents the averaged $q(a)$). c) Time evolution of mode energy.

referring to three different moments of the $q(a)$ dynamics is exhibited: the power spectrum amplitude associated with the $q(a)$ minimum instant is considerably larger.
It is worth noting that not only the amplitude of the background spectrum (whose origin is still under debate) grows, but also the amplitude of the AE spectrum is particularly enhanced.

To estimate the energy strictly associated with the AE, we integrated the spectrum over the frequencies in the range $500 \div 1050\ kHz$, after subtracting the fluctuation background, represented by the dashed lines obtained interpolating the spectrum-broad-band in terms of a frequency power law (figure 5.8a). It is worth noting that the evolution of the mode in figure 5.8c shows that its amplitude has pratically doubled during the reconnection event.
This observation can be a significant starting point in the discussion about the possible drive mechanisms of the Alfvén Eigenmodes under consideration. In particular, at this point we cannot distinguish whether the increase of the background and of the AE amplitude is caused by the same drive or not.
This interesting subject will be recovered in the section 5.5, where some remarks about the possible mechanisms driving the alfvénic modes are pointed out.

5.3.4 A possible physical interpretation: GAE

Given the experimental observations, it is now necessary to make some considerations in order to try to give a physical interpretation to such Alfvén Eigenmodes.
As described in section 5.2, the estimation of the wave-vector has been obtained by the linear interpolation of the experimental frequencies at different Alfvén velocities: in the case of Type I modes, their value is around 2.
As stated before, two main branches of AE must be considered: the SAE, characterized by a dispersion relation where only the parallel component of the wave-vector appears ($\omega_A = k_\parallel v_A$) and the CAE, for which the whole wave-vector must be taken into account ($\omega_A = k v_A$).
Therefore, an interpretation of the modes in terms of CAE would require a relation between the frequency and the Alfvén velocity regulated by

$$k = \sqrt{k_r^2 + k_\theta^2 + k_\phi^2}, \tag{5.4}$$

where k_r, k_θ and k_φ are the radial, poloidal and toroidal wave-vector components respectively. The experimental measurements of the mode numbers reported in Sec. 5.3.1, from which $k_r \gtrsim 5\ m^{-1}$,$k_\theta \gtrsim 2\ m^{-1}$ and $k_\varphi \approx 0$, entail a total value to be at least $k \gtrsim 7\ m^{-1}$. Such a value seems probably too large to be consistent with the k_{exp} values obtained by the relation of the measured frequency with the Alfvén velocity of the various plasma conditions explored. On the other hand, according to the SAE hypothesis, the wave-vector compo-

nent affecting the first dispersion relation of 5.1, is

$$k_{\parallel}(r) = \frac{\mathbf{k}\cdot\mathbf{B}}{\mid \mathbf{B} \mid} = [m + nq(r)]\frac{B_\theta(r)}{r \mid \mathbf{B}(\mathbf{r}) \mid}. \tag{5.5}$$

Taking into account the periodicity measurements, it is simple to verify that the k_{exp} evaluated by the interpolation are in good agreement with the $k_{\parallel}$ estimated. Indeed, the sum between squared brakets gives ≈ 1, being both n and $q(r)$ values very close to zero, so that their product can be neglected. Then, if the modes are localized at the plasma edge, $r \approx a$, the poloidal magnetic field is comparable to the main one and their ratio is ≈ 1, so $k_{\parallel} \approx 2$. Otherwise, if the modes reside more inside $r \lesssim a$, we can consider the two magnetic components being similar, so $B_\theta/B \lesssim 1$; thus the resulting $k_{\parallel}$ is the same.
It is therefore reasonable to associate the modes observed in RFX-mod plasma to the Shear branch.

The following analysis is devoted to investigate the possible occurrence of gaps in the continuum of Alfvén dispersion relation at the frequencies where the modes here described are observed. Both the gaps generated by the toroidal coupling (TAE case) or by the presence of a minimum (GAE case) in the Alfvén frequency radial profile, $f_A(r)$, are considered. In the TAE case, the proper correction to the dispersion relation due to toroidicity and causing the modes coupling has been derived for the RFP configuration by G. Regnoli *et al.* (2005) [102]; the dispersion relation takes the form:

$$\omega^2 = k_{\parallel}^2(r) v_A^2(r) \gamma(r) \tag{5.6}$$

where

$$\gamma = \frac{1 + \sigma \pm \sqrt{(1-\sigma)^2 + \epsilon_0^2 \sigma}}{2 - \epsilon_0^2/2} \qquad \text{and} \qquad \sigma = k_{\parallel,m+1}^2 / k_{\parallel,m}^2 \qquad ;$$

the ϵ_0 parameter, representing the gap width, is small but finite at the edge of a RFP plasma. In [102] it was estimated as $\epsilon_0 \sim 2\,r/R$.
Regarding the Global Alfvén Eigenmodes, the presence of an extremum (e.g. a minimum) in the dispersion relation profile is an essential ingredient for their development. The radial profiles of the electron density and of the safety factor (obtained as mentioned in Sec. 3.1.3), representative of a general behaviour, are shown in the figures 5.9a and 5.9b, respectively. By means of such quantities, the Alfvén frequency profiles have been simulated (fig. 5.9c): the dashed curves refer to the continuum shear dispersion relation (the first of eq. 5.1), the solid ones, taking into account the toroidal coupling, refer to the expression 5.6. The $k_{\parallel}(r)$ profile used is defined in equation 5.5; different poloidal ($m = 0, 1$)

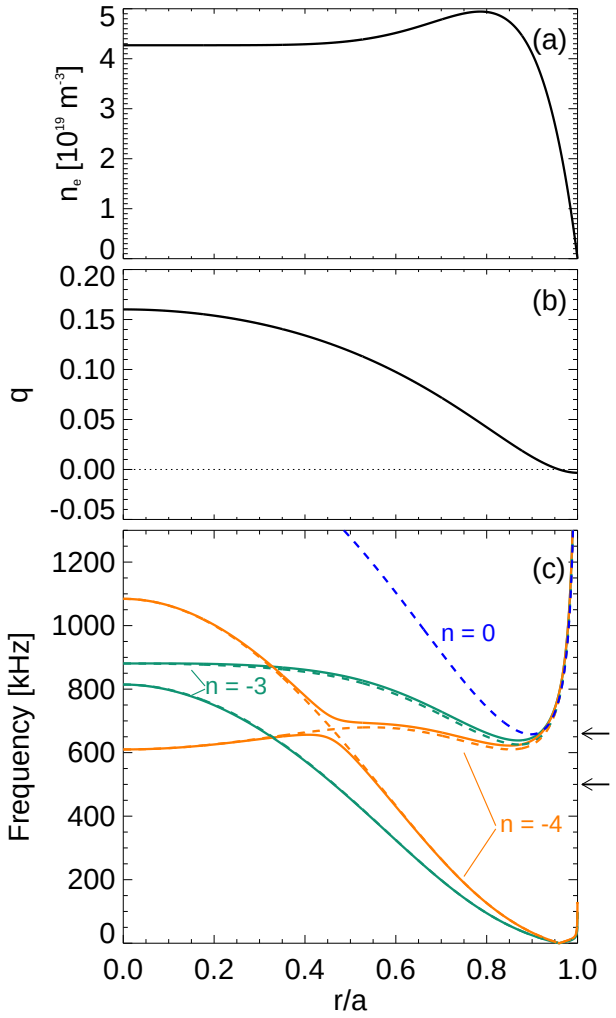

Figure 5.9: Radial profiles of the electron density n_e (a), of the safety factor q (b) and of the Alfvén frequency f_A(c) for different poloidal $m = 0, 1$ and toroidal $n = 0, -3, -4$ periodicities, in cylindrical (*dashed lines*) and toroidal (*solid lines*) approximations. The two arrows on the left indicate the experimentally observed frequency values (for the Type I modes).

and toroidal ($n = 0, -3, -4$) mode numbers have been considered. The two arrows on the left side of the picture indicate the frequencies of the modes experimentally observed in the $\dot{B}_\theta$ power spectrum of the same discharge at the same instant.
It is worth noting that the curves with a local minimum at the edge represent

the $m = 1$ modes and that the crossing between modes with different m and the consequent toroidicity-induced coupling occur only for toroidal numbers $\mid n \mid \geq 4$. The measurement of the toroidal periodicity would suggest an interpretation in terms of GAE, nevertheless, since it is based on a statistical approach (Sec. 5.3.1), the TAE option cannot be totally excluded.

However, referring to figure 5.9c, it is possible to deduce that the discriminating factor can be the localization of the modes: TAE develop inside the plasma, and GAE at the edge. A useful indication in this sense emerged from the observation of the mode response during a single reconnection event: **the modes are localized at the edge**.
The large and rapid variation of the safety factor at the edge $q(a)$, sign of a global relaxation, and the relative spectrogram of the modes are presented in figures 5.10a and 5.10b respectively. As described in the previous paragraph and observed in the mentioned spectrogram, a global increase of the magnetic fluctuations at all frequencies occurs during the DRE. Moreover, immediately after the fluctuation growth, the modes exhibit a reduced frequency, that recovers its pre-reconnection value in few milliseconds. The dashed curve overplotted on the spectrogram represents the mode frequency calculated using the plasma parameters presented above (I_p, Z_{eff} and $\langle n_e \rangle$, that, we remind, is estimated from an internal chord of the interferometric diagnostics, so it is an average value) and the experimentally obtained $k_{exp,2}$ value. It is worth noting that this estimate can not explain the rapid fall of the measured frequency. On the other hand, the solid curve, obtained by plotting the frequency values of the continuum minimum relative to the $(m, n) = (1, 0)$ curve, which takes into account the density radial profile, at different time instants, matches quite well the experimental frequency dynamics. The mode frequency depends on the value of the plasma density at the radial position where the modes are excited; in figure 5.10c, three $\langle n_e \rangle$ radial profiles in different time instants are shown. The profile shape and especially the density value in the edge region exhibit an interesting dynamics during the reconnection process: a rapid growth of the density occurs mainly around $r/a \simeq 0.8 \div 0.9$ during the DRE, as already more extensively documented elsewhere [115]. This observation seems to confirm that the modes are actually localized at the very edge of the plasma column.
Concluding, since the toroidal mode number values are centered around zero and the mode has been localized at the edge (Sec. 5.3.3), it is evident that **the experimental observations are mainly consistent with the minimum of the** $(m, n) = (1, 0)$ **continuum, so with the Global Alfvén Eigenmode interpretation.**

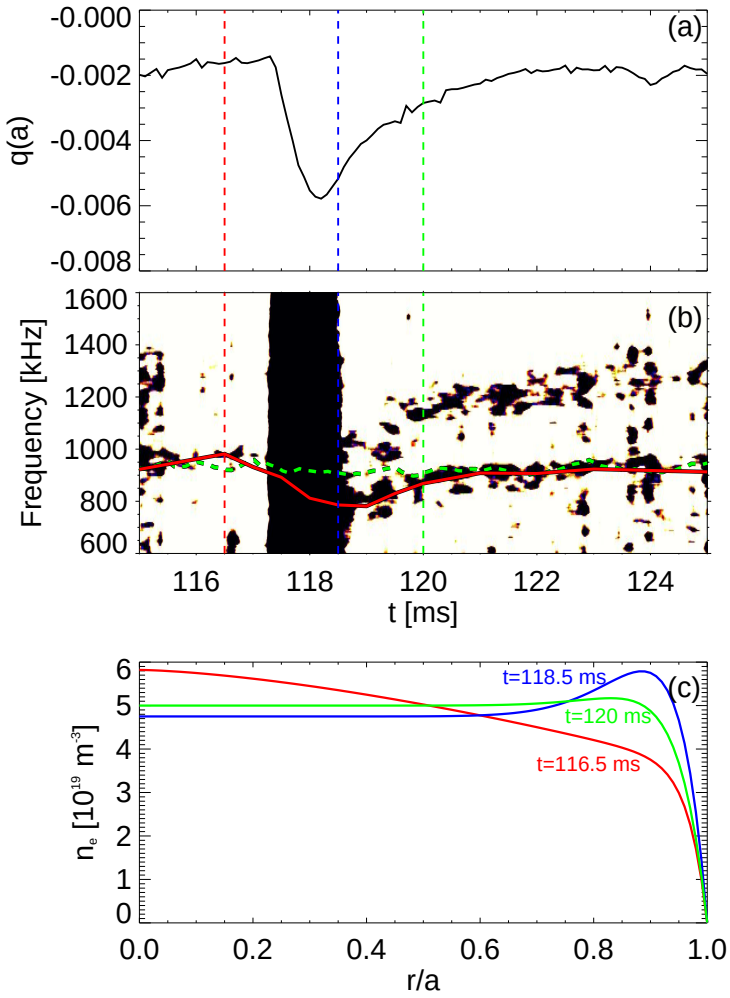

Figure 5.10: A reconnection event is recognized by the abrupt fall of the safety factor at the edge $q(a)$ (a) and by the global increase of the $\dot{B}_\theta$ fluctuations (b). The dashed line represents the mode frequency as estimated by the plasma parameters (I_p, $\langle n_e \rangle$, Z_{eff}, $k_{1,exp}$), the solid one is the time evolution of the frequency minimum of the continuum. c) n_e radial profiles at three different instants.

Finally, an interesting element in the physical interpretation of the experimental results could be the close agreement of the experimental observations with those, named Alfvén Frequency Mode (AFM), obtained in TFTR and

described by Z. Chang *et al.* [104].
In particular, in both TFTR and RFX-mod devices, despite the largely different magnetic topologies, it has been observed that two modes are present at a frequency linearly depending on the Alfvén velocity and that they are separated in frequency by about 25% (see the section 5.2 of this thesys and the figure 2 of [104]).
In TFTR ohmic plasmas, the estimation of the mode numbers by means of Mirnov coils gave $(m, n) = (1, 0)$ for both peaks; these values are consistent with the mentioned possible interpretation of the modes in terms of GAE.
Moreover, the activity here investigated has been recorded in all the high density discharges considered, while in low density regimes the modes seem to appear less frequently (at $\langle n_e \rangle < 1 \times 10^{19}\ m^{-3}$ the Alfvénic modes are extremely weak); in the mentioned paper, above a threshold value, a clear linear dependence of the mode amplitude on the electron density was exhibited (figure 10 of [104]). In both experiments it has been observed that an abrupt increase in $\langle n_e \rangle$ (e.g. pellets) induces not only a sharp drop in the mode frequency, but also an enhancement of the mode amplitude (see figure 5.4).
A further similarity between the experimental observations of RFX-mod and TFTR is that the modes are localized in both devices at the edge.
Later on, AFMs have been theoretically explained in terms of $n = 0$ Global Alfvén eigenmodes [116]. According to the mentioned paper, the presence of a double $(m, n) = (1, 0)$ mode is explained in term of the quantization condition of the radial component of the wave-vector, the two eigenfrequencies being localized in close but different radial positions.

5.4 Alfvén Eigenmodes during SHAx states (Type II)

Differently from those of the Type I, Type II AE, characterised by a frequency in the range $100 \div 600kHz$, have been found only in high plasma current discharges ($I_p > 1.5MA$). In particular, the presence of the mode is discontinuous in time, being strictly related to the time evolution of magnetic equilibrium. This is evident from figure 5.11, representing a spectrogram of the U-probe $\dot{B}_\theta$ signal for a $I_p \approx 1.8MA$ discharge. Some relatively weak, coherent peaks are seen to appear when the dominant tearing mode ($m = 1$, $n = -7$) amplitude (toroidal component), shown by the red continuous line referring to the right-side y axis, is very high.
As previously mentioned (Sec. 2.2.2), high plasma current discharges in RFX-

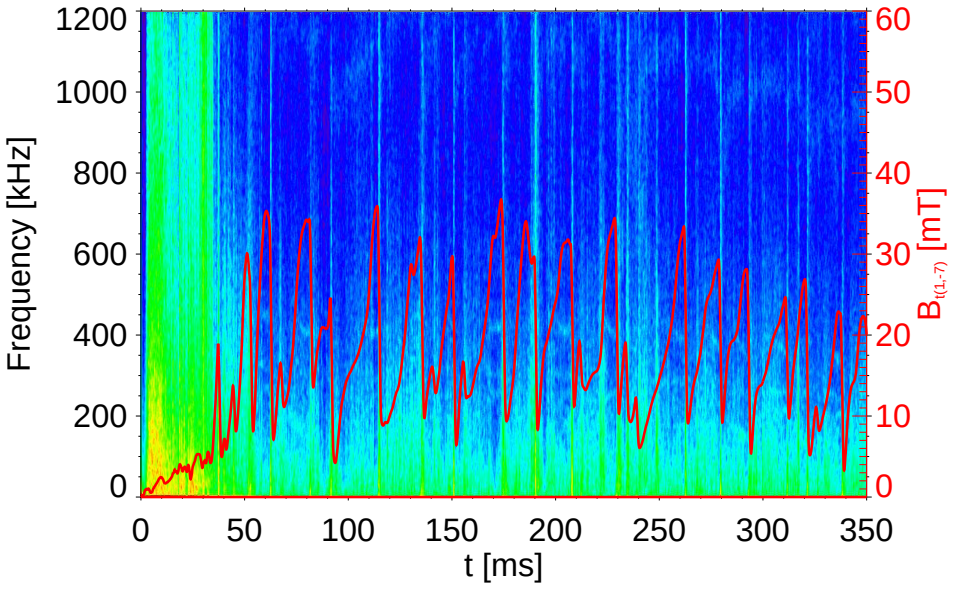

Figure 5.11: Spectrogram of U-probe $\dot{B}_\theta$ signal. The red line is the (m,n)=(1,-7) toroidal magnetic field component.

mod are characterised by the spontaneous transition to a helical equilibrium, the Single Helical Axis state (SHAx). The fact that SHAx states are intermittently interrupted by reconnection events causing rapid transitions to the multiple helicity regime, involves the disappearing of the Type II modes.

In figure 5.12 two power spectra of the $\dot{B}_\theta$ signal, obtained selecting in the same discharge, time instants characterized by different magnetic topologies (MH and SHAx), are shown. It is worth noting that, while the Type I modes, interpreted as GAE, are continuously present during the discharge, the Type II peaks (in this case only one is visible, at about $400\,kHz$) appear only during the SHAx states.

5.4.1 Mode number measurements

The mode number measurements associated to the Type II fluctuations are not clear, because of the difficulty to isolate the activity of interest by the background fluctuation.

Nevertheless, some preliminar evaluations of the toroidal mode numbers have been performed and they place the n value roughly in the range $n \approx 0 \div 4$.

As regards to the poloidal mode number, we can say that long-wavelength

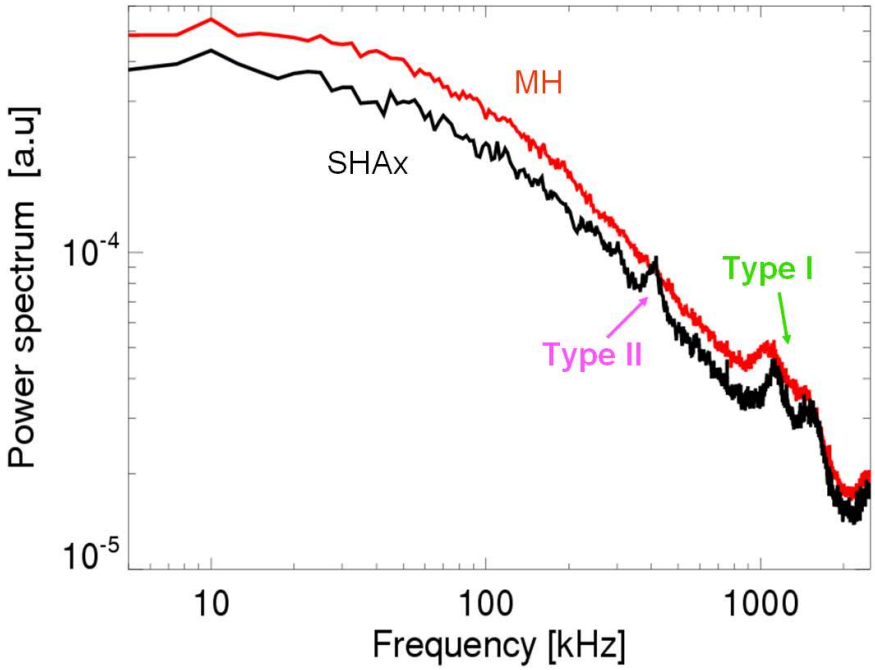

Figure 5.12: Power spectra of $\dot{B}_\theta$ signal for the different topologies (MH and SHAx states).

components has been observed.

5.4.2 Possible physical interpretations

Further analyses are needed to give a physical interpretation of Type II modes. Certainly, a fundamental information is that they arise only when the plasma spontaneously organizes in a helical equilibrium.
This observation brings to mind the huge literature on the the study of Alfvén modes in stellarators. In particular, in these devices the break of the axial symmetry of the magnetic configuration causes the appearance of gaps in the Alfvén continuum which are absent in tokamaks. Deriving a basic equation for the SAE in flux coordinates [103], it can be seen that two cylindrical Alfvén branches, intersecting at the same frequency $\omega_A(m,n) = \omega_A(m+\mu, n+\nu N)$, can be coupled by any given Fourier harmonic of the magnetic field, $\epsilon^{(\mu,\nu)}$, where the coupling numbers μ and ν are integers and N is the number of periods of the equilibrium magnetic field. In the case where both coupling numbers are not null, the gap is said to be helicity-induced and **Helical Alfvén Eigenmodes** can develop.

For the case of the described observations about the Type II modes in RFX-mod device, a collaboration with the Oak Ridge National Laboratory (USA) is presently undergoing with the aim of studying the 3D effects of the helical equilibrium during SHAx states, on the Alfvén continuum and on the possible couplings. In particular, the AE3D code is going to be applied to the peculiar RFX-mod magnetic and pressure profiles (in a self-organized $N = 7$ device) in order to investigate the eigenfunctions and the stability properties of the Alfvén instabilities. An important point to be addressed is to verify if the frequency ordering prescribing the HAE one to be fairly higher than that of the TAE [103], which is known to be valid for stellarators, must apply also to the RFX-mod case. This would be an interesting analysis as seen in fig. 5.9, in RFX-mod TAE frequency has been evaluated to be comparable to the GAE one while the frequency of the Type II modes is generally lower by a factor 3.

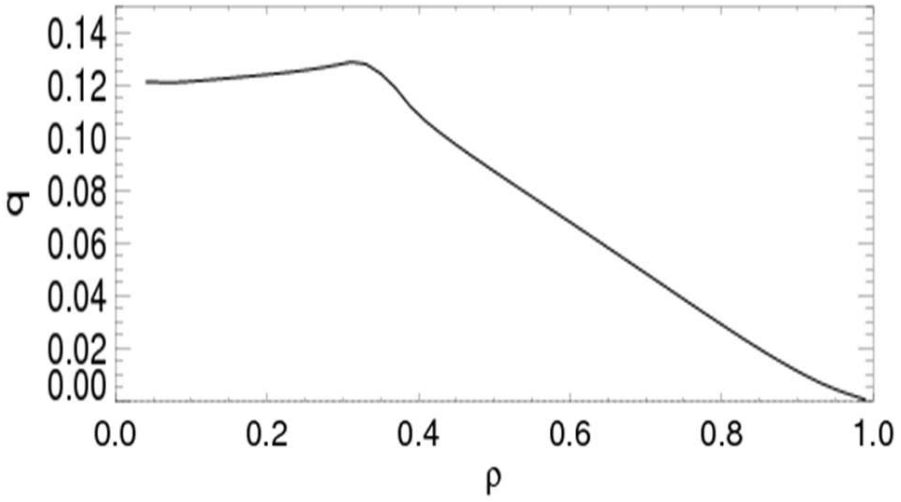

Figure 5.13: Safety factor profile during a SHAx state in RFX-mod.

A further interesting observation is that SHAx states are associated with the presence of a maximum in the q profile, as shown in Fig. 5.13, where the safety factor is plotted against the spatial coordinate in a helical equilibrium, ρ, defined in eq. 3.3.
The absence of magnetic shear at the radius where q is maximum recalls the condition of the reversed shear tokamak plasmas, where the q profile has a minimum and **Reversed Shear Alfvén Eigenmodes** can be excited, as a huge amount of experimental observations demonstrate [117, 97]. In this respect, it must be added that, in tokamaks, the frequency of the RSAE is observed to be

slightly lower than that of the toroidicity-induced AE, somehow consistently with RFX-mod observations.
A last consideration is that in this case the mode would be localized fairly inside the plasma, so that the possibility to measure it by using a probe located at the edge of the plasma column, would deserve a special attention.

5.5 Hints on possible driving mechanisms

The coherent magnetic activity here described has been recognized as the first clear evidence of Alfvén Eigenmodes in the RFX-mod plasma. In this section, a discussion about the drive mechanism for these modes is carried out.
Currently, the common interpretation about the excitation of AE in tokamaks is that they are driven by fast ions, produced by NBI or ICRH antennas, with velocities in the range of the Alfvén speed through the inverse Landau damping mechanism. Nevertheless, AE have been also observed in ohmically heated plasmas (e.g. in ASDEX Upgrade [118], in TFTR [104], in TCA, figure 3 of [119]). For the RFP case, where only ohmic heating is present, a first hypothesis was proposed by Regnoli *et al.* [102]. Toroidal Alfvén eigenmodes could tap free energy from particle source via the diamagnetic drift if

$$\omega_{DRIFT} = \frac{k_\perp}{eB}\frac{1}{n_e}\nabla(n_e\kappa_B T_e) \geq \omega_{TAE}, \tag{5.7}$$

This condition can be satisfied at the edge, where the pressure gradients are the highest, for the high toroidal mode number TAE there detected.
In EXTRAP T2R experiment, indeed, the observed high frequency Alfvénic fluctuation has a toroidal phase velocity of $v_{ph} = \omega_{TAE}R/n$. For coupling, the frequencies and toroidal phase velocities should be equal for the two waves, which yields a relation between n and $k_\perp$,

$$\frac{n}{R} = k_\perp \frac{B_0}{B_\theta} \tag{5.8}$$

and gives $k_\perp \approx k_\varphi$ at the edge as $B_\theta(a) \approx B_0$. It can be verified that the modes which are suited to be destabilized by the electron pressure profile at the edge of EXTRAP T2R are high-n modes with $\mid n \mid \geqslant 30$ consistently with the high-n numbers observed in the experiment.
However, such an interpretation seems not to be applicable to the low-n mode structure associated to the modes observed in RFX-mod.
The $\omega_{DRIFT} \geq \omega_{TAE}$ condition is, moreover, almost never satisfied in tokamaks, where the main magnetic field is higher, so that Maraschek *et al.* [118]

proposed the role of the inverse energy cascade on the coupled drift Alfvén small-scale turbulence to explain the observation of AE in ohmically heated tokamak plasmas.
It is worth mentioning that such a coupling has recently been identified in the edge region of the RFX-mod plasmas in the form of drift Alfvén vortex structures [120], so that a role played by the inverse cascade also for RFX-mod plasmas cannot be excluded.
A "thermal", non-resonant driving mechanism, based on charge exchange processes near the plasma edge, has also been proposed by Chang *et al.* (1995) [104]: the model features, in addition, the mode amplitude enhancement when the edge density increases, as experimentally observed also for AE in RFX-mod.

Anyway, an important role in the excitation of AE in RFX-mod plasma could be played by fast the particles, having a velocity of the order of v_A, which could be generated during the spontaneous reconnection events. It is quite a common knowledge that fast particles (ions) are accelerated during the reconnection process with a velocity comparable to the Alfvén speed, crossways to the current sheet where the magnetic field lines reconnect [8].
Suprathermal ion tails have been observed in the past in RFX plasmas, for which a wave particle interaction model was proposed [121]. Also recently in MST plasmas, a population of suprathermal ions, generated during magnetic reconnection, has been measured [122].
This aspect is presently under investigation by means of the *Neutral Particles Analyzer* diagnostics recently installed in the RFX-mod device (described in Sec. 3.1.3). In figure 5.14a, a contour plot, obtained by a conditional averaging process over about ten discharges, of the neutral hydrogen atoms H^0 fluxes collected by the NPA during magnetic reconnection events (the green curve represents $q(a)$) is shown. In particular, the generation of a high energy ions population in the distribution function of the H^0 exiting the plasma is observed. Picture 5.14b highlights this behaviour: at reconnection, the lowest energy flux component (black line) is reduced, while a high energy ($> 5\,keV$) population forms (red line). The origin of the generation of a non-Maxwellian H^0 fast population (deriving from charge-exchange processes with accelerated protons), is still under debate, but it is worth noting that such fast particles, being in some cases super-Alfvénic, could, in principle, be able to induce an inverse Landau damping mechanism for AE destabilization.
In this respect, it must be reminded that, as shown in section 5.3.3, reconnection events have been observed not only to have an influence on the mode frequency, but also on their amplitude: the growth of AE energy, above the

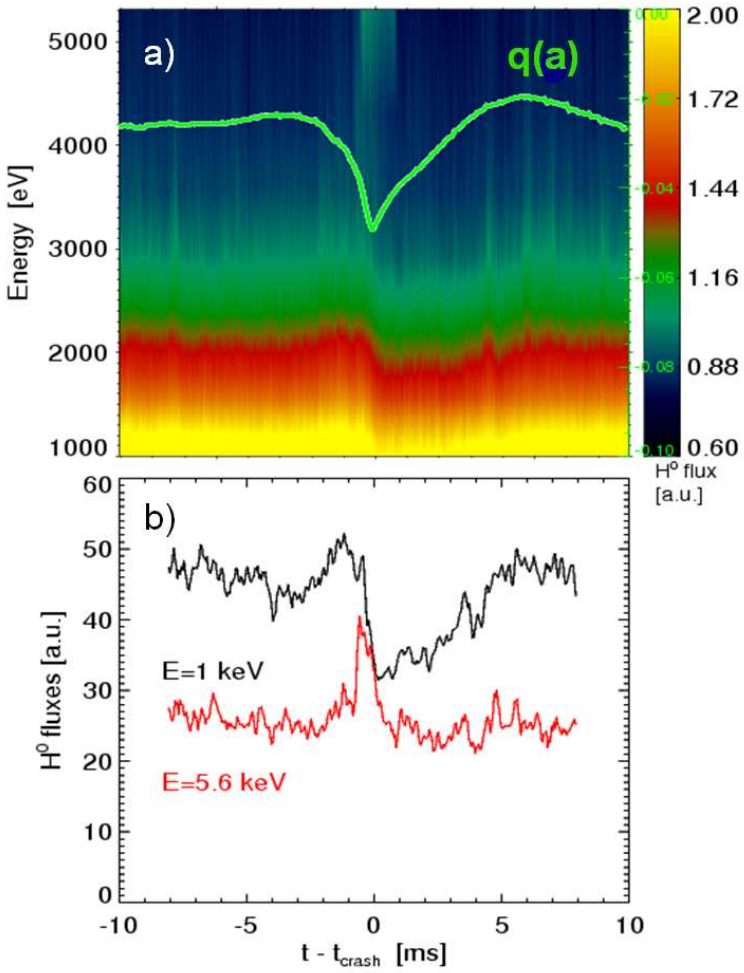

Figure 5.14: a) Event-averaged energy spectrum of the H^0 flux exiting the plasma versus the time rescaled to the DRE minimum time: the generation of a high energy tail is observed. b) Time trace of the H^0 fluxes at low ($E = 1\,keV$) and high ($E = 5.6\,keV$) energy values.

turbulent background, indicates that reconnection is likely to stimulate a driving mechanism for this kind of magnetic instability. Further analysis and experimental investigation of the neutral fluxes at higher energy levels, along with theoretical modelling, would be, however, mandatory in order to support this hypothesis and to investigate the relation of such phenomenon with the ion heating due to reconnection observed in the RFP plasmas of the MST device [123].
Concluding, a last consideration on this subject can be added. At the end of section 5.3.3 is mentioned that it cannot be excluded the possibility that the

growth of the background fluctuation and of the AE amplitude is caused by the same drive, since they both doubled at the reconnection. During the DRE, a strong slap of magnetic energy is distributed at all frequencies: we wonder whether this could be enough to excite AE at the frequencies at which a gap is present.

Microtearing modes

6.1 Microtearing mode introduction

The MHD model provides a description of plasma instabilities in the large length scale approximation. Calculations including finite Larmor radius and kinetic dissipation effects indicate that a class of instabilities with wavelengths comparable to the ion/electron Larmor radius, can occur. They are named **microinstabilities**.
The **microtearing** (MT) modes are microinstabilities that attracted the interest of the tokamak community since the 1970s [124], as they are considered an alternate source of magnetic fluctuations which could enhance thermal transport.
As the name suggests, microtearing instabilities are similar to the more common tearing modes, briefly presented in section 1.4.3, but they are characterized by a high poloidal mode number m and, consequently, very high toroidal mode number n. For such short wavelenght instability, the standard tearing mode theory predicts stability. Nevertheless, microtearing instabilities can be driven unstable by the electron temperature gradient, unlike their long-wavelength counterpart which is essentially current driven [11]. The strong temperature gradients, indeed, can be reservoirs of large amounts of free energy available to trigger microinstabilities, whose effect is to increase radial transport and to damp a further increase of the gradients by a self-regulating process. The physical contribution made by steep gradients is to generate turbulence that short-circuit regions of plasma having different temperatures, generating a heat flux.
RFP plasmas, more than tokamak ones, are an optimal environment for MT modes to grow, since they are characterized by not low collisionality and β plasmas, conditions favourable to destabilize MT [125].
These instabilities have been recently predicted to be linearly unstable in RFX-mod plasma by means of a gyrokinetic code by I. Predebon *et al.* (2010) [126].

6.2 Experimental observations

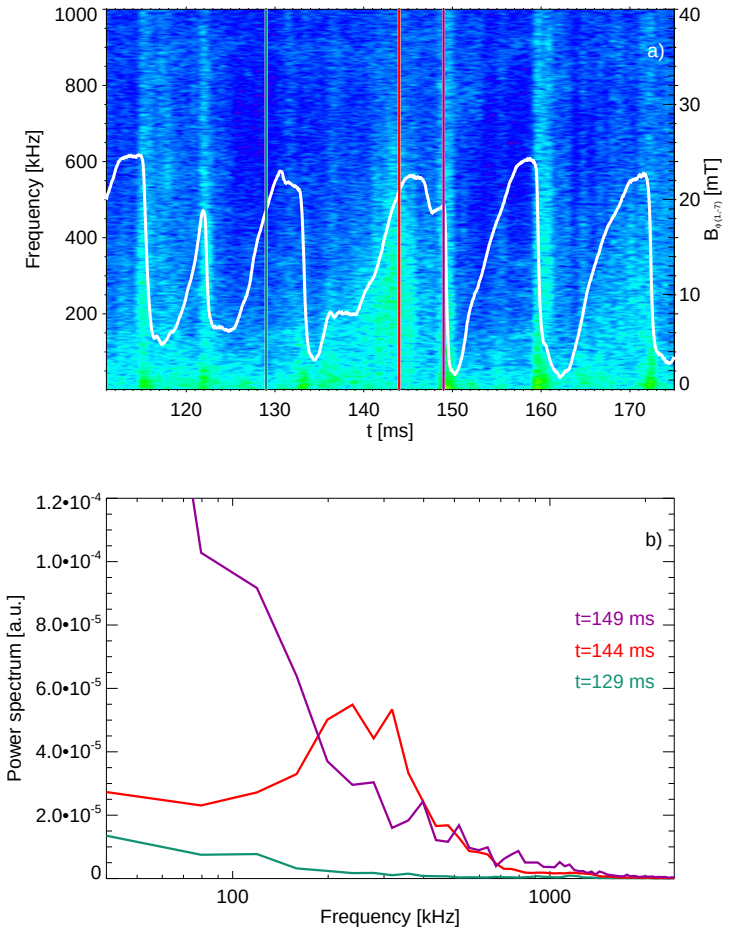

Figure 6.1: a) U-probe $\dot{B}_\theta$ spectrogram: a coherent magnetic activity is observed at $200 \div 300\,kHz$ around $144\,ms$. The white line represents the dominant mode amplitude. (b) Power spectra referring to the time instants indicated: $129\,ms$ (pine green curve), $144\,ms$ (red curve) and $149\,ms$ (violet curve).

In figure 6.1a, a spectrogram of $\dot{B}_\theta$ signal in a high plasma current discharge is shown. A magnetic activity, characterized by a broad frequency spectrum, is clearly visible in the time range between $141 \div 146\,ms$, at a frequency of

$200 \div 300\,kHz$. (It is worth noting that some Type II AE are also slightly visible at 132 and $157\,ms$).
The activity has been observed only in discharges characterized by long lasting QSH states, which, for RFX-mod corresponds to high plasma current levels and shallow reversal parameter. The white line, representing the amplitude of the dominant mode magnetic field, is overplotted to underline that the mode under investigation occurs in coincidence of the phases during which the $B_{\varphi\,(1,-7)}$ amplitude is relatively high.
Moreover, as seen in section 5.3.3, a global enhancement of the magnetic fluctuations at all the frequencies is seen to occur during discrete reconnection events: in the spectrogram, they are recognized by the narrow vertical stripes in correspondance of the fall of the dominant mode (for a reminder of the connection between DRE and the transition to MH states, see section 2.2.2)
In figure 6.1b three power spectra realized at the three time instants indicated in the spectrogram are shown. In particular, the pine green power spectrum has been calculated at $129\,ms$, that is when the dominant mode amplitude is high, but the magnetic activity under investigation is not observed. The red curve, referring to $144\,ms$, corresponds to an instant at which the $B_{\varphi(1,-7)}$ is high and the activity is present. Finally, the violet curve shows the magnetic spectrum at $149\,ms$, that is during a discrete reconnection event.
The comparison of the spectra is useful, on the one hand, to show the appearance in the red curve of a pronounced broad peak centered around $200\,kHz$, while in the green spectrum, although the dominant mode is high, the activity does not occur; thus the presence of a QSH state is observed to be necessary but not a sufficient condition for the mode to develop.
On the other hand, the spectra in picture 6.1b help to understand how to distinguish the mode spectrum (red curve) from that due to a reconnenction event (violet curve), since the two spectra are comparable at the frequencies at which the activity under investigation occur. Nevertheless, they exhibit a marked difference at the lowest frequencies. For this reason, in order to give a quantitative evaluation of the spectrum amplitude A of the activity without confusing it with the DRE occurrence, the following formula has been applied:

$$A = \frac{\int_{\Delta f_1} S(f)df}{\int_{\Delta f_2} S(f)df} \tag{6.1}$$

that is the integral of the power spectrum in the frequency range $\Delta f_1 = 100 \div 300\,kHz$, indicative of the presence of the modes, normalized with respect to the respective low frequency spectrum integral, in the range $\Delta f_2 = 10 \div 50\,kHz$.

As mentioned, the occurrence of QSH states is found to be not the only ingredient necessary for the development of the fluctuation under study.

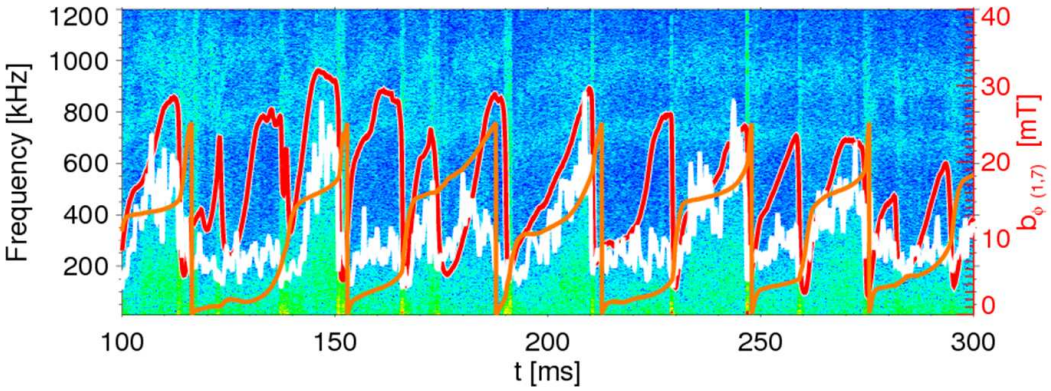

Figure 6.2: U-probe $\dot{B}_\theta$ spectrogram: the amplitude A of the activity under investigation (white curve), the amplitude (red curve) and the phase (orange curve) of the dominant mode are superimposed.

An important role is actually played by the phase of the dominant mode itself, since it has been experienced to rotate at a frequency of about $30\,Hz$.
This statement ensues from the observation of figure 6.2 (the two coherent at 800 and $1000\,kHz$ are the modes described in Chapter 5 and recognized as Global Alfvén Eigenmodes). The time behaviour of the magnetic activity observed to peak around $200\,kHz$ in the spectrogram of the $\dot{B}_\theta$ U-probe signal, is well described by the amplitude A, defined by the relation 6.1, represented by the white curve. Moreover, the amplitude (red curve) and the phase (orange curve) of the dominant mode are superimposed, in order to investigate their role on the appearance of the activity. In particular, it can be observed that the amplitude A increases when the dominant mode amplitude is high and, at the same time, the phase value is roughly between π and 2π.

In order to study the relation between the activity amplitude and the phase of the dominant mode, $\phi_{(1,-7)}$, a statistical analysis performed over about 30 high-current discharges has been carried out. Since the quantities A and $\phi_{(1,-7)}$ are both functions of time, they have been divided in time intervals of some ms and an average value for each time interval of the two quantities has been considered. The points plotted in figure 6.3a, thus, show the relation between the amplitude A and the phase $\phi_{(1,-7)}$.
It is clear from the figure that high activity amplitudes are associated to specific phase values included in the range $\Delta\phi = (0.9 \div 1.7)\pi$ (points highlighted by red colour).
A parallel analysis is represented in figure 6.3b, where the points have been selected distinguishing the cases when the phase belongs to $\Delta\phi$ (red points) and those with a different phase (black points). It can be observed that if the phase

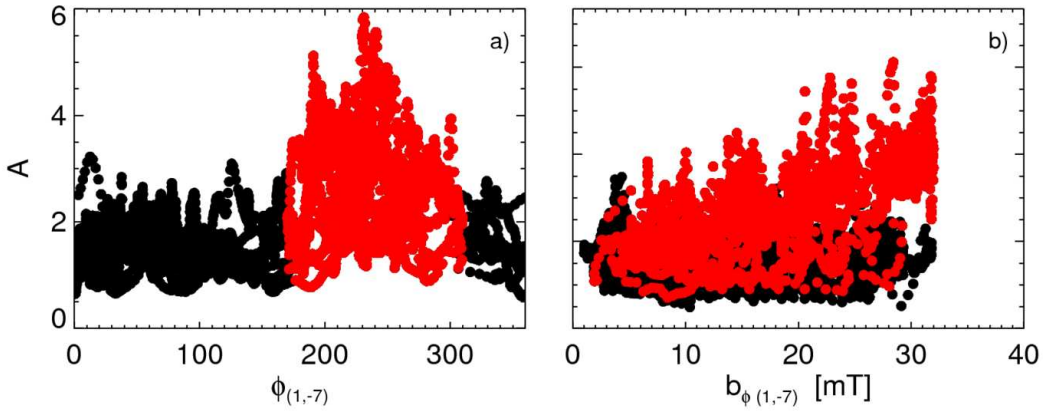

Figure 6.3: a) The activity amplitude A is shown to be high only within a certain range of the dominant mode phase values. The "right" phase is highlighted by the red points. b) The amplitude A of the modes with "right" phase increases with the amplitude of the dominant mode.

is the "right" one (the red points), the amplitude A depends (roughly linearly) on the amplitude of the dominant mode $B_{\varphi(1,-7)}$. On the contrary, if the phase is not included in the $\Delta\phi$ range, A mantains a constant low value both during MH and QSH states. We can conclude that **the magnetic activity under investigation is observed by the U-probe in conditions of high $B_{\varphi(1,-7)}$ (corresponding to QSH states) and at specific phase values.**

Moreover, the analysis of the activity amplitude A has been extended to the data coming from two magnetic coils belonging to a poloidal array of the ISIS system measuring $\dot{B}_\theta$. In particular, the mentioned array is located at the toroidal angle $\varphi = 216.2°$, so, pratically, at the same toroidal position of the U-probe. The two coils used for the analysis has been chosen to be located near the equator, one on the outer side (at $\Theta_e = 19°$), the other on the inner side (at $\Theta_i = 161°$) of the machine. In figure 6.4a the time evolution of the amplitude A measured by the U-probe (orange curve), by the outer ISIS coil (red curve) and by the inner ISIS coil (blue curve) are plotted. The black curve refers to the dominant mode amplitude.
From the picture, it can be noted that, as above mentioned, the presence of QSH state (high $B_{\varphi(1,-7)}$ amplitude) is a condition necessary but not sufficient to observe high values of the activitity amplitude A measured by the three different magnetic sensors. Moreover, a very good agreement between the orange and the red curves that are quite close, while the blue curve, coming from a probe diametrically opposed located, is clearly in antiphase with respect to them. These observations suggest that the magnetic activity under study is

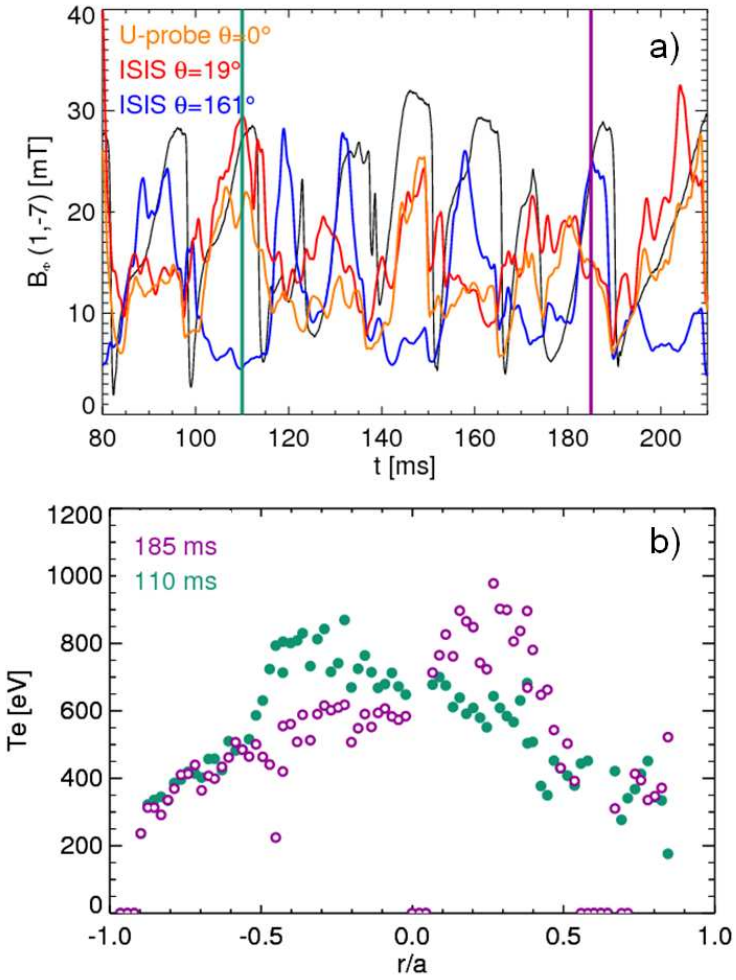

Figure 6.4: (a) Amplitude A of the modes plotted as measured by the U-probe (orange curve) and by the ISIS sensors located at the internal (orange) and external (red curve) sides. The black curve represents the dominant mode amplitude. (b) Electron temperature profiles measured by the Thomson scattering diagnostics at the time $110\,ms$ (pine green symbols) and $185\,ms$ (violet symbols), as indicated in (a).

alternately present on one side of the machine or on the other.
Futhermore, it has been observed that the amplitude A is high during QSH states associated to the presence of a thermal structure i.e. a steep temperature gradient, in correspondence with the coil used for the measurement. In figure 6.4b, the electron temperature profiles measured by the Thomson scattering diagnostics (see section 3.1.3) captured at $110\,ms$ (pine green symbols)

and at $185\,ms$ (violet symbols) are plotted as examples. A thermal structure typical of QSH states (see Sec. 2.2.2) is observed to be present in each of the two profiles. The hot region is observed to change its position in time in accordance with the rotation of the helical structure measured by means of the phase of the dominant mode. In particular, a relation is found between the appearance of the magnetic activity on the outer side of the machine (orange and red curves of fig. 6.4a) and the presence of a thermal structure in the internal side, corresponding to negative r (pine green symbols in fig. 6.4b). On the other hand, the maximum activity on the inner side (blue curve) is associated to a thermal structure arising on the external side of the machine (violet symbols), at positive r values.

In order to better understand the geometry of the experimental setup, figure 6.5, which comes from a simulation of the flux surfaces during a SHAx state, shows a fraction of helical structure and the respective position of the magnetic coils and of the Thomson diagnostics at $t = 185\,ms$ referring to the case considered in fig. 6.4.

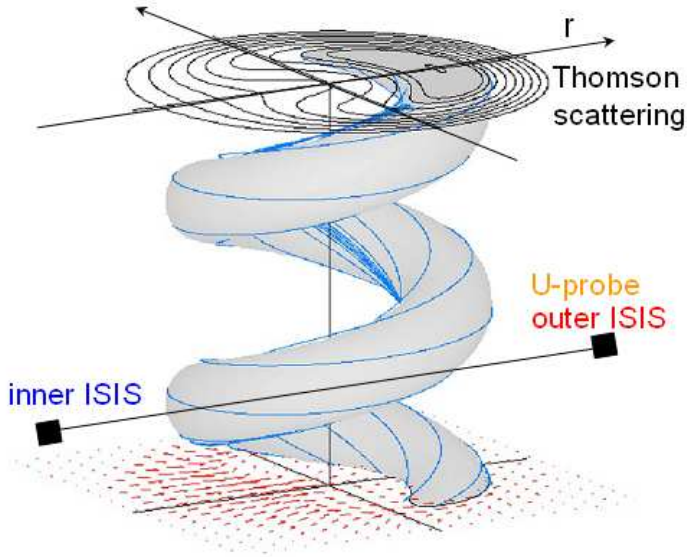

Figure 6.5: Schematic view of the helical structure and the relative position of the magnetic probes (represented by the small cubes) and of the Thomson scattering (in the scheme the two groups of diagnostics are only 1.5 pitches, instead of the 2.5 that should be).

The relation between the thermal structure and the high magnetic activity can, thus, be explained first of all recalling the cyclical structure of the helix

and presuming that its general features are almost spatially preserved. In this way, it turned out that the activity seems to rotate with the helical structure, since it can be observed only when the convex side of the helix passes in front of the probe. This can be verified considering that the helical pitch is $p_h = 360°/7 \approx 51.4°$ and the magnetic coils are $\Delta_\varphi \approx 135°$ apart from the Thomson scattering diagnostics, thus the helical structure takes two turns and a half to cover the distance between the two diagnostics. This implies that the external magnetic probes face a plasma configuration similar to that crossed by the lines of sight located on the inner side of the chamber and vice versa.
From this analysis it can be concluded that **the magnetic activity under investigation is observed to be localized on the convex side of the helical structure characterizing the RFX-mod plasmas during QSH states. It is worth noting that the appearance of the activity is associated to the presence of strong temperature gradients.** Anyway, up to now it is not clear whether the modes occur only on the convex side of the helical structure or whether they are located all along the boundary of the helix, but the edge sensors cannot measure the magnetic fluctuations belonging to the inner side of the helical structure since they are probably too far for the probes themselves. Further investigations, involving discharges specifically characterized by SHAx states, i.e magnetic configurations where the helical structure is large (see fig. 2.10), could give an answer to this point.

6.2.1 Mode number measurements

An essential information in order to try to interpret the magnetic activity under study is the measurement of the poloidal and toroidal mode numbers.
The poloidal mode number m has been deduced by means of two coils located in the two cases of the U-probe. The figure 6.6a shows the $S(m, f)$ spectrum obtained by applying the two-point technique in a phase of a single discharge characterized by a strong activity in the frequency range under consideration. The activity is recognizable at $300\,kHz$ and is actually slightly affected by spatial aliasing. The mentioned figure is shown as an example, since a large range of values has been measured: $m \approx 13 \div 23$.
A measurement of the toroidal mode number is exhibited in figure 6.6b. It has been obtained using two of the coils installed on the GPI diagnostics, since the U-probe one was heavily affected by spatial aliasing. The n value results, in fact, to be very high, at the order of hundreds. In particular, it has been seen to span values in the range $100 \div 300$.

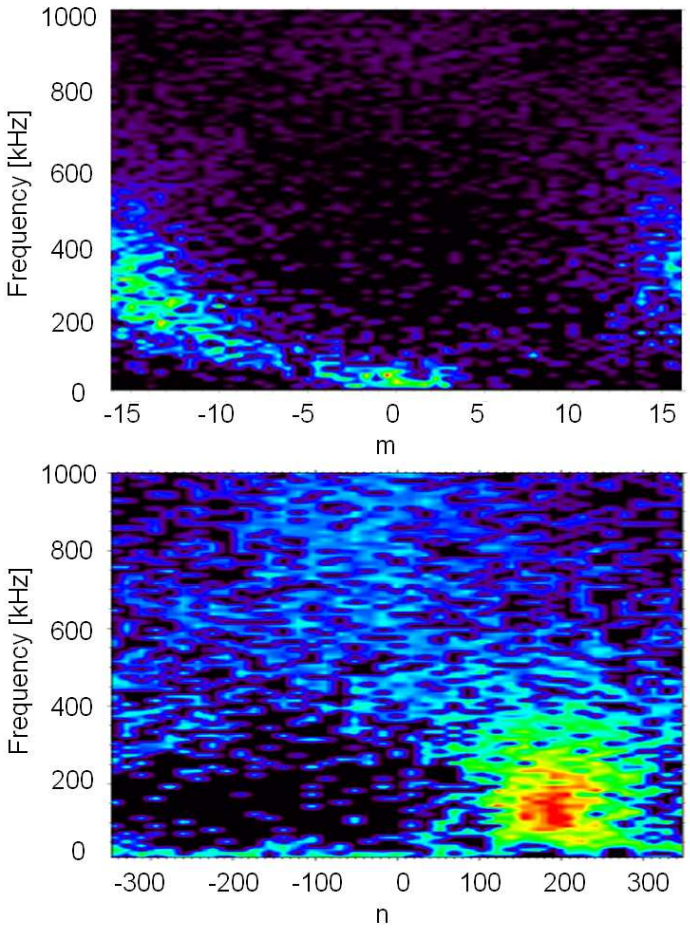

Figure 6.6: a) $S(m, f)$ spectrum obtained rotating the U-probe. b) $S(n, f)$ spectrum obtained by using GPI coils.

6.2.2 Amplitude A as a function of the parameter β

A further interesting observation is the clear relation between the amplitude A of the modes under study and the parameter β, shown in figure 6.7.
Each point has been obtained selecting time intervals characterized by QSH states (i.e. dominant mode high values) and the so-called "right" phase.
The picture shows that the amplitude of the magnetic activity clearly grows with the β parameter.

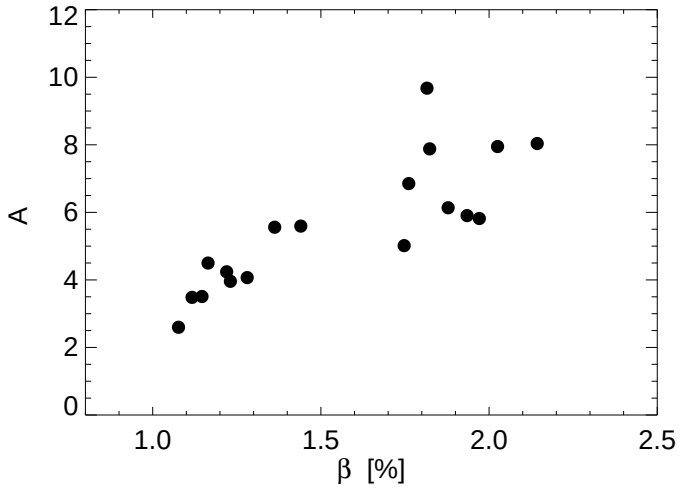

Figure 6.7: Activity amplitude A plotted against the relative β values.

6.3 Possible physical interpretation

The magnetic activity arising in the $\dot{B}_\theta$ spectrum at $\approx 200\,kHz$ is found to be characterized by spectral properties in good agreement with some features characterizing microtearing instabilities, as theoretically predicted by gyrokinetic codes: in particular, the connection with strong temperature gradients (achieved in RFX-mod plasma during QSH states), the high poloidal and toroidal mode numbers and the correlation between the amplitude of the modes and the β parameter.
More in detail, the high mode numbers measured suggest that we are dealing with a microinstability. Moreover, the formation of Internal Transport Barriers (ITB) enclosing the high temperature core in QSH states, observed in RFX-mod experiments [127], leading to the formation of high temperature gradients, can supply the free energy necessary to trigger microinstabilities as MT, enhancing energy transport.
Furthermore, an interesting point concerns the frequency of the modes. Microtearing instabilities are expected to be characterized by a phase velocity close to the electron diamagnetic velocity,

$$v_{de} = \frac{\nabla p \times \mathbf{B}}{e n_e B^2}. \tag{6.2}$$

The electron diamagnetic velocity in the region of the temperature gradient in RFX-mod plasmas can be evaluated as:

$$v_{de} \approx \nabla T_e/B \approx 5000\, eV m^{-1}/0.5\, T \approx 10^4\, ms^{-1}. \tag{6.3}$$

where the density gradient has been neglected, since it can be generally considered small with respect to the temperature one at that radius. On the other hand, the experimental activity is observed at a typical frequency value of $200kHz$; so the toroidal phase velocity measures

$$v_\phi = (2\pi f)/(n/R) \approx 10^4\, ms^{-1}. \tag{6.4}$$

Based on these considerations, a numerical investigation by means of the gyrokinetic GS2 code [128, 129] has started with the aim of properly interpret the measured activity. The code, modified to include the RFP geometry, is specifically built to find out information about instabilities and turbulence characterized by $k_\perp r_L \approx 1$, $k_\perp/k_\parallel << 1$, $\omega/\omega_c << 1$ It is based on the electromagnetic nonlinear gyrokinetic equation, and it uses as input data profiles coming from RFX-mod experimental measurements.Simulations are, however, linear and the geometry is assumed axisymmetric for simplicity.
These studies show that the dominant instabilities in the RFX-mod ITBs region are predicted to be of microtearing (MT) kind, radially localized around their resonant surface and elongated along the magnetic field direction.
The results of the GS2 code indicate that, in the typical experimental condition met in QSH plasmas, MT are unstable.Moreover, their growth rate rises with the normalized logarithmic temperature gradient, $L/L_{T_e} \equiv -L\nabla T_e/T_e$, (where L is a characteristic length) and with plasma β.

As already mentioned, the first evident similarity between experimental observations and code results is the high values of the periodicities. GS2 provided important information about the poloidal wavenumber m, while the corresponding axial wavenumber n is obtained from the q profile. In figure 6.8, the values theoretically expected for typical RFX-mod discharges, are plotted. The periodicities associated to the modes under investigation are characterized by m values of the order of tens and n values of the order of hundreds, as described in 6.2.1; the values most frequently measured in RFX-mod plasma are represented in the picture by the large red point. Thus, it can be stated that the experimental values are compatible with those expected. The not perfect agreement could be ascribable to the fact that theoretical values are strictly related to the radial extension of the temperature gradient (the peak of the spectrum moves towards larger n values as the gradient is increased) and to the beta parameter; moreover, it must be reminded that while the eigenfunction of MT are extremely radially localized in the region where the gradient is

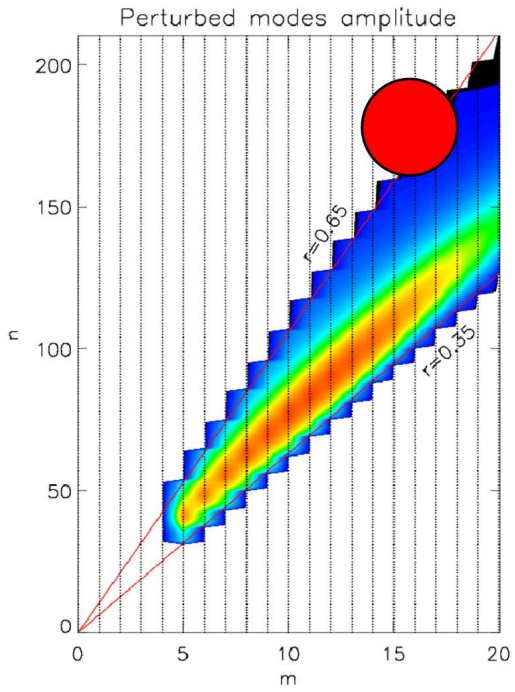

Figure 6.8: Perturbed modes amplitude contour plot in the $m - n$ plane (amplitude is decreasing from red to blue). The red point represents the values of the mode periodicities more frequently observed.

steeper, the experimental measurements are taken at the plasma edge.

The information coming from section 6.2.2, where the clear relation between the activity amplitude and the parameter β [126] is described, matches quite well with what predicted by the code [126], where large β values are seen to be associated to higher growth rates and wavenumbers. In particular, similarly to what above described regarding the resistive interchange modes (Sec. 4.3), in absence of a non-linear estimation of microtearing's saturation amplitude, we can to a first approximation compare theoretical growth rate evaluations with the measured amplitude of the modes (in this case with the estimated A). The same behaviour with respect to the β parameter is found for these two quantities.

Finally, the code has been also specifically ran for some cases in which the magnetic activity described in this chapter has been detected. An example is given in figure 6.9.
The temperature gradient used for the analysis has been evaluated by an inter-

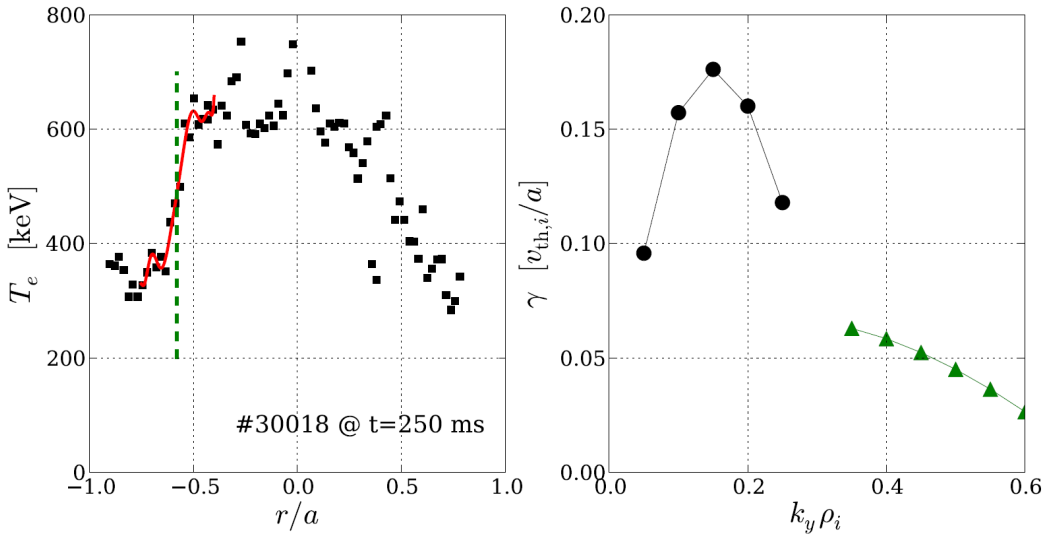

Figure 6.9: a) Electron temperature profile measured by the Thomson scattering diagnostics. The red curve represents an interpolation of the temperature gradient, the green one indicates the radial position chosen for the analysis. b) Growth rates of the instabilities associated to temperature gradients, from GS2 analysis, versus perpendicular periodicities: the black curve refers to microtearing modes, the green one to electrostatic modes.

polation of the electron temperature profile measured by the Thomson scattering diagnostics, as shown by the red curve in fig. 6.9a. In particular the value of the gradient chosen is that at the radial position indicated by the green dashed line. At the same position, the safety factor (for an axisymmetric equilibrium) and the electron density have been evaluated.
The results of the analysis are shownd in fig. 6.9b, where the growth rate of the instabilities is shown as a function of the wavenumber $k_y\rho_i$, where

$$k_y = \frac{n}{R}\sqrt{\left(\frac{r}{R}\right)^2 + q^2} \tag{6.5}$$

is the perpendicular wavenumber, as explained in the paper [130], and ρ_i is the ion Larmor radius. By means of the analysis of the parity of the modes, it has been demonstrated that the branch at higher wavenumber (green curve) refers to an instability having a not yet determinated electrostatic nature, while the branch at lower wavenumber (black curve) to a microtearing instability.
The electrostatic branch has been shown to be very important in corrispondence to strong temperature gradients: further theoretical and experimental analyses are necessary to collect more information about this instability.
Regarding the microtearing instability, the maximum of the growth rate cor-

respond to $n \approx 100$ and, consequently, to $m \approx 10$, in good agreement with experimental observations.

Electrostatic and magnetic measurements in Extrap-T2R

The research activity performed on the EXTRAP T2R Reversed-Field Pinch device (which is described in some detail in section 2.3) was devoted to the study of the plasma edge by means of an insertable probe, the Alfvén probe, provided with different electrostatic pins and with triaxial magnetic coils (see section 3.1.4).
The main feature of the experimental setup is that electrostatic and magnetic measurements can be obtained at different radial positions, since the Alfvén probe can be radially inserted into the plasma up to $r/a = 0.92$.
The experimental campaigns were focused on two main topics. On the one hand, the effect on the edge plasma profiles of externally applied Resonant (RMP) or non-Resonant (nRMP) Magnetic Perturbations, depending on the fact the perturbations are resonant or non-resonant in the plasma column, was investigated. In particular, the effect of RMP on the plasma flow is an interesting matter to delve [53]. For this purpose, different radial scans were performed applying different resonant ($n = -12, -13, -15$) and non-resonant ($n = -9, -8, +5$) magnetic perturbations.
On the other hand, in order to investigate the features of the magnetic activities observed to occur in EXTRAP T2R plasmas, different plasma conditions have been explored. In particular, discharges with plasma current values in the range $I_p = 30 \div 115kA$ and characterized by values of the reversal parameter varying in the range $F = -0.05 \div -0.4$, have been realized.

In figures 7.1a,b the time evolutions of the plasma current I_p and of the reversal parameter F for a typical discharge of EXTRAP T2R are shown. In particular, the plasma current achieves a value of $50kA$ that can be considered relatively low: this choice is made in order to prevent possible damages to the probe. During the discharges realized at higher plasma current, the insertable probe was located at the level of the limiter ($r/a = 1$). Moreover, two signals provided by the electrostatic and magnetic sensors of the Alfvén probe are plotted in figures 7.1c,d, respectively. In particular, the first one shows a

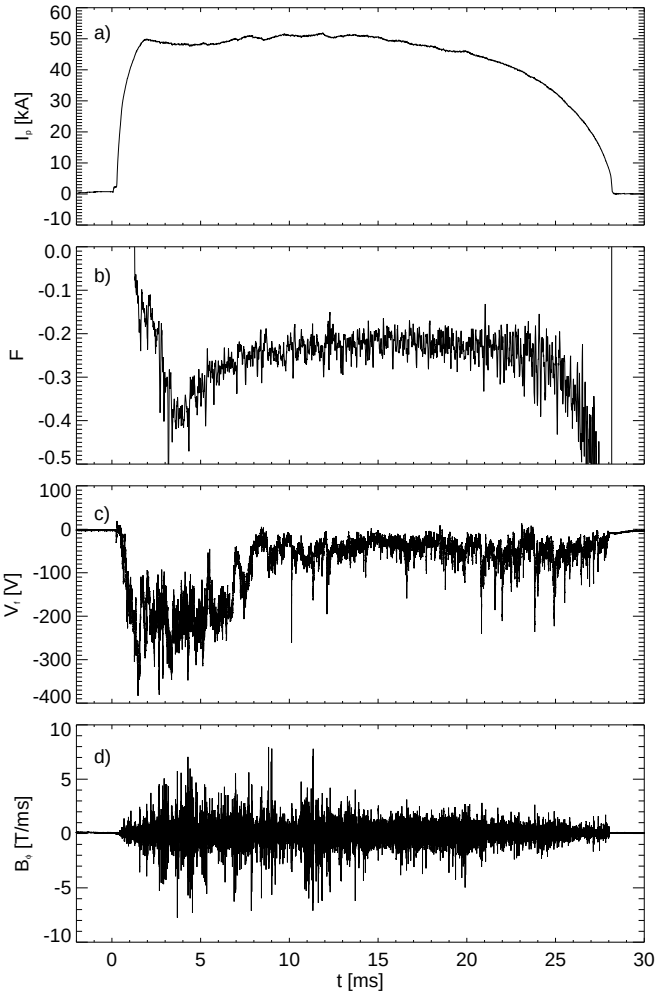

Figure 7.1: Time evolution of plasma current (a), F (b), floating potential (c) and magnetic signal (d) for a typical EXTRAP T2R discharge.

floating potential signal, while the second one represents a measurement of the time derivative of the toroidal magnetic field component.

7.1 Electrostatic measurements

As exposed in section 3.1.4, the Alfvén probe is equipped with a combination of electrostatic pins in a balanced-triple Langmuir probe configuration and with electrostatic sensors measuring the floating potential.

By inserting the probe inside the plasma, the floating potential, electron temperature and electron density radial profiles at the edge can in principle be measured (see Sec. 3.1.4 again).

7.1.1 Floating potential profile

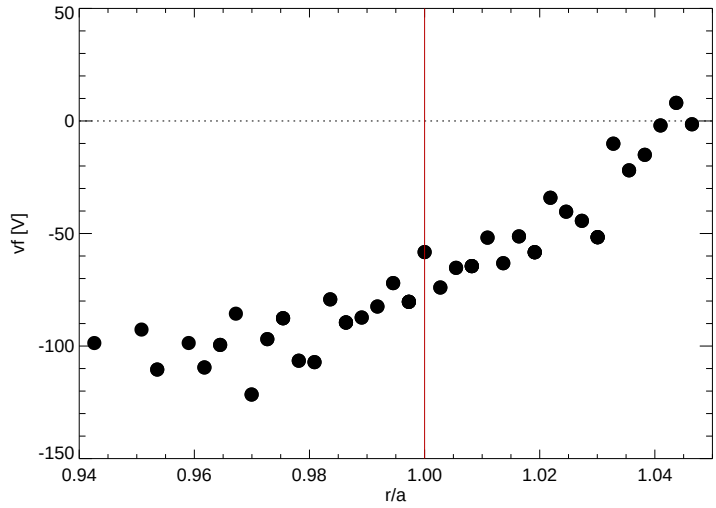

Figure 7.2: Floating potential profile measured by Alfvén probe.

The floating potential profile exhibited in figure 7.2 has been obtained by using the data from all the floating pins of the Alfvén probe for a whole radial scan. In this way, measurements obtained at different radial positions have been obtained. The resulting curve gives a reasonable idea of the floating potential profile at the edge of EXTRAP T2R plasma.

In figure 7.3 different floating potential profiles are plotted. In particular, during the experimental campaign different radial scans have been performed by means of the insertable probe for a set of discharges for which external perturbations (RMP and nRMP) have been applied. The legend indicates the toroidal mode number values of the perturbations applied to each profile. The amplitude of both resonant and non-resonant perturbations has been setted on $0.4\,mT$. The profile realized with discharges performed without any perturbation (red curve) is plotted for comparison.
From these preliminary results, it is not possible to recognize any particular relation between the perturbations and the relative profile. An exception may

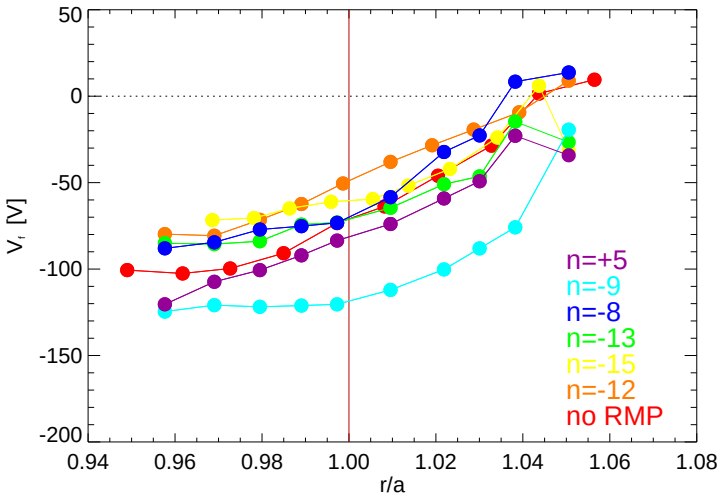

Figure 7.3: Floating potential edge profiles performed during the application of RMP or nRMP.

be the RMP $n = -9$, that exhibits a V_f profile more negative than the other ones, but the reason and the possible consequences are not clear.

7.1.2 Electron density and temperature profiles

By means of the balanced triple-probe located on the Alfvén probe, it has been possible to measure the electron temperature and density profiles (a brief introduction on the measurement technique is given in 3.1.4), as shown in figures 7.4a,b respectively.

The temperature profile is rather different from that expected: it does not decrease at the edge, on the contrary it increases; moreover, the values ($T_e \gtrsim 80\,eV$) are somewhat high, since a temperature of about $20\,eV$ has been measured at the level of the limiter in previous experimental campaigns [131]. The cause can be related to the presence of suprathermal tails on the distribution function of the electrons. As mentioned in the part of section 3.1.4 devoted to the electrostatic sensors, the theory of the triple probe applied in order to evaluate the temperature values assumes a maxwellian distribution function. The occurrence of suprathermal electrons can thus invalidate the measurement.
On the other hand, the density profile results to be reasonable.

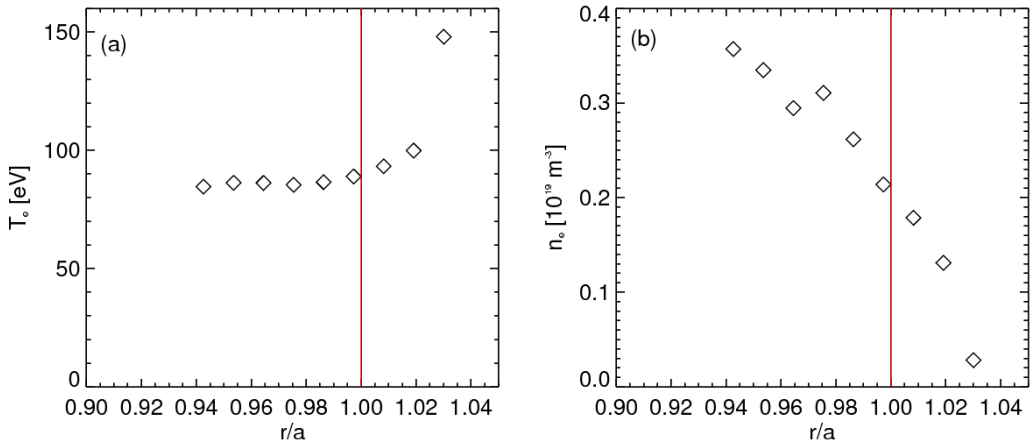

Figure 7.4: Electron temperature (a) and density (b) profiles at the edge of EXTRAP T2R plasma measured by means of a radial scan of the triple-probe housed on the Alfvén probe.

7.2 Magnetic measurements

The magnetic measurements obtained by the two triaxial coils located into the Alfvén probe show various interesting magnetic activities to occur on EXTRAP T2R plasma edge.
Preliminary analyses are presented in the following.

7.2.1 High frequency activities

In figure 7.5a, the frequency spectra relative to the working magnetic signals obtained by the Alfvén coils for a typical EXTRAP T2R discharge, are shown. Similarly to what observed in the RFX-mod spectra (e.g. Fig. 3.2), the toroidal and radial components of the fluctuating magnetic field are one order of magnitude higher than the poloidal one, since they are the components perpendicular to the main one, that, in the edge region of a RFP configuration the poloidal component.
An imposing peak at a frequency around $2\,MHz$ is exhibited by all signals, althought in the poloidal component it is more evident. Moreover, a zoom of the peak (Fig. 7.5/b) highlights the occurence of a fine structure, characterized by the presence of close peaks, about $200\,kHz$ apart from each other.
Preliminary considerations on the possible physical interpretation of these modes reveal that the order of magnitude of the shear Alfvén continuum fre-

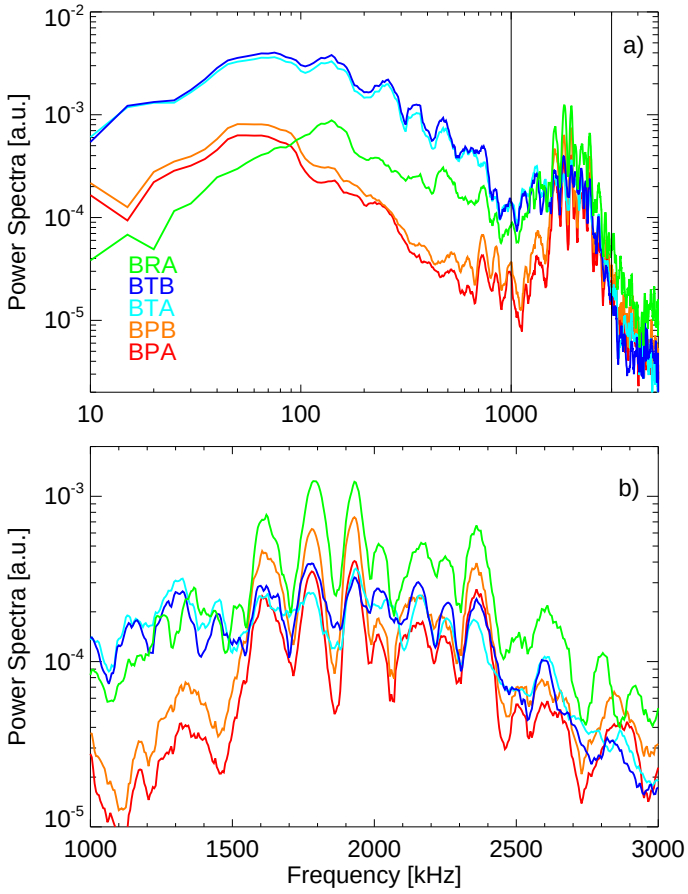

Figure 7.5: (a) Frequency spectra of the Alfvén probe magnetic signals. A peak at $2\,MHz$ is observed to arise: a zoom (b) shows the fine structure of the activity.

quency expected for EXTRAP T2R discharges with these plasma conditions ($v_A \approx 700\,km/s$) is evaluated at the edge as

$$f_A \approx \frac{1}{2\pi}\frac{m}{a}v_A \approx m \cdot 600\,kHz, \tag{7.1}$$

depending on the poloidal mode number, m. Furthermore, it can be added that the activity under investigation is observed at a frequency higher than the cyclotron frequency relative to Hydrogen ions, extimated as $\omega_c \approx 800\,kHz$.

Thus, in case this activity will reveal an alfvénic nature, it must be take into account that only the compressional branch, characterized by the dispersion relation $\omega = kv_A$, can develop at frequencies higher than the cyclotronic one. On the other hand, an experimental relation between the mode frequency and the Alfvén velocity is not easy to find out since the plasma current and the electron density values result in general to be linearly dependent one to the other in EXTRAP T2R .
Nevertheless, it is possible to recognize that, although the order of magnitude of f_A with a large enough wavenumber k is comparable to that of the modes observed, their general behaviour is rather different from that of the Alfvén eigenmodes recognized to occur in RFX-mod plasmas (Chapter 5). For instance, they are not present for whole the discharge time duration, but are characterized by a burst appearence of some ms. This is clear by observing the spectrogram in figure 7.6a, where the magnetic activity described appears more evident around $12 - 13\,ms$, characterized by a rather broad frequency spectrum.
An evaluation of the toroidal mode number relative to this fluctuation has beeen realized by appling the two-point technique between the two toroidally spaced coils of the Alfvén probe. In figure 7.6b, the $S(n, f)$ spectrum relative to the time interval included by the two black lines in fig. 7.6a, is shown. The activity is recognized at about $2000\,kHz$ and exhibits long wavelength.

7.2.2 Low frequency activities

A clear magnetic activity at a frequency of about $60\,kHz$ and enduring for the whole discharge time is observed to occur in the frequency spectrogram of the poloidal component of the fluctuating magnetic field measured by the insertable Alfvén probe, shown in fig. 7.7a. Tearing modes in EXTRAP T2R plasma are known to rotate rather fast with the plasma flow at frequencies of the order of some tens of kHz. Thus, the observed activity could probably be interpreted in terms of *tearing modes*.
Moreover, in the EXTRAP T2R device the dominant tearing mode during QSH discharge is $(m, n) = (1, -12)$ [132]. We may expect that during MH states the spectrum of the tearing modes would be rather broad, but centered around the dominant mode (for a comparison, see figure 2.8, relative to RFX-mod). In figure 7.7b, the $S(n, f)$ spectrum relative to the time interval included between the black lines in fig. 7.7a, is shown. At frequencies lower than $100\,kHz$ a magnetic structure is measured, characterized by mode number values in the interval $n = -20 \div 0$. It is worth noting that the measurement is roughly consistent with the values expected.

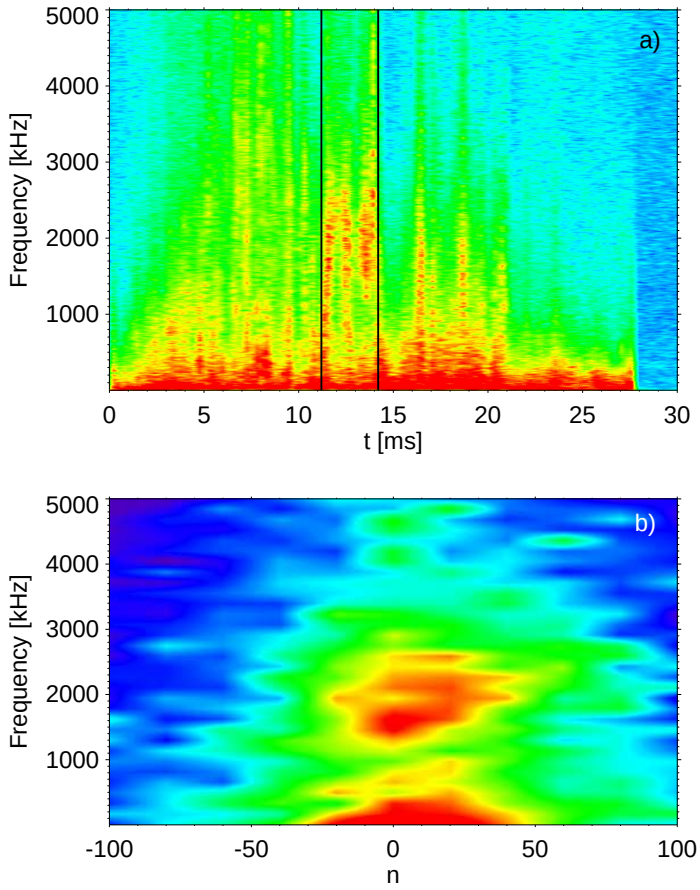

Figure 7.6: (a) Spectrogram of the poloidal component of the Alfvén probe magnetic signal. (b) $S(n, f)$ spectrum of the poloidal component: the peak is visible at $2\,MHz$.

The same activity is also slightly visible in the spectrogram of the toroidal component (Fig. 7.8/a), but the presence of fluctuations of the same amplitude at higher frequencies, whose origin is not clear yet, somehow flattening the frequency spectrum, makes these modes less distinguishable.
Moreover, it is worth noting that the $S(n, f)$ spectrum realized during the flat top phase of the discharge ($10 \div 20\,ms$) and shown in figure 7.8b, exhibits the

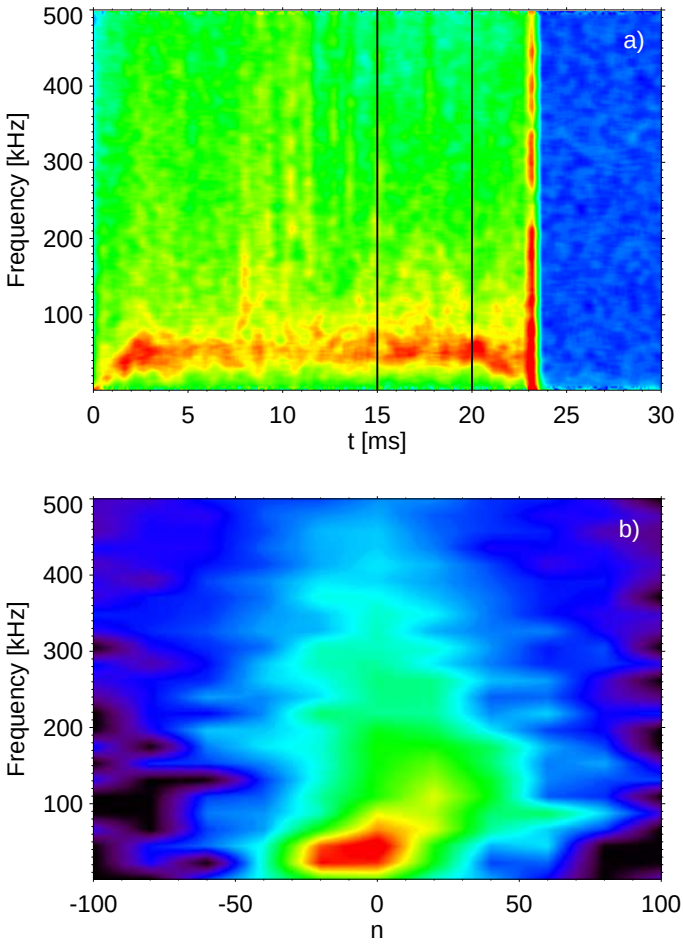

Figure 7.7: Low frequency spectrogram (a) and $S(n, f)$ spectrum (b) of the poloidal fluctuating magnetic field measured by the Alfvén probe.

same magnetic structure observed in the fluctuation of the poloidal magnetic field component at negative wavenumbers (see fig. 7.7b) and an additional activity at higher frequency, associated to high positive n values ($n \approx 30$).

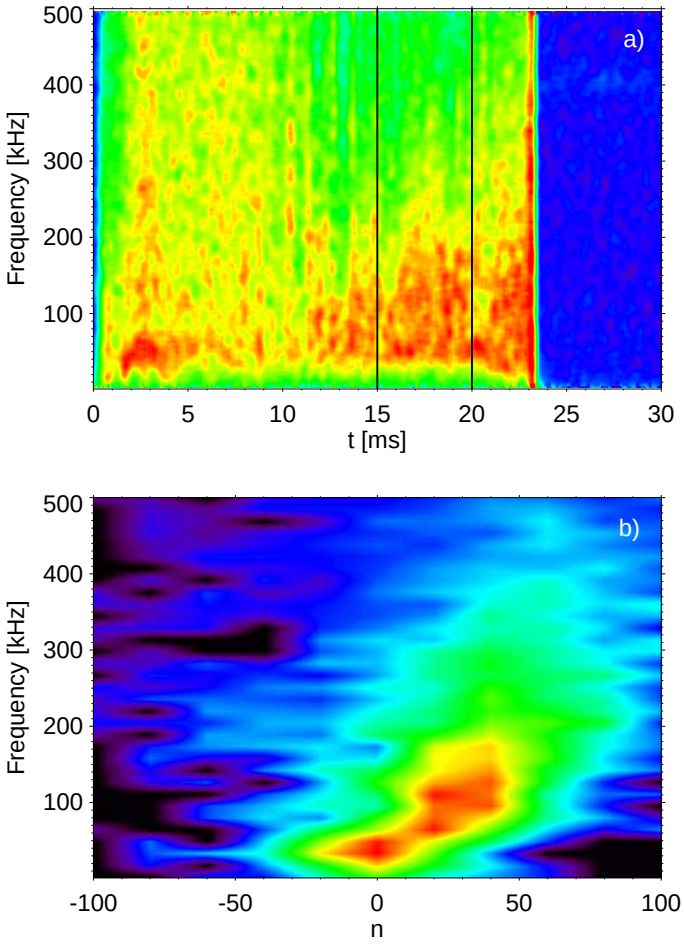

Figure 7.8: Low frequency spectrogram (a) and $S(n, f)$ spectrum (b) of the toroidal fluctuating magnetic field measured by the Alfvén probe.

Conclusions

In this thesis a study of magnetic fluctuations, aimed at the understanding the nature of the instabilities occurring in Reversed-Field Pinch plasmas, has been presented. In particular, the magnetic (and, in part, electrostatic) activities, measured by means of in-vessel probes, observed to develop in two fusion plasma experiments, RFX-mod and EXTRAP T2R , are described.

The magnetic activities observed in the RFX-mod plasma have been extensively analyzed, focusing on the study of their temporal and spatial periodicities in different plasma conditions. Thus, their experimental dispersion relations have been determined, in order to proceed with a comparison with the predictions of theoretical models for plasma dynamics.
In particular, the study presented in this thesis consists in the first detection and physical characterization of the magnetic instabilities occurring in RFX-mod plasmas. Three main branches of magnetic activities have been recognized: the foremost results and the relative open issues are summarized in the following.

Resistive Interchange Modes. A quasi-coherent magnetic activity arising at frequencies centered around $100\,kHz$, has been observed to cover an important fraction of the total magnetic fluctuating energy spectrum. By means of a study performed on a wide range of plasma conditions, it has been observed that the equilibrium plays an important role in the determination of the fluctuation amplitude and of the periodicity values, since the modes resonate at the edge of the RFX-mod plasma. These modes has been interpreted as **Resistive Interchange Modes** (RIM). A good agreement with the theoretical predictions provided by a linear stability code confirms the interpretation proposed, highlighting their pressure-driven nature.

The analysis of the frequency associated to the observed interchange modes indicates that they are rotating along with the plasma in the toroidal direction, i.e. coherently with the plasma flow at the edge, turning the attention also on the topic of the flow itself. The magnetic fluctuations could, thus, be

recognized as an important tool for future studies about the flow behaviour in different plasma conditions.

An important issue to be covered in future is to understand the role of RIM in determining the edge transport properties in RFP plasmas, for which the exact mechanism is still under debate. It will also be crucial to analyze possible ways for the control of these modes, as their importance is expected to largely increase in reactor conditions, due to the steep pressure gradients which should characterize burning plasmas.

Alfvén Eigenmodes. Coherent fluctuations characterized by Alfvénic nature have been detected in a large interval of experimental conditions (in terms of plasma current, densities, working gases, equilibrium). In particular, the frequency of these magnetic activities, characterized by long-wavelength periodicities, has been shown to linearly depend on the Alfvén velocity. A detailed analysis of the experimental observations has allowed to distinguish two kinds of Shear Alfvén Eigenmodes (SAE):

- a first kind of modes (indicated in the thesis as *Type I*) present in almost all the plasma conditions, has been recognized as **Global Alfvén Eigenmodes** (GAE)
- a second kind (*Type II*) associated to the presence of a helical equilibrium (the so-called Single Helical Axis state), spontaneously occurring during high current discharges, is still under study.

The role of the Discrete Reconnection Events (DRE), recurrent quasi-periodic relaxation events characterizing RFP plasmas, in association with SAE has proved to be crucial for at least two reasons: on the one hand, the observation of the frequency evolution just after a DRE led to the localization of the GAE at the edge, on the other hand the enhancement of the power spectrum amplitude of the modes observed during a DRE is investigated in order to verify a possible involvement with the drive for Alfvén eigenmodes in Ohmic plasmas.

Moreover, it is under study the possibility to use the information of the frequency of Alfvén Eigenmodes as a diagnostic tool, a sort of MHD spectroscopy [133]. Indeed, it is worth noting that SAE frequency is particularly sensitive to the values of the magnetic field components and plasma density at the radial position where the modes are destabilized. Thus, using B_θ, B_φ and n_e profiles, it would be, in principle, possible to exploit the frequency measurement with diagnostic purposes, in order to give an estimation of a local value of the effective charge characterizing the plasma.

Microtearing modes.
More recently, the observation of magnetic activities, characterized by extremely high poloidal and toroidal periodicities associated to wavelengths of the same order of magnitude of the ion gyroradius, and arising in corrispondence of the presence of strong temperature gradients, has been identified as a possible first detection of **microtearing instabilities** (MT) in RFP plasmas. A comparison with the theoretical results from a gyrokinetic code seem to confirm this interpretation.

Furthermore, code simulations predict that microtearing modes, in present-day RFX-mod plasmas, may form chains of overlapping magnetic island, contributing significantly to the stochastization of magnetic field lines in the region of the gradients. This strongly influences energy transport in the plasma. The relation between the occurrence of microtearing instabilities and the energy transport measurements in RFX-mod plasma will be the focus of future experimental investigations.

Modes	**MP**	**f [kHz]**	**m**	**n**	$\mathbf{v_{ph}}$	$\mathbf{I_p}$ **[kA]**	**F**
RIM	$\dot{B}_\theta, \dot{B}_\varphi, \dot{B}_r$	100	1	$20 \div 80$	v_D	all	$\lesssim -0.1$
AE I	$\dot{B}_\theta$	$100 \div 1300$	1	0	v_A	all	all
AE II	$\dot{B}_\theta$	$100 \div 500$	≈ 1	≈ 2	v_A	$\gtrsim 1000$	>-0.05
MT	$\dot{B}_\theta, \dot{B}_\varphi, \dot{B}_r$	200	≈ 15	≈ 200	v_{de}	$\gtrsim 1000$	>-0.05

Table 8.3: Scheme of the characteristics of the instabilities observed in RFX-mod plasmas.

Summarizing, the main characteristics of the modes described in the present thesis are schematized in table 8.3. Each instability is, thus, associated to the relative magnetic field component (MP) on which it has been observed, the frequency f and the poloidal m and toroidal n periodicities measured, the phase velocity v_{ph} and the main features of the discharges for modes occurrence (plasma current I_p and reversal parameter F).

Bibliography

[1] www.igi.pd.cnr.it.

[2] M. Zuin, S. Spagnolo, R. Paccagnella, E. Martines, R. Cavazzana, G. Serianni, M. Spolaore, and N. Vianello. **Anisotropic Ion Heating and Tail Generation during Tearing Mode Magnetic Reconnection in a High-Temperature Plasma**. *Nucl. Fusion*, 50:052001, 2010.

[3] S. Spagnolo, M. Zuin, F. Auriemma, R. Cavazzana, E. Martines, M. Spolaore, and N. Vianello. **Alfvén eigenmodes in the rfx-mod reversed-field pinch plasma**. *Nucl. Fusion*, 51:083038, 2011.

[4] D.A. Gurnett and A. Bhattacharjee. ***Introduction to Plasma Physics: With Space and Laboratory Applications***. Cambridge University Press, 2005.

[5] R.J. Goldston and P.H. Rutherford. ***Introduction to Plasma Physics***. Institute of Physics Publishing, 1995.

[6] A. Intravaia, L. Marrelli, P. Martin, R. Pasqualotto, P. Franz, A. Murari, and G. Spizzo *et al.* . **Scaling of Local Core Transport with Lundquist Number in the Reversed Field Pinch**. *Physical Review Letters*, 83:5499–5502, 1999.

[7] T.J.M. Boyd and J.J. Sanderson. ***The Physics of Plasmas***. Cambridge University Press, 2003.

[8] A.A. Choudhuri. ***The physics of fluids and plasmas***. Cambridge University Press, 1981.

[9] J. Friedberg. ***Plasma Physics and Fusion Energy***. Cambridge University Press, 2007.

[10] D. Fasel and M.Q. Tran. **Availability of lithium in the context of future D-T fusion reactors**. Technical report, Centre de Recherches

en Physique des Plasmas, Association EURATOM-Confédération Suisse, 2005.

[11] J. Wesson. ***Tokamaks***. Clarendon Press - Oxford, 2004.

[12] www.iter.org.

[13] L. Rayleigh. **Investigation of the character of the equilibrium of an incompressible heavy fluid of variable density**. *Proceedings of the London Mathematical Society*, 14:170–177, 1883.

[14] G.I. Taylor. **The instability of liquid surfaces when accelerated in a direction perpendicular to their planes**. *Proceedings of the Royal Society of London*, A201:192–196, 1950.

[15] D.H. Sharp. **An overview of Rayleigh-Taylor instability**. *Physica D: Nonlinear phenomena*, 12:3–18, 1984.

[16] S.F. Gull. **The x-ray, optical and radio properties of young supernova remnants**. *Monthly Notices of the Royal Astronomical Society*, 171:263, 1975.

[17] H. Alfvén. **Existence of Electromagnetic-Hydrodynamic Waves**. *Nature*, 150:405–406, 1942.

[18] N.F. Cramer. ***The physics of Alfvén Waves***. Wiley-VCH, 2001.

[19] G. Vlad, F. Zonca, and S. Briguglio. **Dynamics of Alfvén waves in tokamaks**. *La rivista del Nuovo Cimento*, 22:1–97, 1999.

[20] H.P. Furth, J. Killeen, and M.N. Rosenbluth. **Finite-Resistivity Instabilities of a Sheet Pinch**. *Phys. Fluids*, 6:459–484, 1963.

[21] A.E. Lifschitz. ***Magnetohydrodynamics and Spectral Theory***. Kluner Academic Publishers, 1989.

[22] H.A.B. Bodin. **The Reversed Field Pinch**. *Nuclear Fusion*, 30:1717–1737, 1990.

[23] D.C. Robinson and R.E. King. Pinch and tokamak confinement devices. In *Plasma physics and nuclear fusion research*, volume 1, page 263, 1969. Proc. 3rd Int. Conf. Novosibirsk, 1968, IAEA, Vienna.

[24] J.B. Taylor. **Relaxation of Toroidal Plasma and Generation of Reverse Magnetic Fields**. *Physical Review Letters*, 33:1139–1141, 1974.

[25] J.B. Taylor. **Relaxation and magnetic reconnection in plasmas**. *Physical Review Letters*, 58:741–763, 1986.

[26] L. Woltjer. **A theorem on force-free magnetic fields**. *Proceedings of the National Academy of Sciences*, 44:489–491, 1958.

[27] M.G. Rusbridge. **The relationship between the 'tangled discharge' and 'dynamo' models of the magnetic relaxation process**. *Plasma Phys. Contr. Fus.*, 33:1381, 1991.

[28] Zeldovich Y.B, A.A. Ruzmaikin, and D.D. Sokoloff. ***Magnetic fields in Astrophysics***. Gordon&Breach-New York, 1993.

[29] E.N. Parker. **Hydromagnetic dinamo models**. *Astrophysical Journal*, 122:293–314, 1955.

[30] M. Steenbeck and F. Krause and K.H. Rädler. **Berechnung der mittleren Lorentz-Feldstärke $\overline{\mathbf{v} \times \mathbf{B}}$ für ein elektrisch leitendes Medium in turbulenter, durch Coriolis-Kräfte beeinflußter Bewegung.** *Zeitschrift für Naturforschung*, 21a:369–376, 1966.

[31] S. Cappello and D. Biskamp. **Reconnection processes and scaling laws in reversed field pinch magnetohydrodynamics**. *Nuclear Fusion*, 36:571–581, 1996.

[32] S. Cappello and R. Paccagnella. **Nonlinear plasma evolution and sustainment in the reversed field pinch**. *Physics of Fluids B*, 4:611–618, 1992.

[33] J.M. Finn, R. Nebel, and C. Bathke. **Single and multiple helicity ohmic states in reversed field pinches**. *Physics of Fluids B*, 4:1262–1279, 1992.

[34] E. Martines and S. Spagnolo. **One-dimensional simulations of reversed field pinch discharges**. *Physics of Plasmas*, 15:122506, 2008.

[35] S.C. Prager, A.F. Almagri, S. Assadi, J.A. Beckstead, R.N. Dexter, and D.J. Den Hartog *et al.* . **First Results from the Madison Symmetric Torus Reversed Field Pinch**. *Physics of Fluids B*, 2:1367–1371, 1990.

[36] V. Antoni, P. Martin, and S. Ortolani. **Experimental evidence of on axis q oscillations in Eta Beta II**. *Plasma Physics Controlled Fusion*, 29:279–285, 1987.

[37] P. Sonato, G. Chitarin, P. Zaccaria, F. Gnesotto, S. Ortolani, A. Buffa, M. Bagatin, W.R. Baker, S. Dal Bello, P. Fiorentin, L. Grando, G. Marchiori, D. Marcuzzi, A. Masiello, S. Peruzzo, N. Pomaro, and G. Serianni. **Machine modification for active MHD control in RFX**. *Fusion Engineering and Design*, 66:161–168, 2003.

[38] www.cnr.it.

[39] www.enea.it.

[40] www.unipd.it.

[41] www.infn.it.

[42] www.acciaierievenete.com.

[43] F. Gnesotto, P. Sonato, W.R. Baker, A. Doria, F. Elio, M. Fauri, P. Fionentin, G. Marchiori, and G. Zollino. **The plasma system of RFX**. *Fusion Engineering and Design*, 25:335–372, 1995.

[44] P. Zanca, L. Marrelli, G. Manduchi, and G. Marchiori. **Beyond the intelligent shell concept: the clean-mode-control**. *Nuclear Fusion*, 47:1425–1436, 2007.

[45] P. Martin. **Magnetic and thermal relaxation in the RFP**. *Plasma Physics Controlled Fusion*, 41:A247–A255, 1999.

[46] D.F. Escande, P. Martin, S. Ortolani, A. Buffa, P. Franz, L. Marrelli, E. Martines, G. Spizzo, S. Cappello, A. Murari, R. Pasqualotto, and P. Zanca. **Quasi-single-helicity reversed-field-pinch plasmas**. *Physical Review Letters*, 85:1662–1665, 2000.

[47] R. Lorenzini, D. Terranova, A. Alfier, P. Innocente, E. Martines, R. Pasqualotto, , and P. Zanca. **Single-Helical-Axis States in Reversed-Field-Pinch Plasmas**. *Physical Review Letters*, 101:025005, 2008.

[48] P. Innocente, A. Alfier, L. Carraro, R. Lorenzini, R. Pasqualotto, D. Terranova, and the RFX team. **Transport and confinement studies in the RFX-mod reversed-field pinch experiment**. *Nuclear Fusion*, 47:1092–1100, 2007.

[49] E. Martines, R. Lorenzini, B. Momo, S. Munaretto, P. Innocente, and M. Spolaore. **The plasma boundary in single helical axis RFP plasmas**. *Nuclear Fusion*, 50:035014, 2010.

[50] S. Ortolani and D.D. Schnack. ***Magnetohydrodynamics of Plasma Relaxation***. World Scientific, Singapore, 1993.

[51] K.E.J. Olofsson, P.R. Brunsell, E. Witrant, and J.R. Drake. **Synthesis and operation of an FFT-decoupled fixed-order reversed-field pinch plasma control system based on identification data**. *Plasma Phys. Control. Fusion*, 52:104005, 2010.

[52] L. Frassinetti, K.E.J. Olofsson, P.R. Brunsell, and J.R. Drake. **Implementation of advanced feedback control algorithms for controlled resonant magnetic perturbation physics studies on EXTRAP T2R**. *Nuclear Fusion*, 51:063018, 2011.

[53] L. Frassinetti, K.E.J. Olofsson, M.W.M. Khan, P.R. Brunsell, and J.R. Drake. **Controlled Resonant Magnetic Perturbation Physics Studies on EXTRAP T2R** . In *Proceedings of 23th IAEA Fusion Energy Conference, Daejeon, Rep. of Korea, 11th - 16th October*, volume EXS/P3-01, 2010.

[54] P.R. Brunsell, H. Bergsåker, M. Cecconello, J.R. Drake, R.M. Gravestijn, A. Hedqvist, and J.-A. Malmberg. **Initial results from the rebuilt EXTRAP T2R RFP device**. *Plasma Physics Controlled Fusion*, 43:1457–1470, 2001.

[55] J.-A. Malmberg and P.R. Brunsell. **Resistive wall instabilities and tearing mode dynamics in the EXTRAP T2R thin shell reversed-field pinch**. *Physics of Plasma*, 9:212–222, 2002.

[56] N. Vianello and E. Martines *et al.* . **Transport mechanisms in the outer region of RFX-mod**. *Nucl. Fusion*, 49:045008, 2009.

[57] G. De Masi, M. Spolaore, R. Cavazzana, P. Innocente, R. Lorenzini, E. Martines, B. Momo, S. Munaretto, G. Serianni, S. Spagnolo, D. Terranova, N. Vianello, and M. Zuin. **Flow Measurements in the Edge Region of the RFX-Mod Experiment**. *Contrib. Plasma Phys.*, 50:824–829, 2010.

[58] M. Spolaore, G. de Masi, N. Vianello, M. Agostini, D. Bonfiglio, R. Cavazzana, R. Lorenzini, E. Martines, B. Momo, P. Scarin, G. Serianni, S. Spagnolo, and M. Zuin. **Parallel and perpendicular flows in the RFX-mod edge region**. *Journal of Nuclear Materials*, 415:437–442, 2011.

[59] I.H. Hutchinson. ***Principles of Plasma Diagnostics - Second Edition***. Cambrige University Press, 2002.

[60] R. Cavazzana, P. Scarin, G. Serianni, M. Agostini, F. Degli Agostini, V. Cervaro, and L. Lotto. **Optical and electrical diagnostics for the investigation of edge turbulence in fusion plasmas**. *Review of Scientific Instruments*, 75:4152–4154, 2004.

[61] G. Serianni, T. Bolzonella, R. Cavazzana, G. Marchiori, N. Pomaro, L. Lotto, M. Monari, and C. Taliercio. **Development, tests, and data acquisition of the integrated system of internal sensors for RFX**. *Review of Scientific Instruments*, 75:4338–4340, 2004.

[62] G. Serianni, W. Baker, and S. Dal Bello. **High-spatial resolution edge electrostatic probe system for RFX**. *Review of Scientific Instruments*, 74:1558–1562, 2003.

[63] T. Bolzonella, N. Pomaro, G. Serianni, and D. Marcuzzi. **New wide bandwidth in-vessel magnetic measurement system for RFX**. *Review of Scientific Instruments*, 74:1554–1557, 2003.

[64] A. Alfier and R. Pasqualotto. **New Thomson scattering diagnostic on RFX-mod** . *Review of Scientific Instruments*, 78:013505, 2007.

[65] D. Gregoratto, L. Garzotti, P. Innocente, S. Martini, and A. Canton. **Behaviour of electron density profiles and particle transport analysis in the RFX reversed field pinch**. *Nuclear Fusion*, 38:1199–1213, 1998.

[66] R. Paccagnella. **Linear magnetohydrodynamic stability in reversed field pinch with distant and multiple resistive walls**. *Nuclear Fusion*, 38:1067–1081, 1998.

[67] P. Zanca and D. Terranova. **Reconstruction of the magnetic perturbation in a toroidal reversed field pinch**. *Plasma Phys. Control. Fusion*, 46:1115, 2004.

[68] E. Martines, R. Lorenzini, B. Momo, D. Terranova, P. Zanca, A. Alfier, F. Bonomo, A. Canton, A. Fassina, P. Franz, and P. Innocente. **Equilibrium reconstruction for Single Helical Axis reversed field pinch plasmas**. *Plasma Phys. Control. Fusion*, 53:035015, 2011.

[69] L. Garzotti, P. Innocente, S. Martini, A. Reggiori, and G.B. Daminelli. **Noncryogenic pellet injector for diagnostic purposes on the**

RFX reversed field pinch. *Review of Scientific Instruments*, 70:939–942, 1999.

[70] W. Baker, L. Garzotti, P. Innocente, S. Martini, S. Vitturi, P. Zaccaria, J. Bundgaard, B. Sass, and H. Sorensen. **Multishot pellet injection system for RFX**. In *Fusion Engineering, 1995. SOFE '95. 'Seeking a New Energy Era', 16th IEEE/NPSS Symposium*, volume 2, pages 1570–1573, 1995.

[71] M. Zuin, W. Schneider, A. Barzon, R. Cavazzana, P. Franz, E. Martines, M.E. Puiatti, P. Scarin, and E. Zampiva. **Ion temperature measurements by means of a neutral particle analyzer in RFX-mod plasmas**. In *Proceedings of 38th European Physical Society, Strasbourg, France, 27th June - 1st July*, volume PD2.10, 2011.

[72] R.L. Merlino. **Understanding Langmuir probe current-voltage characteristics**. *Am. J. Phys.*, 75:1078–1085, 2007.

[73] P. Stangeby. ***The Plasma Boundary of Magnetic Fusion Devices - Plasma Physics Series***. Institute of Physics, Bristol and Philadelphia, 2000.

[74] V. Antoni, E. Martines, M. Bagatin, D. Desideri, and G. Serianni. **Stochastic magnetic and ambipolar electric fields in the plasma edge region of RFX**. *Nucl. Fusion*, 36:435–442, 1996.

[75] H.Y.W. Tsui, R. D. Bengtson, G. X. Li, H. Lin, M. Meier, Ch. P. Ritz, and A. J. Wootton. **A new scheme for Langmuir probe measurement of transport and electron temperature fluctuations**. *Review of Scientific Instruments*, 63:4608–4610, 1992.

[76] S. Bendat and A.G. Piersol. ***Random Data***. Wiley, New York, 2000.

[77] J.M. Beall, Y.C. Kim, and E.J. Powers. **Estimation of wavenumber and frequency spectra using fixed probe pairs**. *J. Appl. Phys.*, 53:3933–3940, 1982.

[78] B.R. Suydam. **Stability of a Linear Pinch**. *Proceedings of the Second United Nations International Conference on the Peaceful Uses of Atomic Energy*, 31:157–159, 1958.

[79] C. Mercier. **Un Critere necessaire de stabilite hydromagnetique pour un plasma en symetrie de revolution**. *Nuclear Fusion*, 1:47–53, 1960.

[80] F. Porcelli and M.N. Rosenbluthz. **Modified Mercier criterion**. *Plasma Phys. Control. Fusion*, 40:481–492, 1998.

[81] D. Merlin, S. Ortolani, R. Paccagnella, and M. Scapin. **Linear Resistive magnetohydrodynamic stability analysis of Reversed Field Pinch configurations at finite beta**. *Nucl. Fusion*, 29:1153–1160, 1989.

[82] D.H. Liu. **Effects of current and pressure profiles on resistive MHD modes in Reversed Field Pinches**. *Nucl. Fusion*, 37:1083–1093, 1997.

[83] P. Scarin, M. Agostini, R. Cavazzana, F. Sattin, G. Serianni, and N. Vianello. **Edge turbulence in RFX-mod virtual-shell discharges**. *J. Nucl. Mater.*, 363-365:669–673, 2007.

[84] M. Spolaore, N. Vianello, M. Agostini, R. Cavazzana, E. Martines, P. Scarin, G. Serianni, E. Spada, M. Zuin, and V. Antoni. **Direct Measurement of Current Filament Structures in a Magnetic-Confinement Fusion Device**. *Phys. Rev. Lett.*, 102:165001, 2009.

[85] N. Vianello, V. Naulin, R. Schrittwieser, H. W. Müller, M. Zuin, C. Ionita, J.J. Rasmussen, F. Mehlmann, V. Rohde, R. Cavazzana, M. Maraschek, and ASDEX Upgrade Team. **Direct Observation of Current in Type-I Edge-Localized-Mode Filaments on the ASDEX Upgrade Tokamak**. *Phys. Rev. Lett.*, 106:125002, 2011.

[86] F. Villone, Y.Q. Liu, R. Paccagnella, T. Bolzonella, and G. Rubinacci. **Effects of Three-Dimensional Electromagnetic Structures on Resistive-Wall-Mode Stability of Reversed Field Pinches**. *Phys. Rev. Lett.*, 100:255005, 2008.

[87] R. Lorenzini, D. Terranova, F. Auriemma, R. Cavazzana, P. Innocente, S. Martini, G. Serianni, and M. Zuin. **Toroidally asymmetric particle transport caused by phase-locking of MHD modes in RFX-mod**. *Nucl. Fusion*, 47:1468–1475, 2007.

[88] P. Zanca. **Avoidance of tearing modes wall-locking in a reversed field pinch with active feedback coils**. *Plasma Phys. Control. Fusion*, 51:015006, 2009.

[89] A. Bhattacharjee and Eliezer Hameiri. **Self-Consistent Dynamolike Activity in Turbulent Plasmas**. *Phys. Rev. Lett.*, 57:206–209, 1986.

[90] R.D. Sydora, J.N. Leboeuf, Z.G. An, P. H. Diamond, G. S. Lee, and T. S. Hahm. **Dynamics and fluctuation spectra of electrostatic resistive interchange turbulence**. *Phys. Fluids*, 29:2871, 1986.

[91] P. Zhu, D.D. Schnack, F. Ebrahimi, E.G. Zweibel, M. Suzuki, C. C. Hegna, and C.R. Sovinec. **Dynamics and fluctuation spectra of electrostatic resistive interchange turbulence**. *Phys. Rev. Lett.*, 101:085005, 2008.

[92] R.B. White, E. Fredrickson, D. Darrow, M. Zarnstorff, R. Wilson, S. Zweben, K. Hill, Y. Chen, and G. Fu. **Toroidal Alfven Eigenmode Induced Ripple Trapping**. *Physics of Plasmas*, 2:2871–2873, 1995.

[93] K.L. Wong, R. Budny, R. Nazikian, C.C. Petty, C.M. Greenfield, W.W. Heidbrink, and E. Ruskov. **Alpha-Channeling Simulation Experiment in the DIII-D Tokamak**. *Physical Review Letters*, 93:085002, 2004.

[94] S.E. Sharapov, B. Alper, J. Fessey, N.C. Hawkes, N.P. Young, R. Nazikian, G.J. Kramer, D.N. Borba, S. Hacquin, E. De La Luna, S.D. Pinches, J. Rapp, D. Testa, and JET-EFDA Contributors. **Monitoring Alfvén Cascades with Interferometry on the JET Tokamak**. *Physical Review Letters*, 93:165001, 2004.

[95] S.M. Mahajan. **Spectrum of Alfvén waves, a brief review**. *Physica Scripta*, T60:160–170, 1995.

[96] L. Chen. **Alfvén waves: a journey between space and fusion plasmas**. *Plasma Physics Controlled Fusion*, 50:124001, 2008.

[97] W.W. Heidbrink. **Basic physics of Alfvén instabilities driven by energetic particles in toroidally confined plasmas**. *Physics of Plasmas*, 15:055501, 2008.

[98] C.Z. Cheng and M.S. Chance. **Low-n shear Alfvén spectra in axisymmetric toroidal plasmas**. *Phys. Fluids*, 29:3695–3702, 1986.

[99] K.L. Wong, R.J. Fonck, S.F. Paul, and D.R. Roberts *et al.* . **Excitation of toroidal Alfvén eigenmodes in TFTR**. *Phys. Rev. Lett.*, 66:1874–1877, 1991.

[100] E.D. Fredrickson, R.E. Bell, D.S. Darrow, G.Y. Fu, N.N. Gorelenkov, B.P. LeBlanc, S.S. Medley, J.E. Menard, H. Park, and A.L. Roquemore

et al. . **Collective fast ion instability-induced losses in National Spherical Tokamak Experiment**. *Phys. Plasmas*, 13:056109, 2006.

[101] M. Hirsch *et al.* . **Major results from the stellarator Wendelstein 7-AS**. *Plasma Phys. Control. Fusion*, 50:053001, 2008.

[102] G. Regnoli, H. Bergsåker, E. Tennfors, F. Zonca, E. Martines, G. Serianni, M. Spolaore, N. Vianello, M. Cecconello, V. Antoni, R. Cavazzana, and J.-A. Malmberg. **Observations of toroidicity-induced Alfvén eigenmodes in a reversed field pinch plasma**. *Physics of Plasmas*, 12:042502, 2005.

[103] Ya.I. Kolesnichenko, V.V. Lutsenko, H. Wobig, Yu.V. Yakovenko, and O.P. Fesenyuk. **Alfvén continuum and high-frequency eigenmodes in optimized stellarators**. *Phys. Plasmas*, 8:491–509, 2001.

[104] Z. Chang, E.D. Fredrickson, S.J. Zweben, H.K. Park, R. Nazikian, E. Mazzucato, S.H. Batha, M.G. Bell, R.V. Budny, and C.E. Bush *et al.* . **Alfvén frequency modes at the edge of tftr plasmas** . *Nucl. Fusion*, 35:1469–1479, 1995.

[105] K. Appert, R. Gruber, F. Troyon, and J. Vaclavik. **Excitation of global eigenmodes of the Alfven wave in Tokamaks** . *Plasma Phys.*, 24:1147–1159, 1982.

[106] G.A. Collins, F. Hofmann, B. Joye, R. Keller, A. Lietti, J.B. Lister, and A. Pochelon. **The Alfvén wave spectrum as measured on a tokamak** . *Phys. Fluids*, 29:2260–2273, 1986.

[107] S.M. Mahajan and D.W. Ross. **Spectrum of compressional Alfvén waves**. *Phys. Fluids*, 26:2561–2565, 1983.

[108] J.J. Koliner, C.B. Forest, D. Spong, J.S. Sarff, S.P. Oliva, J.K. Anderson, and A.R. Almagri. **Study of Alfvén Eigenmodes on the Madison Symmetric Torus**. In *Bulletin of the American Physical Society, 52nd Annual Meeting of the APS-DPP, Chicago, Illinois, November 8th-12th 2010*, volume PP9.43, 2010.

[109] N.N. Gorelenkov, E. Belova, H.L. Berk, C.Z. Cheng, E. Fredrickson, W.W. Heidbrink, S. Kaye, and G.J. Kramer. **Beam ion driven instabilities in the National Spherical Tokamak Experiment**. *Phys. Plasmas*, 11:2586–2593, 2004.

[110] E. Belova. **Numerical modeling of NBI-driven sub-cyclotron frequency modes in NSTX**. In *Bulletin of the American Physical Society, 52nd Annual Meeting of the APS-DPP, Chicago, Illinois, November 8th-12th 2010*, volume TI2.3, 2010.

[111] A. Boileau, M. von Hellermann, L.D. Horton, J. Spence, and H.P. Summers. **The deduction of low-Z ion temperature and densities in the JET tokamak using charge exchange recombination spectroscopy**. *Plasma Physics and Controlled Fusion*, 31:779–804, 1989.

[112] A. Fasoli, B.N. Breizman, D. Borba, R.F. Heeter, M.S. Pekker, and S.E. Sharapov. **Nonlinear Splitting of Fast Particle Driven Waves in a Plasma: Observation and Theory**. *Phys. Rev. Lett.*, 81:5564–5567, 1998.

[113] M.P. Gryaznevich, M. Lilley S.E. Sharapov, S.D. Pinches, A.R. Field, D. Howell, D. Keeling, R. Martin, H. Meyer, H. Smith, R. Vann, P. Denner, E. Verwichte, and the MAST Team. **Recent experiments on Alfvťen eigenmodes in MAST**. *Nucl. Fusion*, 48:084003, 2008.

[114] H.L. Berk, B.N. Breizman, and M.S. Pekker. **Nonlinear theory of kinetic instabilities near threshold**. *Plasma Phys. Rep.*, 23:778–788, 1997.

[115] R. Lorenzini, F. Auriemma, P. Innocente, E. Martines, S. Martini, and D. Terranova. **Confinement loss during dynamo relaxation event in RFX-mod**. *Plasma Phys. Control. Fusion*, 50:035004, 2008.

[116] L. Villard and J. Vaclavik. **Alfvén frequency modes and global Alfvén eigenmodes**. *Nucl. Fusion*, 37:351–360, 1997.

[117] E.M. Edlund, M. Porkolab, G.J. Kramer, L. Lin, Y. Lin, and S.J. Wukitch. **Observation of Reversed Shear Alfvén Eigenmodes between Sawtooth Crashes in the Alcator C-mod Tokamak**. *Phys. Rev. Lett.*, 102:165003, 2009.

[118] M. Maraschek, S. Günter, T. Kass, B. Scott, H. Zohm, and ASDEX Upgrade Team. **Observation of Toroidicity-Induced Alfvén Eigenmodes in Ohmically Heated Plasmas by Drift Wave Excitation**. *Phys. Rev. Lett.*, 79:4186–4189, 1997.

[119] G. Besson, A. de Chambrier, G.A. Collins, B. Joye, A. Lietti, J.B. Lister, J.M. Moret, S. Nowak, C. Simm, and H. Weisen. **A review of Alfvén wave heating**. *Plasma Phys. Control. Fusion*, 28:1291–1303, 1986.

[120] N. Vianello, M. Spolaore, E. Martines, R. Cavazzana, G. Serianni, M. Zuin, E. Spada, and V. Antoni. **Drift-Alfvén vortex structures in the edge region of a fusion relevant plasma**. *Nucl. Fusion*, 50:042002, 2010.

[121] S. Costa, R. Paccagnella, F. Pegoraro, and M. Viterbo. **A wave-particle interaction model for tail ion acceleration in reversed field pinch plasmas**. *Plasma Phys. Control. Fusion*, 41:1485–1496, 1999.

[122] R.M. Magee, D.J. Den Hartog, S.T.A. Kumar, A.F. Almagri, B.E. Chapman, G. Fiksel, V.V. Mirnov, E.D. Mezonlin, and J.B. Titus. **Anisotropic Ion Heating and Tail Generation during Tearing Mode Magnetic Reconnection in a High-Temperature Plasma**. *Phys. Rev. Lett.*, 107:065005, 2011.

[123] G. Fiksel, A.F. Almagri, B.E. Chapman, V.V. Mirnov, Y. Ren, J.S. Sarff, and P. W. Terry. **Mass-Dependent Ion Heating during Magnetic Reconnection in a Laboratory Plasma**. *Phys. Rev. Lett.*, 103:145002, 2009.

[124] J.F. Drake and Y.C. Lee. **Kinetic theory of tearing instabilities**. *Phys. Fluids*, 20:1341–1353, 1977.

[125] J. F. Drake, N.T. Gladd, C.S. Liu, and C.L. Chang. **Microtearing Modes and Anomalous Transport in Tokamaks**. *Phys. Rev. Lett.*, 44:994–997, 1980.

[126] I. Predebon, F. Sattin, M. Veranda, D. Bonfiglio, and S. Cappello. **Microtearing Modes in Reversed Field Pinch Plasmas**. *Phys. Rev. Lett.*, 105:195001, 2010.

[127] R. Lorenzini, E. Martines, P. Piovesan, D. Terranova, P. Zanca, and M. Zuin *et al.* . **Self-organized helical equilibria as a new paradigm for ohmically heated fusion plasmas**. *Nature Physics*, 5:570–574, 2009.

[128] M. Kotschenreuther, G. Rewoldt, and W.M. Tang. **Comparison of initial value and eigenvalue codes for kinetic toroidal plasma instabilities**. *Comp. Phys. Comm.*, 88:128–140, 1995.

[129] W. Dorland, F. Jenko, M. Kotschenreuther, , and B.N. Rogers. **Electron Temperature Gradient Turbulence**. *Phys. Rev. Lett.*, 85:5579–5582, 2000.

[130] I. Predebon, C. Angioni, and S.C. Guo. **Gyrokinetic simulations of ion temperature gradient modes in the reversed field pinch**. *Phys. Plasmas*, 17:012304, 2010.

[131] N. Vianello, M. Spolaore, G. Serianni, H. Bergsåker, V. Antoni, and J.R. Drake. **Properties of the edge plasma in the rebuilt EXTRAP T2R reversed-field pinch experiment**. *Plasma Phys. Control. Fusion*, 44:2513–2523, 2002.

[132] L. Frassinetti, P.R. Brunsell, and J.R. Drake. **Experiments and modelling of active quasi-single helicity regime generation in a reversed field pinch**. *Nuclear Fusion*, 49:075019, 2009.

[133] A. Fasoli, D. Testa, S. Sharapov, H.L. Berk, B. Breizman, A. Gondhalekar, R.F. Heeter, M. Mantsinen, and contributors to the EFDA-JET Workprogramme. **MHD spectroscopy**. *Plasma Phys. Control. Fusion*, 44:B159–B172, 2002.